

Chapter 1

**P-TYPE TRANSPARENT SEMICONDUCTING
DELAFOSSITE CuAlO_{2+x} THIN FILM: PROMISING
MATERIAL FOR OPTOELECTRONIC DEVICES
AND FIELD-EMISSION DISPLAYS**

Arghya N. Banerjee^{1,a} and Kalyan K. Chattopadhyay^{2,b}

¹Nanoscale Device Research, Department of Electrical and Computer Engineering,
University of Nevada, Las Vegas, Nevada-89154, US.

²Thin Film and Nanoscience Laboratory, Department of Physics, Jadavpur University,
Kolkata-700032, India.

Abstract

Copper based delafossite transparent semiconducting oxide thin films have recently gained tremendous interest in the field of optoelectronic technology, after the discovery of p-type conductivity in a transparent thin film of copper aluminum oxide (CuAlO_2). Most of the well-known and widely used transparent conducting oxide thin films such as ZnO , SnO_2 , ITO etc. and their doped versions are n-type material, but corresponding p-type transparent conducting oxides were surprisingly missing for a long time until the fabrication of above-mentioned p-CuAlO₂ thin film have been published (*Nature* 1997, 389, 939). This has opened up a new field in opto-electronics device technology, the so-called “Transparent Electronics”, where a combination of the two types of transparent conducting oxides in the form of a p-n junction could lead to a ‘functional’ window, which transmits visible portion of solar radiation yet generates electricity by the absorption of UV part of it. Non-stoichiometric and doped versions of various new types of p-type transparent conducting oxides with improved optical and electrical properties have been synthesized in the last few years in this direction. Wide range of deposition techniques have been adopted to prepare the films. But fabrication of device quality films by cost-effective deposition techniques such as sputtering, chemical vapor deposition, wet-chemical dip-coating technique etc. are the need of the hour for large-scale production of these films for diverse device applications. Here we have discussed the fabrication and opto-electrical characterization of p-CuAlO_{2+x} thin films by cost-effective and

^a E-mail address: banerjee_arghya@hotmail.com; arghya@egr.unlv.edu (Arghya N. Banerjee, corresponding author)

^b E-mail address: kalyan_chattopadhyay@yahoo.com (Kalyan K Chattopadhyay)

scaleable deposition routes such as sputtering and wet-chemical dip-coating technique. We have also discussed briefly some of the new developments in the field of p-type transparent conducting oxide thin film technology and an up-to-date and comprehensive description of different Cu-based p-type transparent conducting oxide thin films is presented. Also the origin of p-type conductivity in these transparent oxides has been dealt with considerable attention. Fabrication of all-transparent junctions is also discussed which is most important in the development of ‘Transparent Electronics’. Field emission properties of thin films are currently of much interest due to the potential application in field emission displays (FEDs), which are considered to be strong candidate for low-power panel applications. The low-threshold field emission properties of wide-bandgap CuAlO₂ thin films have been investigated for its potential applications in FED technology. The films showed considerable low turn-on field. This finding might open up a new direction in the field emission technology, and a new group of materials (such as, different transparent conducting oxides) might become a promising candidate for low-threshold field emitter. Also, recently, the research on nanostructured materials generates great interest in the scientific community and offers tremendous opportunities in the field of *science* and technology. Here, we have also discussed in brief, the formation of nanocrystalline p-CuAlO₂ films, which may open up an extremely important and interesting field of research for the fabrication of all-transparent nano-active devices. This will not only give a new dimension in the field of ‘Transparent Electronics’, but new avenues may open up in the nanoparticle research keeping an eye on its tremendous applications in optoelectronics technology.

1. Introduction

In the last century, scientists have made rapid and significant advances in the field of semiconductor physics. Semiconducting materials have been the subjects of great interest due to their numerous practical applications and also they provide fundamental insights into the electronic processes involved. Thus material processing has similarly become an increasingly important research field. Many new materials and devices, which possess specific properties for special purposes, have now become available, but material limitations are often the major deterrent to the achievement of new technological advances. Material scientists are now particularly interested in developing materials which maintain their required properties in extreme environment. In general it is the aim of the material scientists to find ways of improving qualities and increasing productivity, whilst reducing the manufacturing cost.

One of the most important fields of interest in materials *science* is the fundamental aspects and applications of semiconducting transparent films, which are more popularly known as “Transparent Conducting Oxides” (TCO) in opto-electronic device technology. The characteristics of such films are high room-temperature electrical conductivity ($\sim 10^3$ S cm⁻¹ or more) and high optical transparency (more than 80 %) in the visible region. TCOs are well-known and widely used for a long time in opto-electronics industries as well as in research fields. After the first report of transparent conducting cadmium oxide (CdO) thin film by Badekar [1] in 1907, extensive works have been done in the field of TCO technology to prepare new types of TCOs with wide ranging applications [2 – 12]. Some of these well-known and widely used TCOs include In₂O₃: Sn/F/Sb/Pb, ZnO: In/Al/F/B/Ga, Cd₂SnO₄, SnO₂: Sb/F etc. as well as some new TCOs such as CdIn₂O₄: Sn, CdSb₂O₆: Y, GaInO₃: Ge/Sn, AgInO₂: Sn, MgIn₂O₄, In₄Sn₃O₁₂, Zn₂SnO₄, ZnSnO₃, Zn₂In₂O₅, ZnGa₂O₄ etc. [13 – 43].

Technologically, these TCOs are being used extensively in various fields, which include solar cells, flat panel displays (FPD), low-emissivity (“low-e”) windows, electromagnetic

shielding of cathode-ray tubes in video display terminals, electrochromic (EC) materials in rear-view mirrors of automobiles, EC-windows for privacy (so-called “smart windows”), oven windows, touch-sensitive control panels, defrosting windows in refrigerators and airplanes, invisible security circuits, gas sensors, biosensors, organic light emitting diodes (OLED), polymer light emitting diodes (PLED), antistatic coatings, cold heat mirrors, etc. [1 – 4, 8 – 9, 13, 44 – 54]. Also some new applications of TCOs have been proposed recently such as holographic recording medium, high-refractive index waveguide overlays for sensors and telecommunication applications, write-once read-many-times memory chips (WORM), electronic ink etc. [55 – 58]. And lastly, the low-temperature deposition of TCOs onto poly(ethylene terephthalate) (PET), polyamides and other polymer substrates in roll-coating processes for touch-screen and infra-red reflector applications are the recent challenges for the TCO industries [59 – 61].

Possibility of the above-mentioned novel applications of TCOs is based on the fact that the electronic band gap of a TCO is higher than 3.1 eV (corresponding to the energy of a 400 nm blue photon). So visible photons (having energy between 2.1 to 3.1 eV) cannot excite electrons from valence band (VB) to the conduction band (CB) and hence are transmitted through it, whereas they have enough energy to excite electrons from donor level to CB (for n-type TCO) or holes from acceptor level to VB (for p-type TCO). And these acceptor or donor levels are created in the TCOs by introducing non-stoichiometry and (or) appropriate dopants in a controlled manner. A schematic representation of the bandgap designing for transparent conductors is shown in Fig. 1(a).

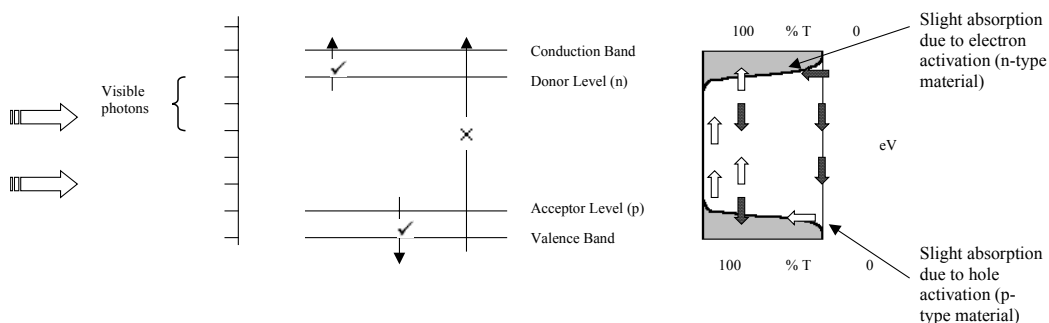


Figure 1(a). Bandgap designing for transparent conductors. Visible photons (2.1 eV to 3.1 eV) do not have enough energy to excite electrons from valence band to conduction band, but have enough energy to excite holes (for p-type) from acceptor level to VB or electrons (for n-type) from donor level to CB.

Although the TCOs have vast range of applications as mentioned above, very little work have been done on the active device fabrication using TCOs [62, 63]. This is because most of the aforementioned TCOs are n-type semiconductors. But the corresponding p-type transparent conducting oxide (p-TCO), which are essential for junctional devices, were surprisingly missing in thin film form for a long time, until in 1997, Kawazoe and co-authors reported the p-type conductivity in a highly transparent thin film of copper aluminum oxide (CuAlO_{2+x}) [64]. This has opened up a new field in opto-electronics device technology, the so-called “Transparent Electronics” or “Invisible Electronics” [65], where a combination of the two types of TCOs in the form of a p-n junction could lead to a ‘functional’ window, which transmits visible portion of solar radiation yet generates electricity by the absorption of

UV part [64]. It must be mentioned here that the first report of semi-transparent p-type conducting thin film of nickel oxide was published in 1993 by Sato et al [66]. They observed only 40 % transmittance of the NiO films in the visible region and when they tried to fabricate an all-TCO p-i-n diode of the form p-NiO/i-NiO/i-ZnO/n-ZnO, the visible transmittance further reduced to almost 20 %. Although this low transmittance was not favorable for superior device applications, but still this report was an important milestone in the field of “Transparent Electronics” and in the development of TCO technology.

Now for diverse device applications, it is utmost important to prepare various new types of p-TCOs with superior optical and electrical characteristics, at least comparable to the existing, widely used n-TCOs, which are having transparency above 80 % in the visible region and conductivity about 1000 S cm^{-1} or more. Intense works have been done for the last few years in this direction to fabricate new p-TCOs by various deposition techniques. Also quite a number of works have been carried out for proper understanding of the structural, optical and electrical characteristics of p-TCOs. As this is an emerging field in TCO technology, preparation of new materials as well as existing materials with new deposition techniques is the need of the hour.

Copper aluminum oxide (CuAlO_2) is the first and the most important p-TCO material reported in thin film form [64], which has reasonable optical and electrical properties for diverse device applications. The reported visible transparency of this material is around 80 % with a direct bandgap value of 3.5 eV, whereas the room temperature conductivity (σ_{RT}) is 0.34 S cm^{-1} with a carrier concentration $\sim 3.0 \times 10^{19} \text{ cm}^{-3}$ [67]. Although the reported transparency is quite high but the hole concentration is one to two orders of magnitude lower than the corresponding well-known and widely used n-TCO thin films e.g. ITO, ZnO, SnO_2 etc. Therefore, as far as technological aspects are concerned, improvement in the electrical characteristics of this material is the need of the hour alongwith the reproducibility with the required opto-electrical properties.

The electrical, optical, structural as well as morphological properties and hence device performance of CuAlO_2 thin films are highly correlated with the deposition techniques. The growth parameters, especially deposition atmosphere, substrate temperature, post-deposition annealing of the films etc., control the properties of CuAlO_2 thin films to a large extent. Defect chemistry plays a major role in the enhancement of the p-type conductivity of the films. So a systematic study of the effect of different growth parameters on the characteristics of the films is needed for improved material synthesis. Also low-cost processes to deposit device quality CuAlO_2 and similar types of p-TCO thin films are the most important issue for large-scale production of these films for diverse device applications. And most importantly, transparent junction fabrication with superior opto-electronic properties will be the next significant step towards the realization of “Transparent Electronics”.

Nanocrystalline CuAlO_2 thin films: After the pioneering works of Efros and Efros [68] and Brus [69] on the size-quantization effect in semiconductor nanoparticles, the research on nanostructured materials generates great interest in the scientific community and offers tremendous opportunities in *science* and technology because of new properties exhibited by these materials and challenging problems thrown up for providing theoretical concepts in physics associated with it [70-72]. Infact, both the natural as well as the artificial world can now be categorized in two regimes: micro regime and nano regime. Starting from a human hair to DNA structure – the *nature* evolves itself from micro to nano scale structures. Similarly, man made world is now shifting its attention from micro devices to nano materials.

Fig. 1(b) schematically represents the broad spectrum of the micro and nano regime, indicating how natural and man made world evolve into smaller domain.

Optical properties of nanocrystals are markedly related to their size and surface chemistry and drastically differ from those of bulk materials. Preparation and study of high quality quantum dots [73], nanobelts [74] and nanowires [75] have been reported widely. These achievements in the last few years have focused nanoparticle research on their applications in electrical and optoelectronics devices [76-77].

Syntheses and characterizations of nanostructured n-TCOs are very important and well-established field in nanotechnology and still growing in stature. Therefore, the formation of nanocrystalline p-type counterpart may open up an extremely important and interesting field of research for the fabrication of all-transparent nanoactive devices. This will not only give a new dimension in the field of "Transparent Electronics", but new avenues may open up in the nanoparticle research keeping an eye on its tremendous applications in optoelectronics technology.

Field-emission displays: Low-macroscopic field (LMF) emission of electrons from the surface of a thin film to the vacuum in the presence of a macroscopic electric field (mean field between the parallel plates in a capacitor configuration) is currently of much interest due to the potential application in cold cathode devices. Also field emission displays (FEDs) are considered to be strong candidate for low-power panel application because of its very thin profile, high production efficiency, fast response, high brightness, wide operating temperature, possible expansion of size and last but not the least, high picture quality at a lower cost [78]. Spindt tip cathodes made up of materials with high work function, e.g. Mo, W, Si etc. are used in typical FEDs. For extraction of electrons from these cathodes, sharp tips with radii as low as 20 nm were constructed, which enhances the macroscopic field at the emitter-tip and supplies the necessary barrier-field (also called local-field at the emitter-tip) to produce the field-emission-tunneling. These emitted electrons are then allowed to collide with fluorescent material applied to the cathode, thus emitting light. A schematic diagram of the light emitting principle of the FED system is shown in Fig. 1(c). While the cathode of a CRT uses a point electron source, an FED uses a surface electron source. 6-inch color FED panels have already been manufactured, and research and development on 10-inch FEDs is proceeding very rapidly. When compared with TFT LCDs, FEDs offer a superior viewing angle (160 degrees both vertically and horizontally) and are several microseconds quicker in response speed. In the last decade, low-macroscopic field emission from carbon based films like diamond, diamond like carbon (DLC), amorphous carbon (a: C) etc. [79, 80], made them strong candidate materials for FEDs.

It was found that the materials with wide bandgap (such as diamond) have low or negative electron affinity, which, in turn, enhances the low-macroscopic field emission properties of diamond films [81]. Also p-type semiconducting diamond film showed low-threshold field emission properties [82].

CuAlO_2 - being a p-type wide bandgap semiconducting material, can become a candidate material for potential field-emitters. Infact, we have first reported the low macroscopic field emission, at a relatively lower threshold, from CuAlO_2 thin film, deposited on glass substrate. The emission properties have been studied for different anode-sample spacing. The threshold field and approximate local work function are calculated and we have tried to explain the emission mechanism therefrom. As mentioned above, CuAlO_2 is a transparent p-type semiconducting material, which has excellent potential to be used in opto-electronics device

technology [64, 83]. Its field emission properties have given an additional impetus on the properties of this technologically important material and may open up a new window in the

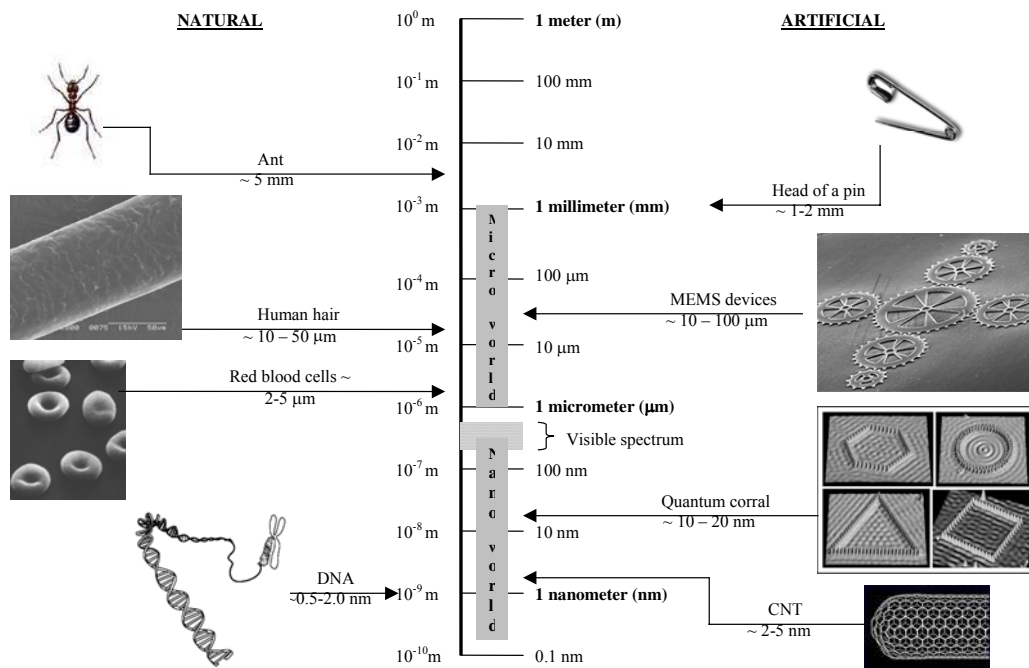


Figure 1(b). Description of nano regime. From Forbes-Nanotech Report.

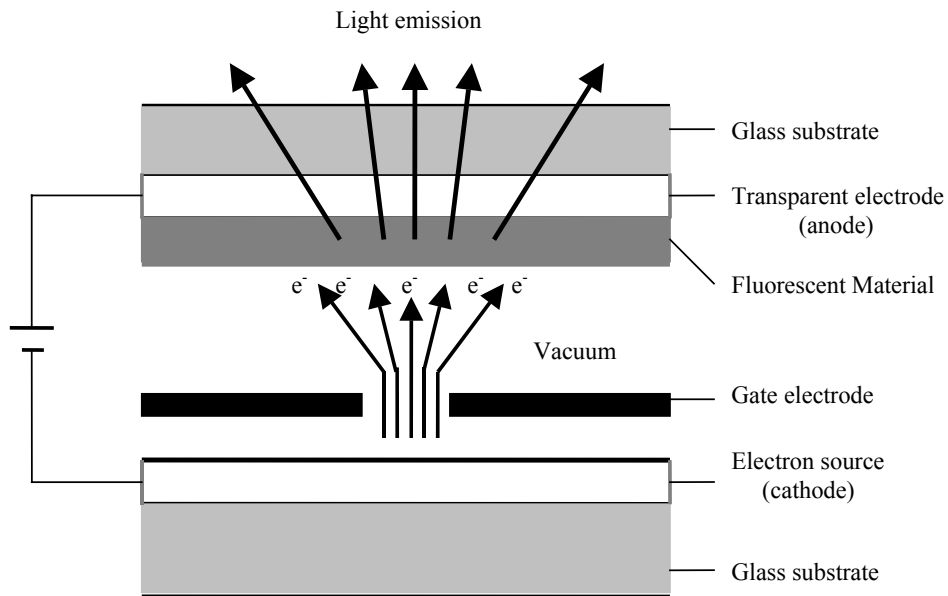


Figure 1(c). Schematic diagram of the light emitting principle of the FED system.

field-emission technology with a new group of materials other than carbon-based films like amorphous carbon (a: C), diamond like carbon (DLC), diamond, carbon nano-tubes (CNT), silicon carbide (Si: C) nano-rods etc. [84-87].

2. Brief Review of Past Work

As p-TCO technology is an important and emerging field of research, hence a systematic review of the major developments in p-TCO materials with regard to the different deposition techniques and properties of the films so obtained are the needs of the hour. A brief and partial review on this field had been reported previously by Tate and co-authors [89] as well as by Nagarajan and co-authors [89-90]. Also Norton [91] presented a detailed review on the synthesis and properties of oxide thin films, which briefly includes the importance of p-TCO too. We have recently published a detailed and up-to-date review on the recent developments in this interesting and challenging field of p-type transparent conducting oxides [92]. Fig. 2(a) describes different p-TCO materials fabricated so far by various groups around the globe. Here we have tried to give a comprehensive picture of the developments in various Cu-based p-TCO thin films, starting with CuAlO_2 , which is the first and most important material in this family. We have also discussed, in details, the fabrication of various transparent junctions, which is the most important aspect of the “Invisible Electronics”. Also a brief review on the recent activities on nanostructured p-TCO thin films have been presented, which is an extremely important field of research for the development of nano-active devices. And lastly, field-emission properties of various wide bandgap materials and their applications in FED technology have been presented.

2.1. Copper Based p-TCO Films

2.1.1. Delafossite Films

Delafossite materials have the chemical formula $\text{M}^{\text{I}}\text{M}^{\text{III}}\text{O}_2$, where M^{I} : monovalent cations such as Cu^+ , Ag^+ , Pd^+ , Pt^+ etc. and M^{III} : trivalent cations such as Al^{+3} , Ga^{+3} , In^{+3} , Cr^{+3} , Fe^{+3} , Co^{+3} , Y^{+3} , La^{+3} , Sc^{+3} etc. Amongst them, those materials having d^{10} orbital (Cu, Ag) show p-type semiconducting behavior whereas those with d^9 orbital (Pt, Pd) show metallic conductivity [93-95]. For p-TCO technology, materials from the former group show the required properties for possible device applications. The first and the most important material in this group is the copper aluminum oxide (CuAlO_2). Although this material is known to exist for nearly 50 years [96] and back in 1984 its p-type conductivity was first reported by Benko and Koffyberg [97], but Kawazoe and co-authors [64] first prepared it in transparent thin film form for possible applications in p-TCO technology. The structural properties of this material were extensively studied by Ishiguro and co-authors [98-100]. The structure is shown in Fig. 2(b) and described in details later. It belongs to $R\bar{3}m$ (D_{3d}) space group with rhombohedral crystal structure [95]. The crystal data of CuAlO_2 is given in Table 1. Other p-TCO thin films belonging to this group are copper gallium oxide (CuGaO_2) and copper indium oxide (CuInO_2) [101-103]. The lattice parameters of these materials were reported in various literatures [94, 104-105]. Also, the band structures of these materials were calculated

by Yanagi et al. [67], Robertson et al. [106] and Ingram et al. [107] in details. Doped versions of some similar types of p-TCO thin films have also been reported which include iron doped copper gallium oxide (CuGaO_2 : Fe), calcium doped copper indium oxide (CuInO_2 : Ca), magnesium doped copper scandium oxide (CuScO_2 : Mg), magnesium doped copper chromium oxide (CuCrO_2 : Mg), calcium doped copper yttrium oxide (CuYO_2 : Ca) etc. [88, 102-103, 108-110]. Crystallographic data as well as band structure calculations of these materials had also been reported in various literatures [104, 111-112]. Preparation of some other highly resistive ($\sim 10^6 \Omega\text{-cm}$) new delafossite materials such as $\text{CuFe}_{1-x}\text{V}_x\text{O}_2$ ($x = 0.5$), $\text{CuNi}_{1-x}\text{Sb}_x\text{O}_2$, $\text{CuZn}_{1-x}\text{Sb}_x\text{O}_2$, $\text{CuCo}_{1-x}\text{Sb}_x\text{O}_2$, $\text{CuMg}_{1-x}\text{Sb}_x\text{O}_2$, $\text{CuMn}_{1-x}\text{Sb}_x\text{O}_2$ ($x = 0.33$) in powder form had been reported by Nagarajan et al. [89-90] (but no thin film preparation of these materials has been reported so far). Preparation of 10 % Sn doped $\text{CuNi}_{1-x}\text{Sb}_x\text{O}_2$ thin film has been reported by the same group [88, 90], having reasonable visible transparency (60 %) and conductivity ($5 \times 10^{-2} \text{ S cm}^{-1}$). The electrical and optical properties of these films are described in Table 2.

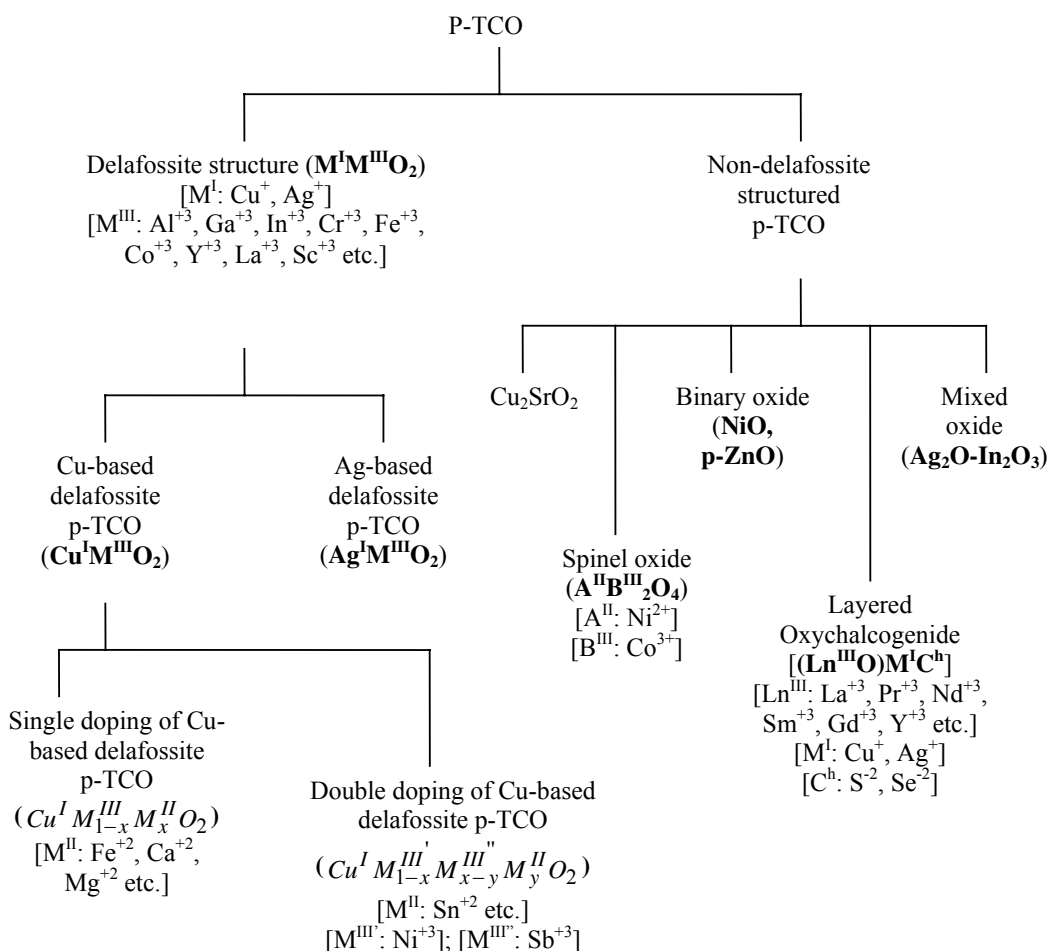
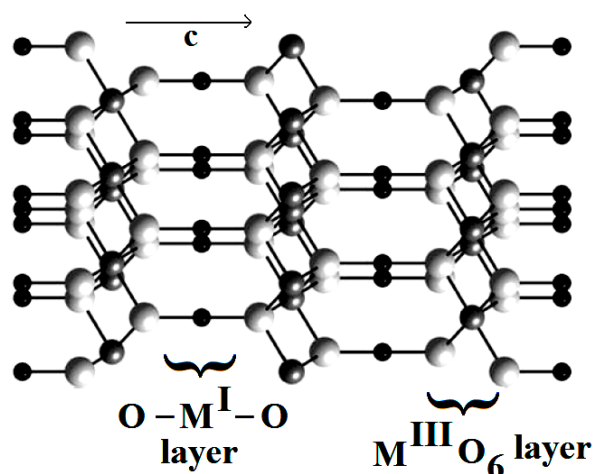


Figure 2(a). Chart of various p-TCO materials reported so far. Here the doped versions of Cu-based delafossite p-TCOs have been mentioned only.



- M^I (Cu, Ag etc.)
- M^{III} (Al, Ga, In etc.)
- Oxygen

Figure 2(b). Delafossite Crystal Structure.

Table 1. Crystal data for CuAlO_2 [98, 104, 106, 113]

 System - Rhombohedral

Space Group - $R\bar{3}m$ (D_{3d})

$a = 2.858 \text{ \AA} = b$, $c = 16.958 \text{ \AA}$

$\alpha = 28.1^\circ = \beta$

$\text{Cu-O} = 1.86 \text{ \AA}$, $\text{Al-O} = 1.91 \text{ \AA}$, $\text{Cu-Cu} = 2.86 \text{ \AA}$

Table 2. Delafossite p-TCO thin films with different doping concentrations and their respective opto-electrical parameters.

Material	Dopant	% dop-ing	Average film thickness (nm)	T (%)	$E_{g\text{-direct}}$ (eV)	σ_{RT} (S cm^{-1})	S_{RT} ($\mu\text{V K}^{-1}$)	Ref.
CuAlO_2	undoped	---	230	70	3.5	0.34	+ 214	67
CuGaO_2	undoped	---	500	80	3.6	0.063	+ 560	101
$\text{CuGa}_{1-x}\text{Fe}_x\text{O}_2$	Fe	0.5	150	60	3.4	1.0	+ 500	88
$\text{CuIn}_{1-x}\text{Ca}_x\text{O}_2$	Ca	0.07	170	70	~ 3.9	0.028	+ 480	103
CuCrO_2	undoped	---	250	40	~ 3.1	1.0	---	109
$\text{CuCr}_{1-x}\text{Mg}_x\text{O}_2$	Mg	0.5	270	50	3.1	220.0	+ 150	89, 109
CuYO_2	undoped	---	200	60	~ 3.5	0.025	---	89, 110

Table 2. Continued

Material	Dopant	% dop-ing	Average film thickness (nm)	T (%)	$E_{g-direct}$ (eV)	σ_{RT} ($S\ cm^{-1}$)	S_{RT} ($\mu V\ K^{-1}$)	Ref.
$CuY_{1-x}Ca_xO_2$	Ca	0.01-0.02	240	50	3.5	1.05	+ 275	89, 110
$CuScO_2^*$	undoped	---	110	40	~ 3.3	30.0	---	89, 108
$CuSc_{1-x}Mg_xO_2^\#$	Mg	0.05	220 - 250	80	3.3 -3.6	~ 0.07	---	88, 114
				60	-do-	~ 0.1	---	
				25	-do-	~ 0.8	---	
				15	-do-	~ 20.0	---	
$CuNi_{1-x}Sb_x\text{-}ySn_yO_2$	Ni	0.66	~ 200	60	3.4	0.05	+ 250	88
	Sb	0.30						
	Sn	0.033						

*Maximum of 25 % oxygen was intercalated.

[#] The variation of transparency of the films at the expense of conductivity was due to a variation of oxygen pressure from 3 Torr (for most transparent film) to 15,000 Torr (for least transparent film). Also according to Ref. [115] the doping concentration of Mg was 1 %.

2.1.2. Nondelafossite Films

Cu_2SrO_2 : Besides delafossite films, another Cu-based p-TCO thin film in the form of Cu_2SrO_2 has been synthesized by Kudo et al. [116]. The crystallographic data and band structure calculations were done by Teske et al. [117], Boudin et al. [118] and Robertson et al. [106]. Undoped and 3 % K doped sintered discs and films were prepared by Kudo et al [116]. The transparency remains almost same ($\sim 70\%$ to 75%) for both types of films whereas the conductivity increased slightly from $3.9 \times 10^{-3}\ S\ cm^{-1}$ to $4.8 \times 10^{-2}\ S\ cm^{-1}$.

Layered oxychalcogenide films: Layered-structure oxychalcogenide films of the form $(LaO)CuC^h$ ($C^h =$ Chalcogenides e.g. S, Se) [115, 119] showed high optical transparency and reasonable p-type conductivity to become promising material for ‘‘Transparent Electronics’’. Although this material was first prepared almost two decades ago by Palazzi [120] and its p-type conductivity was reported more than a decade ago [121, 122], but Ueda, Hiramatsu and co-authors first prepared it in transparent thin film form to extend its application into p-TCO technology [115, 119]. Also this material shows room-temperature band edge emission under UV-excitation, extending its application in light emitting devices (LEDs) and similar fields [123-129]. Crystallographic parameters of these materials were extensively studied by Palazzi [120] as well as by others [121, 130-131]. Also band structure calculations were done by Inoue et al. [132]. Different physical properties of the material were also studied by various groups [133-135].

Non-oxide Cu-based transparent semiconductors: There are reports on the fabrication of non-oxide p-type transparent conductors like Cu_2BaS_2 , $CuBaSF$ [136-138] etc. Park and co-authors [136] synthesized $\alpha-Cu_2BaS_2$ thin film, which crystallizes at low temperature in orthorhombic structure [139]. They obtained a visible transmittance of 70 % for a 430 nm

thick film with a rather low bandgap of 2.3 eV. The room-temperature conductivity was reported as 17 S cm^{-1} with a Hall mobility of $3.5 \text{ cm}^2 \text{ V}^{-1} \text{ S}^{-1}$. Later the same group reported the preparation of undoped and K doped CuBaSF pellets and thin films [138]. The transmittance of the undoped film was $\sim 85 \%$ in the visible region with an estimated direct bandgap value of 3.2 eV. A decrease in the transmittance with increase in the K-dopant was observed for the doped films. Room-temperature conductivity of the polycrystalline thin film was obtained as 1.0 S cm^{-1} . Although these materials cannot be classified as p-TCO, but still they have scientific importance in the field of “Transparent Electronics”.

2.1.3. Deposition Techniques

Growth technique of thin films plays the most significant role on the properties of the films. Different deposition routes yield films with diverse structural, optical and electrical properties. Even for the same deposition technique, slight variation in the deposition parameters produce films with different properties. So it is very important to have a comparative study on the properties of various films produced by different deposition routes. Detailed description of different deposition techniques along-with their schematic diagrams and related parameters are reported in various literatures [5, 8, 140-143].

CuAlO_2 thin films prepared by various techniques include pulsed laser deposition (PLD) [64, 67, 144, 145], R. F. magnetron sputtering [145], R. F. magnetron reactive co-sputtering of Cu and Al metal targets [146], D. C. reactive sputtering of facing targets of Cu and Al metals and a rotating substrate [147], pulsed magnetron sputtering [148], chemical vapor deposition (CVD) [149-151], e-beam evaporation [152], wet-chemical solution growth technique [153], hydrothermal cation exchange reaction followed by spin-on technique [154], rapid thermal annealing [155], spray technique [156], sol-gel technique [157] etc. Also ion exchange method is used to prepare CuAlO_2 powder from LiAlO_2 [158]. Although no film preparation was reported by this method but this process may become an important target preparation procedure for PLD or sputtering. Similarly, hydrothermal process [159] had been adopted to synthesize CuAlO_2 and Ga doped CuAlO_2 solid solutions. Previously, we have reported the syntheses of phase pure p- CuAlO_2 thin films by D. C. sputtering of sintered pellet of copper aluminum oxide [160] as well as reactive sputtering of a mixture of Cu and Al metal target pellets in oxygen diluted Ar atmosphere [161]. Wet-chemical deposition of highly oriented CuAlO_2 thin film has also been carried out by us [92, 162], which showed very good optical properties.

Also, based on ab initio electronic structure calculations, new methods have been proposed by Yoshida and co-authors [163-164] to fabricate high-conducting p- CuAlO_2 . They proposed that in thermal non-equilibrium PLD or molecular beam epitaxy (MBE) crystal growth techniques, induction of high concentration of Cu vacancies, to form impurity band, by reducing the Cu vapor pressure during deposition might enhance the p-type conductivity in the material. On the other hand, doping of Mg or Be at Al-sites to form acceptor levels by decreasing the Al vapor pressure and increasing the Cu vapor pressure during low temperature PLD, MBE or MOCVD process might also increase the p-type conductivity of the material. Optical and Electrical properties of CuAlO_2 thin films synthesized by various growth techniques are furnished in Table 3.

Table 3. Optical and Electrical properties of CuAlO₂ thin films synthesized by various growth techniques.

Growth Technique	Thickness (nm)	Avg. Visible Transmittance (%)	Room-Temp. Conductivity (S cm ⁻¹)	E _a (meV)	Carrier density (cm ⁻³)	Ref.	Remarks
PLD	500	70	0.095	~ 200	1.3 x 10 ¹⁷	64	---
PLD	230	80	0.34	220	2.7 x 10 ¹⁹	67	Films were post-annealed in O ₂ atmosphere (1.3 Pa)
R. F. Sputtering	180	85	---	---	---	145	Preliminary Hall and TEP measurements confirmed p-type conductivity
R. F. Magnetron Reactive Co-Sputtering	250	20 – 80	---	---	---	146	Small amount of CuO was present in the film
Pulsed magnetron sputtering	20	85-95	0.20	---	---	148	Film deposited directly from a blended Cu ₂ O/Al ₂ O ₃ powder target.
Reactive D. C. Sputtering	400 – 800	50 – 60	0.01 – 0.1	---	---	147	With facing metal targets and rotating substrate. Films were annealed at 1050 °C in N ₂ atmosphere.
MOCVD	250	40	2.0	120	2.6 x 10 ¹⁹	150	The films were a mixture of CuAlO ₂ , Cu ₂ O and CuAl ₂ O ₄ .
PE-MOCVD	120	40	17.08	32	1.17 x 10 ²⁰	149	For those samples annealed in air for 5 min (at 350 °C)
E-beam evaporation	---	50 - 85	1.0	---	10 ¹⁸ -10 ²⁰	152	Hole concentration decreases with increasing water vapor pressure
Dip-coating	1000	---	5 x 10 ⁻³	---	---	153	Results given for films deposited via Nitrate route.
RTA	360	60	0.57	---	---	155	RTA was performed over 1000 °C.
Hydrothermal cation exchange	420	60	2.4	140	5.4 x 10 ¹⁸	154	Film is nanocrystalline in <i>nature</i> with grain size around 14-16 nm
Spray pyrolyses	1000	30 - 70	---	---	---	156	Transmittance increases as Cu:Al ratio approaches to 1.0
Sol-Gel synthesis	1100	---	0.004	---	---	157	High resistivity is due to porous structure of the film.

2.2. Transparent Junctions

Junctional devices fabricated by both n and p types of TCO thin films are the key structure for “Invisible Electronics” [65]. The simplest of them is the p-n junction diodes with rectifying properties. The importance of these types of devices lies in the fact that ‘functional windows’ can be fabricated by these devices, which would transmit the visible solar radiation but absorb the UV part [64]. Therefore, simultaneously these devices can act as ‘UV-shields’ as well as ‘electricity generators’ by the UV absorption. A schematic diagram of all-TCO diode is shown in Fig. 2(c). Fabrication of a number of all-TCO junctional devices have been reported, which include both p-n and p-i-n homo-junctions and hetero-junctions as well as transparent field effect transistors (TFET) .

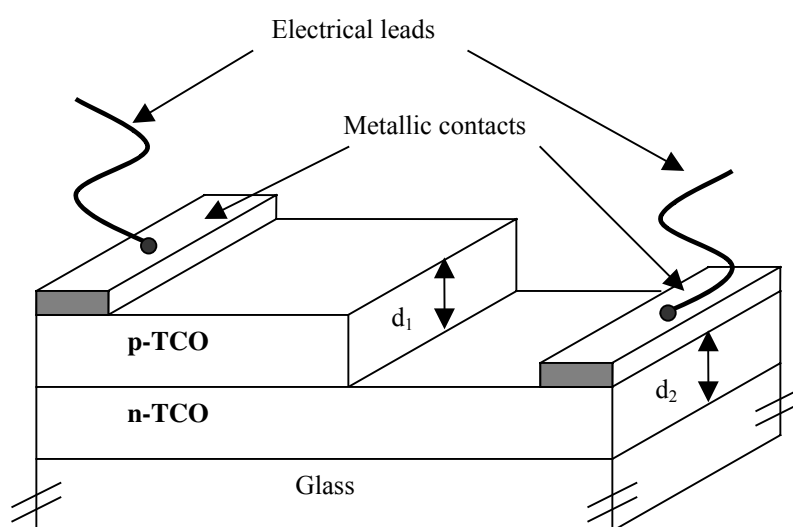


Figure 2(c). Schematic diagram of an all-TCO p-n junction diode on glass substrate.

Heterojunction: The first all-TCO diodes were reported by Sato and co-authors [66]. They fabricated a semi-transparent thin film p-i-n structure consisting of p-NiO / i-NiO / i-ZnO / n-ZnO: Al. The rectifying properties of the structure confirmed the formation of the junction. Similarly, fabrication of all-TCO p-n hetero-junction thin film diode of the form p-SrCu₂O₂ / n-ZnO was reported by Kudo and co-authors [165]. The same group also reported UV emission from a p-n hetero-junction diode composed of p-SrCu₂O₂ / n-ZnO after current injection through it [166-169]. P-i-n hetero-junction in the form of p-SrCu₂O₂: K / i-ZnO / n-ZnO was also constructed by this group [168]. Similarly p-i-n hetero-junction of the form p-CuYO₂: Ca / i-ZnO / n-ITO was fabricated by Hoffman et al [170]. Jayaraj and co-authors [110, 171] fabricated p-n hetero-junction using p-CuY_{1-x}Ca_xO₂ (x = 0.01-0.02) / n-Zn_{1-x}Al_xO (x = 0.02) structure. Tonooka and co-authors [172] reported the fabrication of n-ZnO/p-CuAlO₂ diode structure with rectifying characteristics and observed a photovoltaic effect (as large as 80 mV) under illumination of blue radiation. Although the performance of the diode was restricted by the low crystallinity of the CuAlO₂ layer but the forward-to-reverse current

ratio showed a moderate value of 90 between -1.5 to $+1.5$ volt. Also the transparency of the structure was 40 % to 70 % in the visible region.

Homojunction: Besides hetero-junctions, fabrications of p-n homo-junctions were also reported by few authors. Importance of the homo-junctions lies in the fact that lattice matching is supposed to be automatic during the formation of diodes. First all-delafossite p-n homo-junction diode was fabricated by Yanagi and co-authors [103] of the form YSZ (111) / ITO / p-CuInO₂: Ca / n-CuInO₂: Sn / ITO. Similarly all-ZnO p-n homo-junctions were reported by Hwang and co-authors [173], Tüzemen and co-authors [174] and Aoki and co-authors [175]. Hwang et al [173] fabricated n-ZnO: Al / p-ZnO: As and observed rectifying characteristics with a turn-on voltage around 2.5 volt. Tüzemen et al [174] reported intrinsic p and n-type ZnO homo-junction, prepared by reactive R. F. magnetron sputtering. The n-type and p-type conductivities were obtained by varying O₂ partial pressure in the Ar + O₂ sputtering atmosphere. It is worthwhile to be noted that the first report on p-type conductivity in intrinsic ZnO was published by Butkhuzi and co-authors [176], where post-annealing of the as-grown material in atomic oxygen atmosphere was performed to achieve intrinsic p-type conductivity. Aoki et al [175] fabricated p-ZnO: P / n-ZnO homo-junction and observed rectifying I-V characteristics. If the carrier concentration can be increased by optimizing the deposition parameters then these all-ZnO diode structures may open up a new horizon in the field of “Transparent Electronics”. Parameters of different all-transparent diodes are compared in Table 4(a).

TFET: Another important area in the field of “Transparent Electronics” is the fabrication of transparent field-effect transistors (TFET) [177]. A schematic diagram of top-Gated TFET is shown in Fig. 2(d). Prins and co-authors [178, 179] reported the fabrication of ferroelectric TFETs, based on transparent SnO₂: Sb thin films. They have observed the field-effect mobility around $10 \text{ cm}^2\text{V}^{-1}\text{s}^{-1}$, with an on/off current ratio $\sim 10^4$. Later various groups [180-181] reported the fabrication of ZnO based TFETs with reasonable device properties. Hoffman et al [180] reported 75 % visible transparency in their ZnO-TFETs with mobility and on/off ratio around $2.5 \text{ cm}^2\text{V}^{-1}\text{s}^{-1}$ and 10^7 respectively. Masuda et al [181] observed these values around $1.0 \text{ cm}^2\text{V}^{-1}\text{s}^{-1}$ and 10^5 respectively, with optical transmittance more than 80 % in the visible region. Similarly Carcia et al [182] obtained these values around $2.0 \text{ cm}^2\text{V}^{-1}\text{s}^{-1}$, 10^6 and >80 % respectively for their ZnO-TFETs. Recently, Nomura, Ohta and co-authors [183, 184] reported the successful fabrication of high mobility top-gate TFETs based on single crystalline transparent InGaO₃(ZnO)₅ thin film. The device shows the mobility as high as $80 \text{ cm}^2 \text{ V}^{-1}\text{s}^{-1}$ with on/off current ratio $\sim 10^6$ and more than 80 % transparency in the visible and near infra-red region. The deposition techniques for the fabrication of these TFETs include pulsed laser deposition (PLD) [178, 179, 181], ion beam sputtering [180], r.f. magnetron sputtering [181], reactive solid-phase epitaxy [183] etc. The deposition routes and various parameters of different TFETs are furnished in Table 4(b). These reports provide a significant step towards the realization of “Invisible Electronics”.

Table 4(a). Parameters of deferent all-transparent diodes

Diode structure		n-ZnO/ p-SrCu ₂ O ₂	n-ZnO/ p-SrCu ₂ O ₂ :K	n-ZnO:Al/ p-CuYO ₂ :Ca	n-ZnO/ p-CuAlO ₂	n-CuInO ₂ :Sn / p-CuInO ₂ :Ca	n-ZnO: Al/ p-ZnO: As	n-ZnO/ p-ZnO
Thickness (nm)	p-layer	300	200	300	400	400	1500-2000	5000
	n-layer	300 – 1000	200	250	400	400	600	5000
Carrier concentra-- tion (cm ⁻³)	p-layer	10 ¹⁷	~10 ¹⁸	---	---	---	---	~ 5 x 10 ¹⁵
	n-layer	5 x 10 ¹⁸	~10 ¹⁸	---	---	---	---	~ 6 x 10 ¹⁵
Substrate		Glass	YSZ (111)	Glass	Glass	YSZ (111)	GaAs (001)	Si (100)
Deposition technique	p-layer	Reactive co- evaporation in O ₂ atmosphere	PLD	Reactive co- evaporation in O ₂ atmosphere	PLD	PLD	R. F. Magnetron sputtering	R. F. Magnetron reactive sputtering
	n-layer	Magnetron sputtering	PLD	R. F. Magnetron sputtering	PLD	PLD	R. F. Magnetron sputtering	R. F. Magnetron reactive sputtering
Electrodes	p-side	ITO	Ni	In	ITO	ITO	In	Au/Al
	n-side	n ⁺ -ZnO	ITO	ITO	n ⁺ - ZnO	ITO	In	Au/Al
Turn-on voltage (V)		~ 0.5	~ 1.0	0.4 – 0.8	0.4 – 1.0	1.8	~ 2.5	~ 1.0
Reference		165	166	110	172	103	173	174

Table 4(b). Parameters of various TFETs

Active Channel	Gate Insulator	Gate Electrode	Substrate used	Mobility ($\text{cm}^2\text{V}^{-1}\text{s}^{-1}$)	On/off ratio	Visible Transparency (%)	Ref
SnO ₂ : Sb (Thickness ~ 110 nm) (Deposition technique: PLD)	PbZr _{0.2} Ti _{0.8} O ₃ (Thickness ~ 160 nm) (Deposition technique: PLD)	SrRuO ₃ (Thickness ~ 140 nm) (Deposition technique: PLD)	SrTiO ₃ (100)	10.0	~ 10 ⁴	Transparent, as seen in the figure provided, but no numerical data given.	178* 179
ZnO (Thickness ~ 100 nm) (Deposition technique: PLD)	Al ₂ O ₃ + TiO ₂ [#] (Thickness ~ 220 nm) (Deposition technique: ALD)	ITO (Thickness ~ 200 nm) (Deposition technique: Sputtering)	Glass	2.5	~ 10 ⁷	75	180
ZnO (Thickness ~ 140 nm) (Deposition technique: PLD)	SiO ₂ + SiN _x [†] (Thickness ~ 250 & 50 nm respectively) (Deposition technique: PECVD)	ITO (Thickness ~ 100 nm) (Deposition technique: e-beam evaporation)	Glass	1.0	10 ⁵	80	181
InGaO ₃ (ZnO) ₅ [‡] (Thickness ~ 120 nm) (Deposition technique: PLD)	a-HfO ₂ (Thickness ~ 80 nm) (Deposition technique: PLD)	ITO (Thickness ~ 30 nm) (Deposition technique: PLD)	YSZ (111)	80.0	~ 10 ⁶	80	183 ^{**}

* Due to the presence of ferroelectric insulator PbZr_{0.2}Ti_{0.8}O₃, the device showed intrinsic memory function.

[#] Al₂O₃ + TiO₂ is an alternative layers of Al₂O₃ & TiO₂.

[†] This TFET has a double layer Gate insulator.

[‡] Single-crystalline InGaO₃(ZnO)₅ is used as active channel layer.

^{**} The device has a top gate structure.

Table 5(a). Electro-optical properties of nanostructured CuAlO₂ thin films synthesized by various processes.

Process	Avg. particle size (nm)	Band-gap (eV)	Room-temp. conductivity (S cm ⁻¹)	Carrier concentration (cm ⁻³)	Ref	Remarks
MO-CVD	10	3.75	2.0	1.8×10^{19}	150	The film contains nanocrystalline phases of CuAlO ₂ and Cu ₂ O.
Spin-on technique	10	3.75	2.4	5.4×10^{18}	154	Initially CuAlO ₂ nanocrystalline powder was prepared by hydrothermal cation exchange reaction between NaAlO ₂ and CuCl. Then the powder was dispersed in alcohol and deposited as thin film.
Sputtering	~10	3.94	---	---	185	Deposition time was varied to decrease the particle size. With decrease in the particle size, an increase in the bandgap is observed due to quantum confinement effect. Also room-temp. photoluminescence properties were observed first time in these nanocrystalline CuAlO ₂ thin films.

Table 5(b). Progress in the development of F-N theory and F-N equation.

Theory	Author(s)	Year	Assumptions and remarks	Ref.
'Original' F-N theory	R. H. Fowler and L. Nordheim	1928	The authors treated the effect as wave-mechanical tunneling through a triangular potential barrier. They have carried out an exact solution of the Schrödinger equation for a simple triangular barrier.	209
'Standard' F-N theory	E. L. Murphy and R. H. Good Jr.	1956	These authors used more realistic barrier and introduced 'exchange-and-correlation interaction' between the emitted electron and the surface, into the original F-N theory.	210
'Modified' standard F-N theory	H. A. Schwetman, J. P. Turneaure, and R.F. Waites	1974	These authors introduced the local field enhancement factor 'β'. β was initially postulated to arise from the geometrical irregularities on the emitting surface.	211
Latham's model for 'field enhancement'	R. V. Latham	1983	This model introduced field enhancement due to semiconducting or insulating materials on the emitting metal surface.	212
'Generalized' F-N equation	R. G. Forbes	1999	This equation combined various models for F-N theory and depended on the particular assumption(s) and approximation(s) made. The proper choice of the 'generalized correction factors' in the generalized F-N equation would lead to the required F-N equation.	214
'ENH' theory	R. G. Forbes	2001	The emitting films are assumed to be 'electrically nanostructured heterogeneous' (ENH) materials, where internal nanostructure creates geometrical field enhancement inside and at the film-vacuum interface. Thus the macroscopic field is enhanced by a factor, β, to produce the required barrier-field for electron tunneling.	213

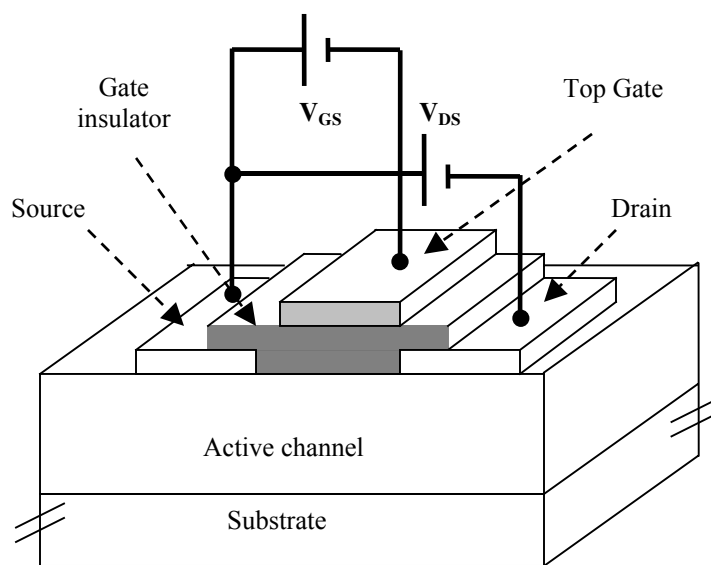


Figure 2(d). Schematic diagram of a top-gated TFET structure. After [183].

2.3. Nanostructured p-CuAlO₂ Thin Films

As far as syntheses of nanocrystalline CuAlO₂ thin film is concerned, Gong and co-authors [150] first reported the preparation of phase impure copper aluminum oxide films by chemical vapor deposition (CVD) method, which contain nanocrystalline phases of CuAlO₂ and Cu₂O. They have used metalorganic precursors Cu(acac)₂ and Al(acac)₃ (acac = acetylacetonate) as the source material. The crystallite size was found to be below 10 nm with an optical bandgap of 3.75 eV. The carrier concentration was $\sim 10^{19} \text{ cm}^{-3}$ [150]. Also later, Gao and co-authors [154] reported the synthesis of phase pure nanocrystalline CuAlO₂ thin film by spin-on technique. Initially CuAlO₂ nanocrystalline powder was prepared by hydrothermal cation exchange reaction between NaAlO₂ and CuCl. Then the powder was dispersed in alcohol and deposited as thin film on glass substrates by spin-on technique [154]. The average grain size obtained by this group was around 10 nm with an optical bandgap around 3.75 eV. The room temperature conductivity was found to be 2.4 S cm^{-1} with a hole concentration around 10^{18} cm^{-3} . We have also reported the synthesis of CuAlO₂ nanoparticles by D. C. sputtering technique from a sintered disk of copper aluminum oxide [185]. The particle size was found to be as low as 10 nm. We have observed an increase in the particle size with an increase in the deposition time. Also an increase in the bandgap from 3.60 to 3.94 was observed with the decrease in the particle size. And this bandgap enhancement is attributed to the quantum confinement effect as often found in semiconductor nanocrystals. Various opto-electronic properties of nanocrystalline CuAlO₂ thin film are furnished in Table 5(a). We have also observed for the first time some photoluminescence properties of nanocrystalline CuAlO₂ thin films and tried to explain it with existing theories [185]. Photoluminescence properties of p-type transparent semiconducting layered oxysulphide thin films of LaO(CuS) have been reported previously by Ueda and co-authors [115]. Also, as far

as luminescence properties of copper based delafossite oxide materials are concerned, Jacob and co-authors [186] reported the luminescence properties of CuLaO_2 and CuYO_2 pellets.

2.4. Wide Bandgap Field-Emitters

It was found that the materials with wide bandgap (such as diamond) have low or negative electron affinity, which, in turn, enhances the low-macroscopic field emission properties of diamond films [81]. Also p-type semiconducting diamond film showed low-threshold field emission properties [82]. As far as the field emission from other wide bandgap thin films is concerned, GaN and AlN showed very good field emission properties. Polycrystalline GaN films [187] as well as nanostructured GaN, in the form of nanorods [188], nanobelts [189], nanoneedles [190], nanowires [191] etc. showed very low threshold field emission properties. Similarly, oriented AlN [192, 193] and nanostructured AlN [194-197] also showed very good field emission properties.

As far as field emission properties of various TCOs are concerned, Olesik et al. [198] reported the field emission properties of Sb and Sn doped Indium tin oxide (ITO) thin films under an average external field of $5 \text{ V}\mu\text{m}^{-1}$. Similarly, Baranauskas and co-authors [199] reported the field emission properties of SnO_2 thin films and observed that the deposition temperature had a dramatic influence on the electron emission properties of the material. Also nanostructured ZnO films have recently generated great interest in the field of FED technology due to their superior field emission properties over carbon based field emitters. ZnO nanowires [200-202], nanoneedles [203] etc. have been reported to show excellent low-threshold cold field emission properties. Previously, our group also reported very good field emission properties of ZnO nanowires [204-205] synthesized by catalyst free solution route. The enhanced field emission properties of this material were attributed to the geometrical structure of the nanowires, due to which considerable field enhancement was manifested at the emitter tip to show low-threshold field emission. Also recently, Yang et al. [206] observed that a nanocomposite film composed of ZnO nanowire and amorphous diamond layer showed remarkable enhancement in the field-emission properties over the intrinsic diamond and ZnO films. This is very important in the sense that both diamond, being a robust material, and ZnO, a highly chemically stable and structurally rigid material, a nanocomposite of these two may produce much stable field emitters for diverse applications. As far as the field emission properties of wide bandgap p-CuAlO₂ thin film is concerned we have first reported its field emission properties and tried to explain the field emission mechanism therefrom [207, 208].

The emission of electrons from a metal-vacuum interface, in the presence of an external electric field normal to the emitting surface, was initially treated as a quantum mechanical tunneling process by Fowler and Nordheim ('original' F-N theory)[209]. Later, Murphy and Good [210] proposed a more rigorous theory, called 'standard F-N theory', where the 'exchange-and-correlation interaction' between the emitted electron and the surface was included into the original F-N theory [209]. Schwettman et al. [211] further modified the 'standard F-N theory' by introducing the local field enhancement factor ' β '. β was initially postulated to arise from the geometrical irregularities on the emitting surface, but later Latham [212] proposed a model, which introduced field enhancement due to semiconducting or insulating materials on the metal surface. Extending the Latham's model, Forbes [213] tried to explain the low-macroscopic field emission of various films by assuming that the thin

films are ‘electrically nanostructured heterogeneous’ (ENH) materials, where internal nanostructure creates geometrical field enhancement inside the film as well as at the film-vacuum interface. Thus the macroscopic field is enhanced by a factor, which can be related to the above mentioned field-enhancement factor β , to produce the required barrier-field for electron tunneling. In fact, as the original F-N theory (so also F-N equation) [209] is based on certain assumptions, any deviation from one (or more) of these assumptions, leads to some ‘specialized versions’ of elementary F-N equation. So, Forbes proposed a ‘generalized F-N equation’ [214], whose form in a given case depends on the particular assumption(s) and approximation(s) made. He showed that the proper choice of the ‘generalised correction factors’ in the generalized F-N equation, leads to the standard F-N equation, proposed by Murphy and Good [210], which was the first fully satisfactory treatment of standard physical assumptions. The development in the F-N theory is tabulated in Table 5(b). In fact there are many different mechanisms involved as the electrons, in the presence of an external electric field, travel through the bulk of the film to the surface via

different interfacial contacts, followed by the emission to vacuum, propagated through the electrode gap and finally reaching the anode. The exact *nature* of these mechanisms is yet to be explored completely.

3. Origin of P-type Conductivity in P-TCO

Most of the existing TCOs are n-type, whereas it is very difficult to prepare binary metal oxides with p-type conductivity. A possible reason for this has been described by Kawazoe et al. [64, 144], where they argued that this is probably because of the electronic structure of these metal oxides. Strong localization of holes (it can be successfully introduced by intentional substitutional doping or by producing non-stoichiometry within the material) at oxygen 2p levels or an upper edge of the valence band due to high electronegative *nature* of oxygen, i.e. this localization is due to the ionicity of metallic oxides. O 2p levels are far lower lying than the valence orbit of metallic atoms [215], leading to the formation of deep acceptor level by the holes. In other words, the holes, therefore, have high probability to be localized around the oxygen atoms. Hence these holes require high enough energy to overcome large barrier height in order to migrate within the crystal lattice, resulting in poor conductivity and hole mobility.

A possible solution proposed by Kawazoe and co-authors [144] is to introduce a “degree of covalency” in the metal-oxygen bondings to induce the formation of an extended valence band structure, i.e. the valence band edge should be modified by mixing orbitals of appropriate counter cations that have energy-filled-levels comparable to O 2p level. This would reduce the strong coulombic force by oxygen ions and thereby delocalizing the holes. This is the essential approach to obtain p-TCO, which is called “Chemical Modulation of the Valence Band (CMVB)” [144].

But the next requirement is the choice of appropriate cationic species that will serve for CMVB technique. Investigations showed that the required cationic species are $3d^{10}$ -closed shell of Cu^+ ions and $4d^{10}$ -closed shell of Ag^+ ions [144, 215]. Although some transition metal cations with open d-shell may fulfill the energy requirement [216] for CMVB technique, but they usually show strong coloration due to d-d transition, which is not expected for transparent materials. Hence focus had been concentrated on the cations

mentioned above, with closed ($d^{10}s^0$) electronic configuration. Fig. 3 shows a schematic illustration of CMVB technique. Both of the atomic orbitals are occupied by electron pairs, and the resulting antibonding level becomes the highest occupied level, i.e. the valence band edge.

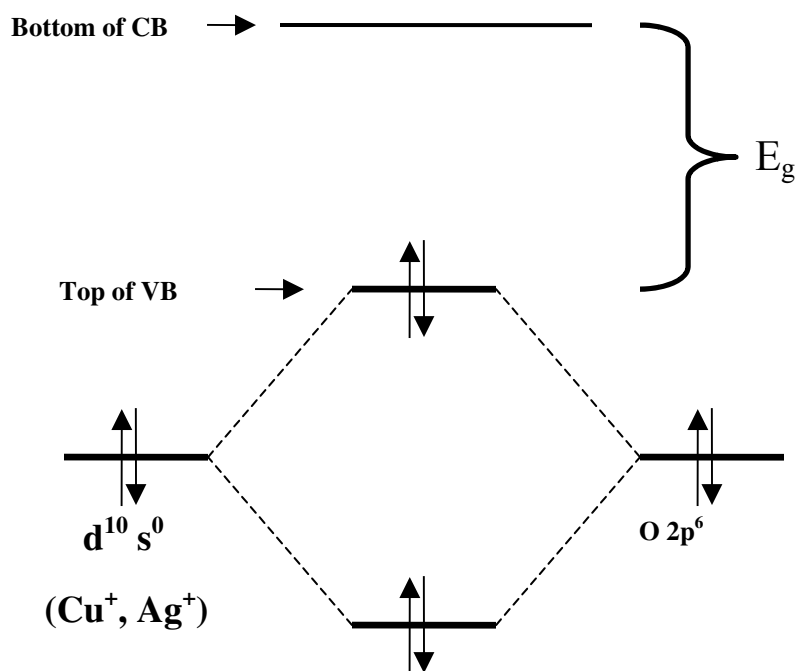


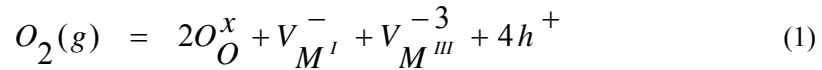
Figure 3. Schematic diagram of CMVB method. Energy levels are to the scale. After Ref. [144].

Next is the structural requirement for designing p-TCO materials. Tetrahedral coordination of oxide ions is advantageous for p-type conductivity, as it acts in reducing the localization behavior of 2p electrons on oxide ions [144]. The valence state of the oxide ions can be expressed as sp^3 in this conformation. Eight electrons (including $2s^2$) on an oxide ion are distributed in the four σ bonds with the coordination cations. This electronic configuration reduces the non-bonding nature of the oxide ions and increases the delocalization of holes at the valence band edge (that is why Cu_2O is a p-type conducting oxide [217-220]). But Cu_2O , although p-type in nature, has rather small bandgap (2.17 eV) [218]. This is probably because of the three-dimensional interactions between $3d^{10}$ electrons of neighboring Cu^+ ions. It is expected that the low-dimensional crystal structure would suppress this interaction [67]. As we are interested in transparent conducting oxides, bandgap of the material (E_g) should be greater than 3.1 eV. Hence enlargement of bandgap would be another structural requirement for designing p-TCO, so that there is no absorption of visible photons. Materials with delafossite crystal structure $\text{M}^{\text{I}}\text{M}^{\text{III}}\text{O}_2$ (M^{I} = Monovalent ions, Cu^+ , Ag^+ ; M^{III} = Trivalent ions, Al^{+3} , Ga^{+3} , In^{+3} , Cr^{+3} , Fe^{+3} , Co^{+3} , Sc^{+3} , Y^{+3} etc.) [93-95] were chosen as the candidates for p-TCOs for several reasons. Firstly, if we investigate the delafossite structure as shown in Fig. 2(a), we see an alternative stacking of M^{I} and layers of nominal $\text{M}^{\text{III}}\text{O}_2$ composition consisting $\text{M}^{\text{III}}\text{-O}_6$ octahedra sharing edges. Each M^{I} atom is linearly coordinated with two oxygen atoms

to form a O-M^I-O dumbbell unit placed parallel to the c-axis. O-atoms of O-M^I-O dumbbell link all M^I layers with the M^{III}O₂ layers. On the other hand, each oxide ion in the M^{III}O₂ layer forms a “pseudo-tetrahedral coordination (M^{III}₃M^IO)” [144] with the neighboring M^{III} and M^I ions. Hence, as previously mentioned, this electronic configuration reduces the non-bonding *nature* of the oxide ions and, therefore, delocalizes the holes at the valence band edge. Secondly, this layered structure (O-M^I-O dumbbell layer and M^{III}O₂ layer) effectively reduces the dimension of cross-linking of M^I ions and, thus enlarging the bandgap [64]. And finally, another important factor in this structure, is the low coordination number of the M^I ions, due to the large separation from oxygen legands, which is the result of the strong coulombic repulsion between 2p electrons in oxygen legands and M^I d¹⁰ electrons. This leads to the M^I d¹⁰ energy levels almost comparable to the O 2p level, resulting in a high degree of mixing of these levels, which is essential for CMVB technique [144].

As the importance of p-TCO lies in the active device fabrication, it is very important to have lattice matching between both p and n-types of TCOs to form p-n homojunctions. Both types of TCOs with delafossite structure may serve this requirement. In this regard, it is also worthwhile to mention that the M^{III}O₂ layers of this structure is also important for designing n-TCOs, specially for the cations like Ga⁺³, In⁺³ in the M^{III} sites with s⁰ configuration [144]. Following the above argument, delafossite AgInO₂ thin film with n-type semiconductivity had already been established [221].

Non-stoichiometry and doping in p-TCO: The cause of p-type conductivity shown by p-type transparent conducting oxide materials is due to excess oxygen (or metal deficit) within the crystallite sites of the material, i.e. the defect chemistry plays an important role. This deviation from the stoichiometric composition of the components can be induced by regulating the preparation condition of the materials. The defect reaction may be represented by the following equation [222, 223]:



where ‘O_O’ denotes the lattice oxygen, ‘V’ denotes the vacancies of monovalent cation M^I and trivalent cation M^{III} respectively and ‘h’ denotes the hole. Superscripts ^x, ⁻, and ⁺ denote effective neutral, negative, and positive charge states respectively.

Also, intercalation of excess O⁻² ions in the interstitial sites may trap electrons, leaving behind empty states in the valence band, which act as holes. The formula for oxygen-excess delafossite films may be written as M^IM^{III}O_{2+x} (M^I = Cu⁺, Ag⁺ and M^{III} = Al⁺³, Ga⁺³, In⁺³, Y⁺³, Sc⁺³ cations etc.). The value of x i.e. the percentage of excess oxygen may be as low as 0.001 % in CuAlO_{2+x} thin film [65] to more than 25 % in CuYO_{2+x} polycrystalline powder and CuScO_{2+x} thin films [89, 224-226]. Fig. 4(a), 4(b) and 4(c) show schematic representation of stoichiometric ABO₂ crystal and non-stoichiometric ABO₂ crystal with “excess” oxygen in lattice sites and interstitial sites.

Oxygen intercalation in delafossite p-TCOs only showed a maximum reported conductivity around 3 x 10¹ S cm⁻¹ [108]. But this is still quite less than that of commercially available n-TCOs like indium tin oxide (ITO), which is having room temperature conductivity more than 1 x 10³ S cm⁻¹. So next attention was focused on the substitutional doping of these materials by appropriate dopants to increase the conductivity. Doping of

CuAlO_2 was first attempted, as it was the first reported material amongst p-TCOs. Several groups theoretically calculated the effects on the electronic behavior of the material due to the presence of various cations in Cu and (or) Al sites. Lalić and co-authors [227, 228] showed that Cd and Zn substitutions on Cu site would produce n-type conductivity in the material, whereas Ni doping in Cu sites would enhance the p-type conductivity of the material. But Cd doping on Al sites would have no effect on the electrical properties of the material. Preparation of a solid solution of gallium doped copper aluminum oxide in the form of $\text{CuAl}_{1-x}\text{Ga}_x\text{O}_2$ ($0 \leq x \leq 0.5$) was reported by Shahriari et al [159]. But no film preparation of this material was reported by them. Also any other experimental data on the doping of CuAlO_2 thin film has yet been reported. Heavy doping ($\sim 50\%$) of CuGaO_2 by Fe^{+3} in Ga sites has

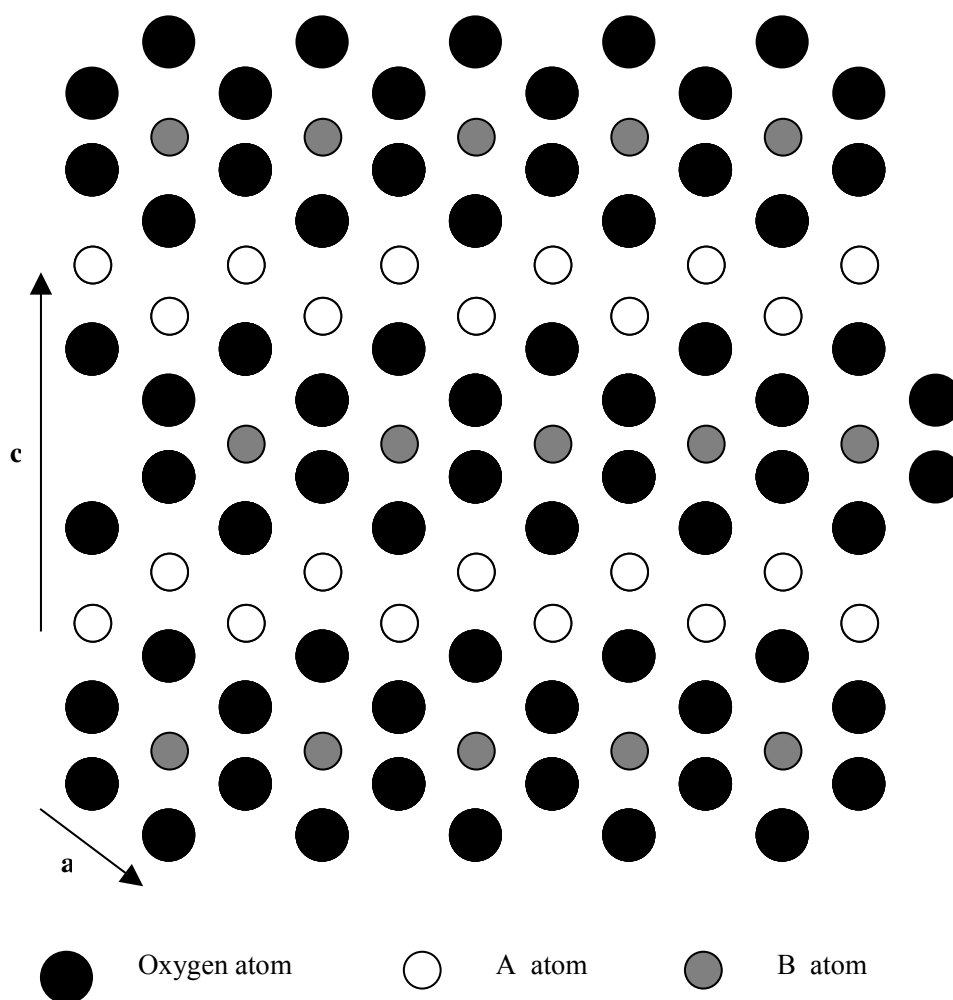


Figure 4(a). Stoichiometric ABO_2 lattice. The diagram is not according to the relative lattice parameters.

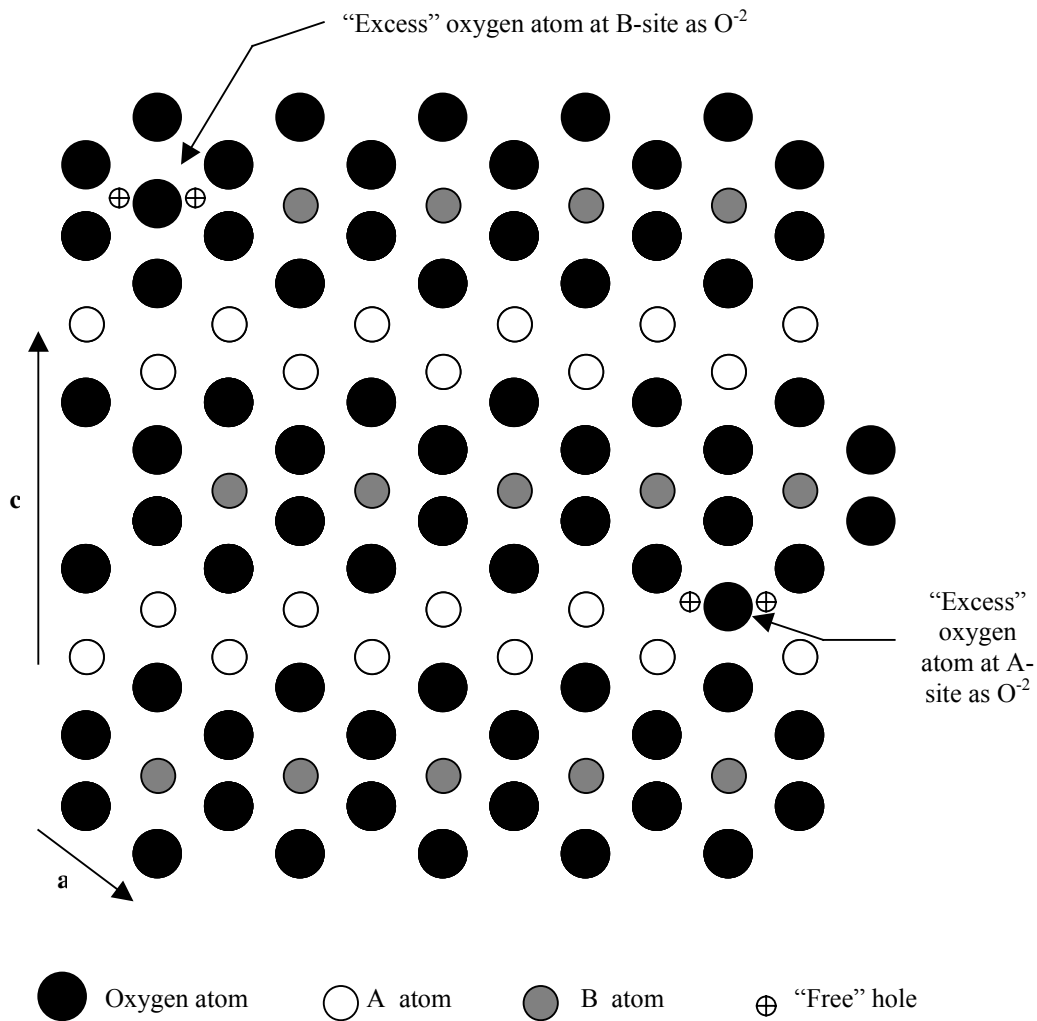


Figure 4(b). Non-stoichiometric ABO_2 structure with “excess” oxygen in lattice sites.

been reported by Tate et al. [88]. Their strategy was to combine high transparency of $CuGaO_2$ thin film ($\sim 80\%$ in visible region [101]) with better conductivity (over other Cu and Ag based delafossites [95]) of $CuFeO_2$ pellets (2.0 S cm^{-1} [95, 229]). Both the polycrystalline powder and thin film of $CuGa_{1-x}Fe_xO_2$ ($0 \leq x \leq 1$) have shown p-type conductivity. It was observed that high Fe doping had increased the conductivity of the film from $2 \times 10^{-2} \text{ S cm}^{-1}$ (for undoped $CuGaO_2$ thin film) to almost 1.0 S cm^{-1} for $CuGa_{1-x}Fe_xO_2$ ($x = 0.5$) thin film, whereas transparency of the films became $\sim 60\%$ in the visible region [88].

Doping of $CuInO_2$, $CuYO_2$, $CuScO_2$, $CuCrO_2$ by divalent cations e.g. Ca^{+2} , Mg^{+2} etc. were reported by various groups [88, 102-103, 108-110]. When a trivalent cation was

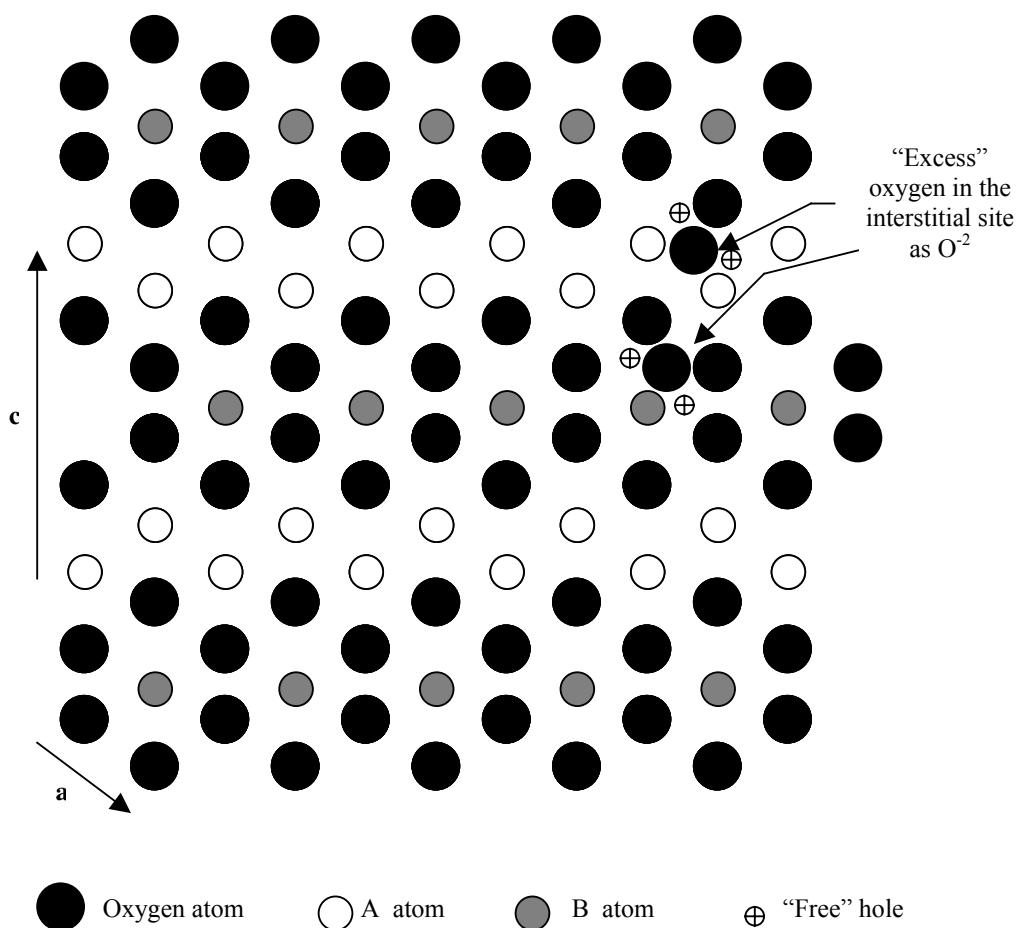
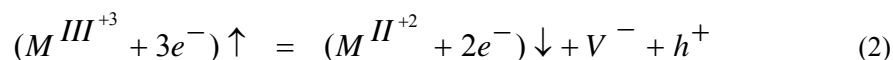


Figure 4(c). Non-stoichiometric ABO_2 lattice with “excess” oxygen at interstitial site.

replaced by a divalent one, one empty state in the valence band was created, which acts as a hole, thus increasing hole conductivity. The method may be described by the following equation:



where $M^{III^{+3}}$ and $M^{II^{+2}}$ are trivalent and divalent cations, V^- is a negatively charged vacant state, e^- and h^+ is an electron and “free” hole respectively. The symbols \uparrow and \downarrow denote the replacement of trivalent cation by divalent one in the lattice sites. Such doped delafossite films like $\text{CuCr}_{1-x}\text{Mg}_x\text{O}_2$ ($x = 0.05$), $\text{CuY}_{1-x}\text{Ca}_x\text{O}_2$ ($x = 0.01 - 0.02$), $\text{CuSc}_{1-x}\text{Mg}_x\text{O}_2$ ($x=0.05$) showed better hole conductivity over the corresponding undoped films.

Some Ag based delafossite materials like $\text{AgM}^{III}\text{O}_2$ ($M^{III} = \text{Sc}^{+3}, \text{Cr}^{+3}, \text{Ga}^{+3}$ etc.) with 5 % Mg doping at M^{III} sites was reported by Nagarajan et al. [89]. The conductivities of these

sintered powders were very low ($\sim 10^{-5} - 10^{-4} \text{ S cm}^{-1}$) and also no film preparation of these materials were reported anywhere so far.

There are also reports in the literature about the double substitution of trivalent M^{III} sites by divalent and pentavalent cations e.g. $\text{CuFe}_{1-x}\text{V}_x\text{O}_2$ ($x = 0.5$), $\text{CuNi}_{1-x}\text{Sb}_x\text{O}_2$, $\text{CuZn}_{1-x}\text{Sb}_x\text{O}_2$, $\text{CuCo}_{1-x}\text{Sb}_x\text{O}_2$, $\text{CuMg}_{1-x}\text{Sb}_x\text{O}_2$, $\text{CuMn}_{1-x}\text{Sb}_x\text{O}_2$ ($x = 0.33$), $\text{AgNi}_{1-x}\text{Sb}_x\text{O}_2$, $\text{AgZn}_{1-x}\text{Sb}_x\text{O}_2$ ($x = 0.33$) etc., but all in the form of sintered powder [90, 224]. Also triple substitution of trivalent cation had been reported by Tate and co-authors [88, 90] in the form of $\text{CuNi}_{1-x}\text{Sb}_x\text{Sn}_y\text{O}_2$ ($x = 0.3$, $y = 0.033$). Thin film of this material showed an average of 60 % transmittance with a room temperature conductivity of $5 \times 10^{-2} \text{ S cm}^{-1}$.

4. Syntheses of P-CuAlO_{2+x} Thin Films

Copper aluminium oxide (CuAlO_2) thin films were prepared by three routes:

- (a) Direct current (d.c.) sputtering of a prefabricated CuAlO_2 powder pellet,
- (b) Reactive d.c. sputtering of a mixture of copper and aluminium metal powder pellet in oxygen-diluted argon atmosphere.
- (c) Wet-chemical dip-coating technique from a solution of CuCl and AlCl_3 dissolved in HCl .

4.1. Synthesis of CuAlO_2 Films by D.C. Sputtering

The d.c. sputtering technique to prepare the film, involved the following three steps:

(i) CuAlO_2 powder preparation

Polycrystalline CuAlO_2 powder was synthesized by heating stoichiometric mixture of Cu_2O and Al_2O_3 according to the reaction: $\text{Cu}_2\text{O} + \text{Al}_2\text{O}_3 = 2\text{CuAlO}_2$. At first Cu_2O and Al_2O_3 powder (99.99 %) were taken with Cu / Al atomic ratio 1 : 1 and mixed for 1 hour. Then the mixture was heated in alumina boat at 1100°C for 24 hours. In every 6 hours the mixture was taken out of the furnace after proper cooling, remixed and placed into the furnace at the same temperature. The sintered body was reground and pressed into a pellet by hydrostatic pressure of about 200 kgf / cm^2 . These pellets were then placed into a grooved aluminium holder by appropriate arrangement, which was used as the target for sputtering.

(ii) Substrate cleaning

Before placing into the deposition chamber the glass substrates were cleaned at first by mild soap solution, then washed thoroughly in deionized water and also in boiling water. Finally they were ultrasonically cleaned in acetone for 15 minutes. Si substrates were first immersed in 20 % HF solution for 5 minutes for removing surface oxide layers. Then they were cleaned in deionized water and finally with alcohol in an ultrasonic cleaner.

(iii) Film deposition

Our sputtering system consists of a conventional vacuum system, which was evacuated to 10^{-6} mbar by rotary and diffusion pump arrangement. The chamber was back filled with Ar and O_2 (40 vol %) gas mixture. The target was pre-sputtered for 10 minutes to remove contamination, if any, from the surface and then the shutter was displaced to expose the substrates in the sputtering plasma. Si (400) and glass were used as substrates. The target was connected to the negative terminal of high voltage d.c. power supply and the substrate was placed on the ground electrode. Summary of the deposition conditions is shown in Table 6 and a photograph of the D. C. plasma generated during deposition is shown in Fig. 5. After the deposition was over, the films were post-annealed in the same vacuum chamber at 473 K for 30 minutes to 150 minutes (at pressure 0.2 mbar) maintaining the oxygen flow to induce nonstoichiometry in the film, which is an important precondition for enhancing p-type conductivity of the film.

Table 6. Summary of deposition parameters for D. C. sputtered films [160]

Electrode distance	:	1.8 cm
Sputtering Voltage	:	1.1 kV
Current Density	:	10 mA / cm^2
Substrates	:	Si (400), glass
Base pressure	:	10 ⁻⁶ mbar
Sputtering Gasses	:	Ar & O_2 (3 : 2 volume ratio)
Deposition Pressure	:	0.2 mbar
Substrate Temperature	:	453 K
Deposition Time	:	4 hr
Post-annealing time	:	30 to 150 min
Post-annealing temperature	:	473 K
Post-annealing atmosphere	:	O_2 (0.2 mbar)



Figure 5. Photograph of D. C. sputtering plasma.

4.2. Synthesis of CuAlO_2 Film by Reactive Sputtering

The reactive d.c. sputtering technique also involved three steps:

(a) Target preparation

Firstly, a mixture of ultra pure copper and aluminum powders (99.99 %) were taken with Cu / Al atomic ratio as 1 : 1 and then they were mixed thoroughly for 1½ hour. The mixture was then pelletized into a grooved aluminium holder by hydrostatic pressure of 150 Kgf / cm^2 to use as target for sputtering.

(b) Substrate cleaning

The substrates used, were glass and Si (400). The substrate cleaning procedure was same as that one described in Section 4.1.

(c) Film deposition

Negative terminal of the d.c. generator was connected with the target and the substrates were placed on the grounded electrode. Si (400) and glass were used as substrates for film

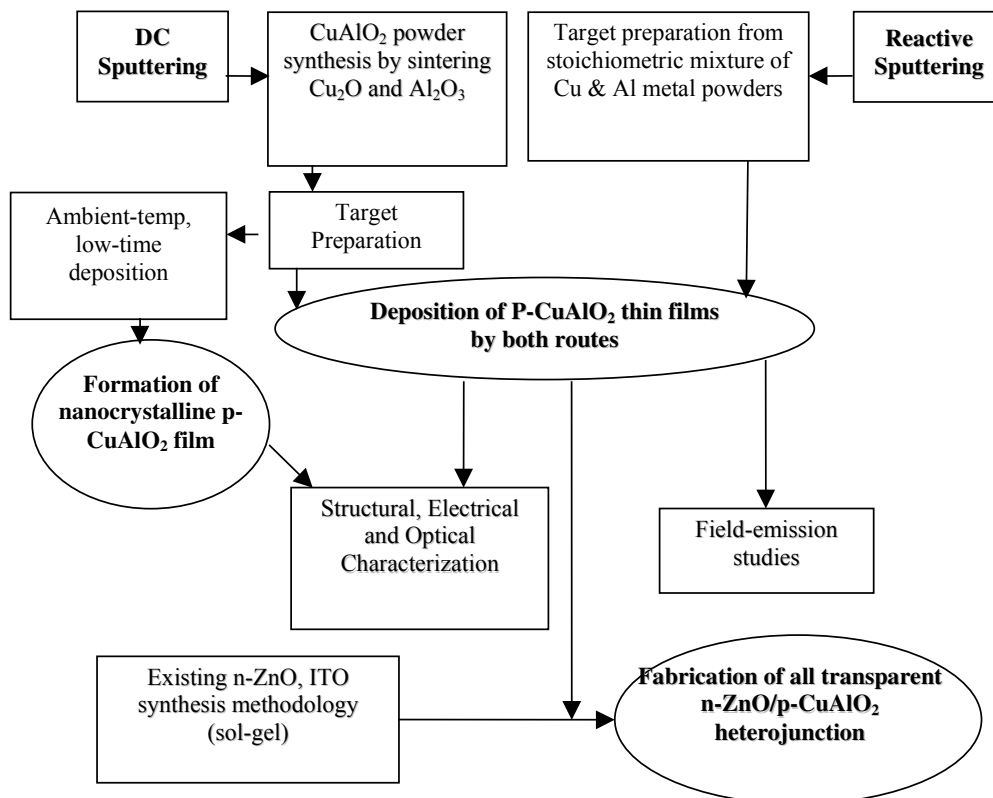


Figure 6(a). Layout of Deposition and characterization process.

deposition. Prior to the deposition, the chamber was evacuated by standard rotary and diffusion pumping arrangements to a base pressure of 10^{-6} mbar. Subsequently, the chamber was flushed with Ar several times and then the target was pre-sputtered at 0.05 mbar in Ar atmosphere for 10 minutes to remove contaminations, if any, present on the target surface. The summary of the deposition conditions is shown in Table 7. After every 2 hours of deposition, the films were post annealed in the same vacuum chamber at 493 K for 1 hour (at pressure 0.2 mbar) maintaining the oxygen flow to induce excess oxygen into the film to increase p-type semiconductivity of the film. A simple flow-chart describing the steps followed for the preparation and characterization of CuAlO_2 thin film by D.C. and reactive sputtering is shown in Fig. 6(a).

Table 7. Summary of deposition parameters by reactive D. C. sputtering [161]

Electrode distance	:	1.8 cm
Sputtering Voltage	:	1.0 kV
Current density	:	12 mA / cm^2
Substrates	:	Si (400), glass
Base pressure	:	10^{-6} mbar
Sputtering gasses	:	Ar & O_2 (3 : 2 volume ratio)
Deposition pressure	:	0.2 mbar
Substrate temperature	:	475 K
Deposition Time	:	4 hr
Post-annealing time	:	60 min
Post-annealing temperature	:	493 K
Post-annealing atmosphere	:	O_2 (0.2 mbar)

4.3. Synthesis of CuAlO_2 Film by Wet-Chemical Dip-Coating Technique

The wet-chemical synthesis procedure also involved three steps:

(i) Sol preparation

The sol required for deposition of the films was prepared as described in the following steps. Firstly, 2.5 cc of concentrated HCl was added slowly to 0.015 moles of cuprous chloride (CuCl , 99.99%) and the solution was stirred continuously by a magnetic stirrer. During the stirring process, further addition of 4 - 5 drops (0.2 cc) of HCl to the solution was done until all the salts were dissolved into it. On the other hand, another solution was prepared by adding 30 cc of distilled water drop by drop to 0.015 moles of aluminium chloride (AlCl_3 , 99.9%) to dissolve it completely. Two solutions were then mixed and 50 cc of distilled water was also added to it. The mixed solution was then stirred continuously at an elevated temperature of 85°C for 2 hrs. During the stirring process, 0.002 moles (approx.) of NaOH pellets (99.99%) were added to the solution to control the pH value around 2. In the resulting solution, the concentrations of Cu and Al were calculated to be 0.187 moles / liter each. The solution was then aged for 3 hrs to get the required sol which was used for dip coating process.

(ii) Substrate cleaning

The substrates used, were glass and Si (400). The substrate cleaning procedure was same as that one described in Section 4.1.

(iii) Dip-coating

Substrates were first dipped into and then withdrawn vertically from the solution slowly at the rate of 6 cm / min for 12 to 15 times. Between two successive dipping, the substrate along with the sol was dried at $\sim 100^\circ\text{C}$ - 120°C to have quick gelation. After the dipping, withdrawing and drying procedure, the resulting films were annealed at $\sim 480^\circ\text{C}$ to 500°C in air for 3 hrs to form the desired copper aluminium oxide thin film. A flow chart of the dip-coating procedure is shown in Fig. 6(b).

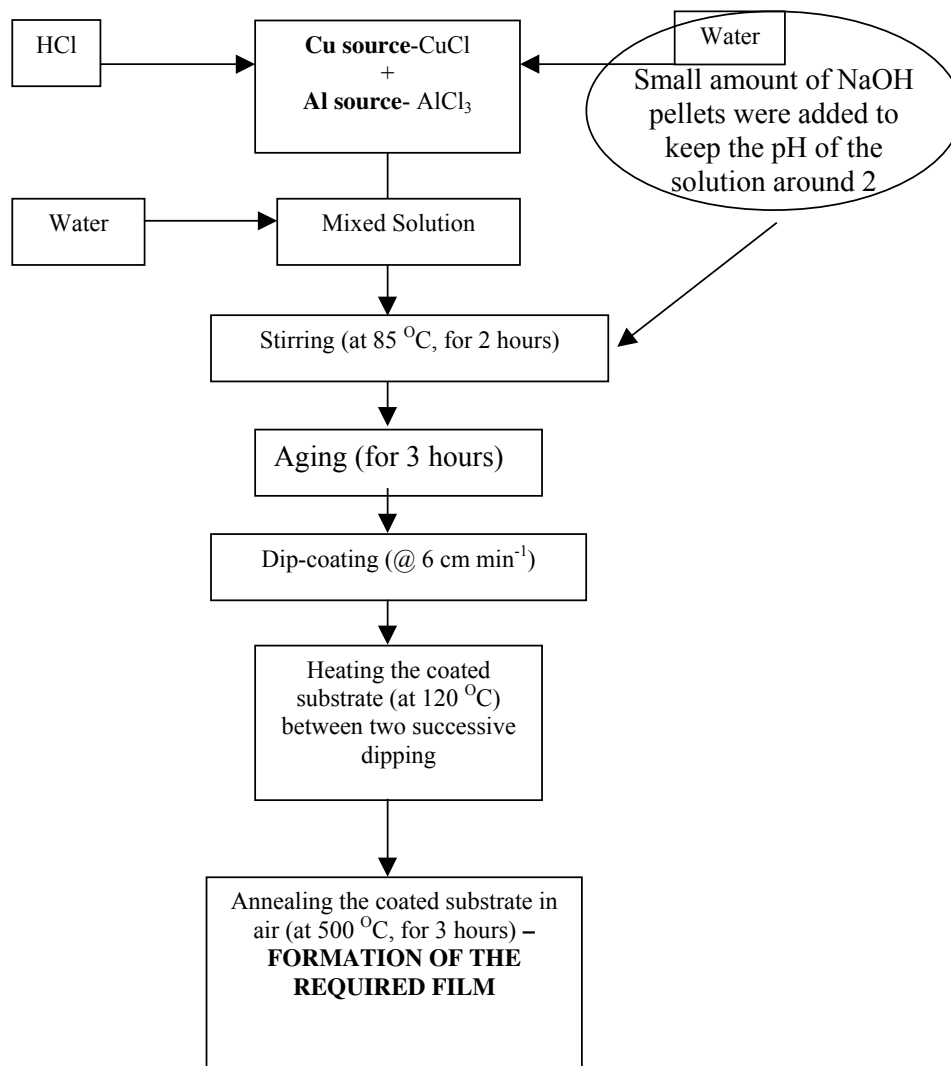


Figure 6(b). Flow Chart of wet-chemical dip-coating process for CuAlO_2 thin films.

4.4. Characterizations of the Films

Structural properties of the films were investigated by X-Ray Diffraction (XRD) measurements. The films were deposited on Si (400) and glass substrates. A Bruker X-ray diffractometer (D8, AXS, ADVANCE) was used for recording the diffraction traces of the films in $\theta - 2\theta$ mode. Germanium (022) monochromator was used for $\text{CuK}\alpha$ (1.4506 Å) radiation from a highly stabilized Bruker X-ray generator (K 780). Diffraction traces were recorded at room temperature. Another X-ray diffractometer (Philips PW 1730 / PW 1710, by $\text{CuK}\alpha$ line) was also used for structural studies of some of the samples.

Surface morphology and microstructural properties of the films were studied by Scanning Electron Microscopy (SEM) and Transmission Electron Microscopy (TEM) respectively. An SEM (JEOL, JSM 5200) was used to determine the growth and morphology of the samples. The resolution of the instrument was 5.5 nm. It is designed to operate at voltages between 1 to 25 kV (7 steps). The magnification could be varied 15 X to 200,000 X (25 steps). Probe-current range was 10^{-12} to 10^{-9} A. The instrument can be operated in two types of image modes e.g. Secondary Electron Image (SEI) and Backscattered Electron Image (BEI). The camera was 35 mm, single-lens reflex type (MP 35051, CSI 3) with focal length = 50 mm.

A TEM (HITACHI H 600) was used to study the microstructure of the film. The instrument has a guaranteed resolution of 2.04 Å. But the resolution attained during routine measurement was 8–10 Å. Magnification could be varied from 100 X to 30,000 X with accelerating voltage 25, 50, 75 or 100 kV. Selected area electron diffraction pattern (SAED) could be obtained with diffraction camera length 0.2 to 1.6 m.

For SEM studies, films were deposited on both glass and Si substrates whereas for TEM studies, films were deposited directly on carbon coated Cu-grids. The film thickness in this case were maintained between 50 – 100 nm by reducing the deposition time.

Compositions of the films were determined from an Energy Dispersive X-Ray (EDAX, Leica S-440 Oxford ISIS) instrument. The instrument has the capability to detect elements from Boron (5) to Uranium (92).

The optical transmittance (T) and reflectance (R) spectra of the films were measured by UV-Vis-NIR spectrophotometer and different bonding information were obtained from Fourier Transformed Infra-Red spectroscopy (FT-IR). A Shimadzu-UV-3101-PC spectrophotometer was used to determine the optical properties. It is a double beam spectrophotometer with integrating sphere attachment for reflectance measurement within the wavelength range of 190 nm to 2600 nm. The attachment is mainly used for measurement of both transmittance as well as diffuse/specular reflectance of the films. The integrating sphere equipped with photomultiplier (UV-Vis region) and PbS cell (NIR region) detectors. Both the optical transmission and reflection spectra of the films deposited on glass substrates were recorded taking similar glass as reference, and hence the spectrum gives transmittance and reflectance of the films only. Another Hitachi (U 3410) spectrophotometer was used to measure transmittance spectra of some samples. The wavelength for this instrument could be varied from 180 to 3500 nm.

A Nicolet Magna (IR-750 Series-II) FT-IR was used to obtain different bonding information in the sample. The resolution of the instrument was 4 cm^{-1} with the wavenumber range of 4000 cm^{-1} to 400 cm^{-1} . Number of scan steps was 50.

The sheet resistance and temperature dependence of electrical conductivity of the films were studied by linear four-probe method using Kiethley electrometer (Model- 6514) from

300 to 550 K. All The contacts were made with silver paint, which showed linear I-V characteristic over a wide range of applied voltage. Films were deposited on glass substrates.

Thermoelectric power (TEP) and Hall effect studies were used to determine the type of conduction taking place within the deposited films. For thermoelectric power measurement (temperature variation of Seebeck coefficient), a temperature gradient across the sample was created by keeping one end of the film in a hot-head and the other in a cold-head. The hot-head temperature was varied from room temperature to 460 K, whereas the cold-head was kept at room temperature. And these temperatures of the hot and cold-ends of the film were measured by proper thermocouple arrangements. The thermoemfs generated between the hot and cold ends of the sample, at different hot-end temperatures, were used to determine the Seebeck coefficients (S) of the material. The entire system was kept under vacuum condition.

For room temperature Hall-study, we have used van der Pauw method, with rectangular van der Pauw configuration. The electrical connections were made at the four corners of the sample. For the measurement of Hall-voltage and related parameters, an electromagnet (Polytronic Corporation, India) with 4 inches pole pieces was used alongwith a stabilized power supply (Current range – 0 to 6 A, Voltage range – 0 to 100 V) to monitor the field strength. The distance between the pole pieces could be varied and for a separation of 3.0 cm of pole pieces, the field strength could be adjusted to a maximum of 10 K Gauss. The field within the measuring system was determined by using Differential Gaussmeter. Flow-diagram of various characterizations done on the CuAlO_2 films are furnished in Fig. 6(c), 6(d) and 6(e).

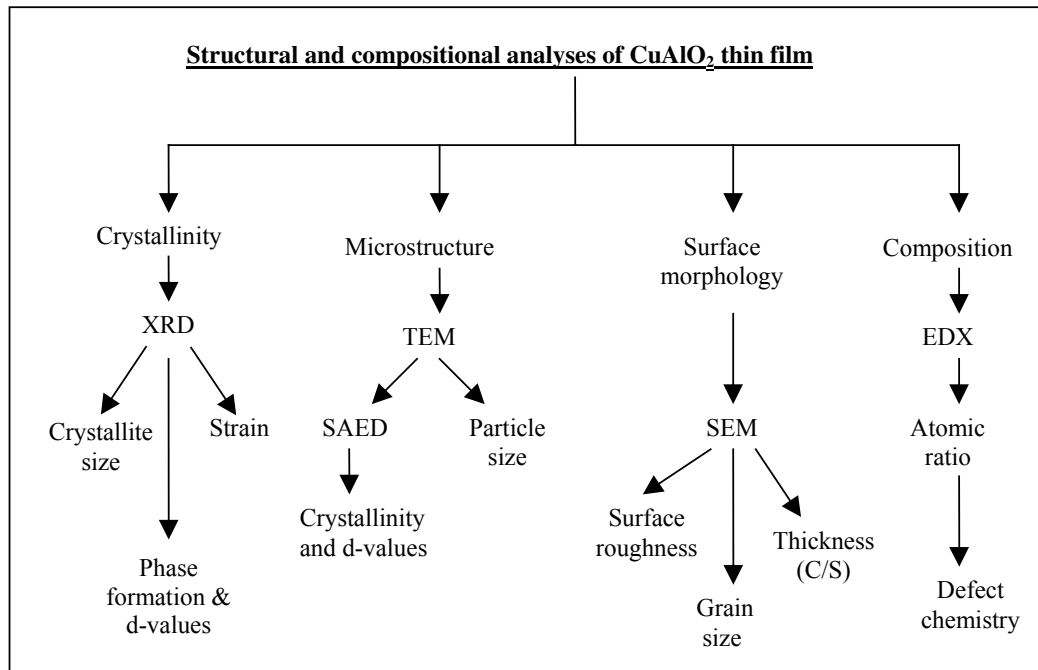
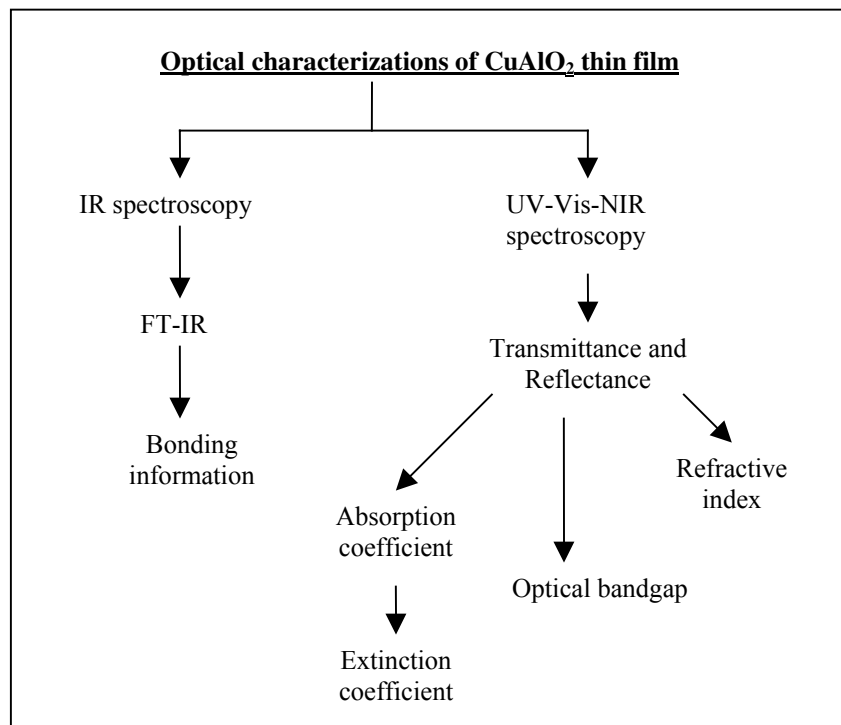
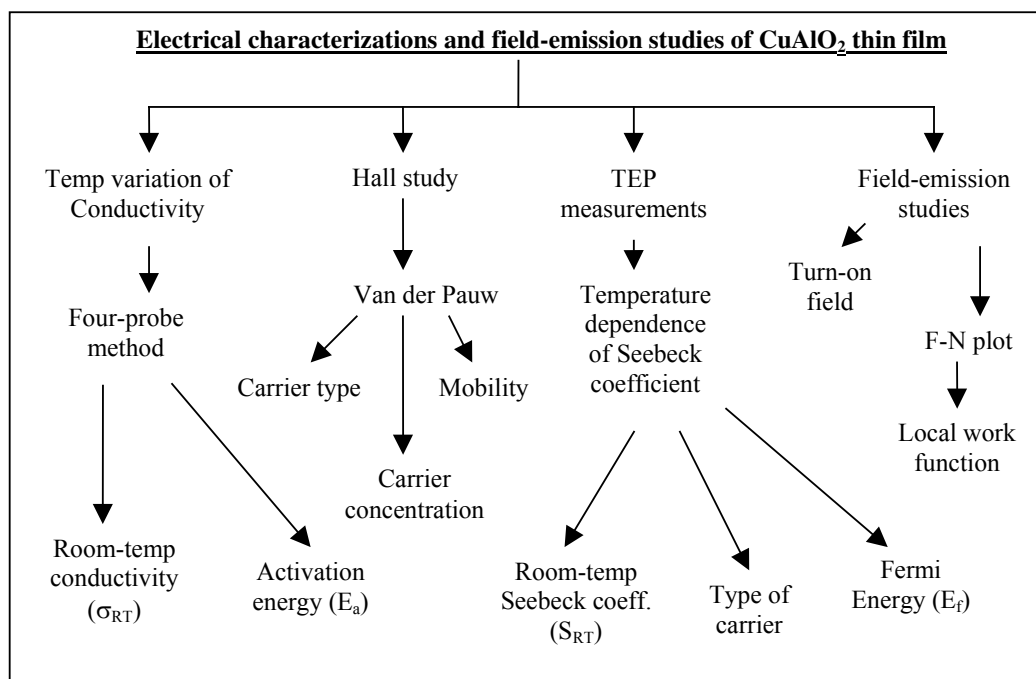


Figure 6(c). Flow-chart of structural characterizations and compositional analyses of CuAlO_2 thin film.

Figure 6(d). Flow-chart of optical characterizations CuAlO_2 thin film.Figure 6(e). Flow-chart for the Electrical and FE characterizations of CuAlO_2 thin film.

5. Results and Discussion

5.1. Properties of D. C. Sputtered Films

i) X-ray diffraction studies

X-ray diffraction study in thin film technology is essential to identify proper phase formation of the required polycrystalline films as well as the degree of crystallinity of the materials. In this section we present the results of the XRD analyses of sintered CuAlO_2 target as well as thin films prepared both by D. C. and reactive D. C. sputtering methods. Also the semiquantitative information of strain and particle size of the films are obtained from the XRD data.

Fig. 7 shows the X-ray diffraction pattern (XRD) of the synthesized CuAlO_2 powder, which was used for target preparation. 2θ values for the scanned pattern range from 10 degree to 100 degree. The peaks of the powdered material are identified to originate from (006), (101), (012), (104), (107), (018), (110), (00 $\bar{1}2$), (116), (202) and (119) reflections. This pattern closely reflects the rhombohedral crystal structure with $R\bar{3}m$ space group [113]. From the XRD pattern it is observed that the target material contains no unreacted species, such as Cu_2O or Al_2O_3 or any other phase of copper aluminium oxide (e.g. $\text{Cu}_2\text{Al}_2\text{O}_4$). The crystallographic data and bond lengths of CuAlO_2 are furnished in Table 1.

The sintered powder was then pressed into a pellet and used for the target of D. C. sputtering. The films were deposited on both glass and Si (400) substrates. After deposition, the films were post annealed in oxygen atmosphere (0.2 mbar). Post – deposition annealing times (t_a) were varied from 30 min to 150 min to observe any variation in structural, morphological, optical and electrical properties of the films.

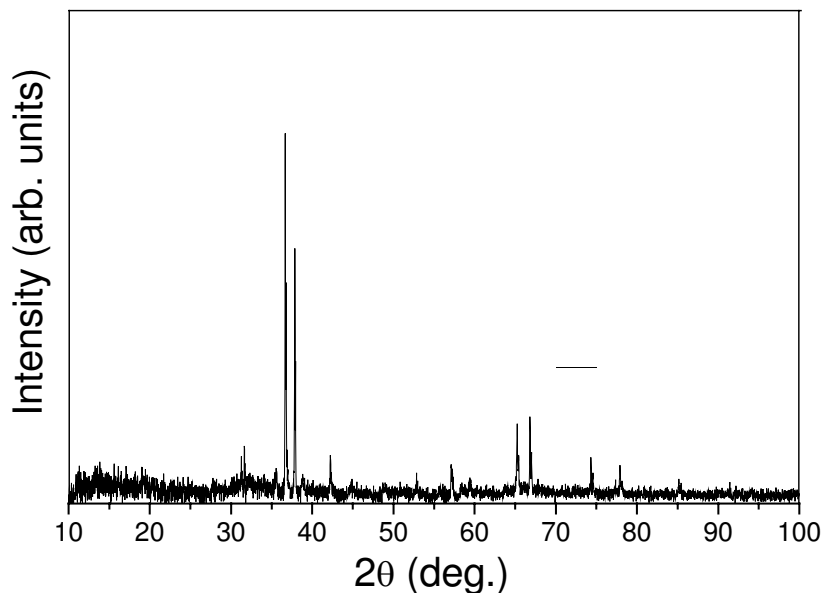


Figure 7. X-ray diffraction pattern of the synthesized CuAlO_2 powder.

Fig. 8(a) shows the XRD pattern of the D. C. sputter-deposited CuAlO_2 thin film on Si (400) substrate for post-deposition oxygen annealing time (t_a) 60 min. The XRD pattern shows a strong (006) orientation. Two other small peaks e.g. (003) and (018) have also been observed in the pattern. It is worthwhile to mention that, for XRD patterns of CuAlO_2 powdered samples, Kawazoe et al [64] and Yanagi et al. [67] previously reported a high (012) orientation, whereas for the thin films deposited on sapphire substrates by PLD method, they observed a strong (006) orientation. For the XRD pattern of our CuAlO_2 powder, we observed a maximum intensity at (101) peak as shown in Fig. 7, whereas the CuAlO_2 thin films deposited by D. C. sputtering on Si substrate, a strong (006) orientation was observed as reported previously [64, 67]. It is also noteworthy that the CuAlO_2 thin films deposited previously by other techniques, such as R. F. sputtering [147], CVD [149-151], wet-chemical method [153] etc., either the crystal quality of the films were not very good or the films were phase impure (i.e. the films contained some amounts of impurity such as CuO , Cu_2O , $\text{Cu}_2\text{Al}_2\text{O}_4$ etc.). This would result in the poor electrical characteristics of those films. But as evidenced from the XRD pattern of our D. C. sputter-deposited CuAlO_2 thin films, these films are highly crystalline, and there are no unreacted species and any impurity present in the films.

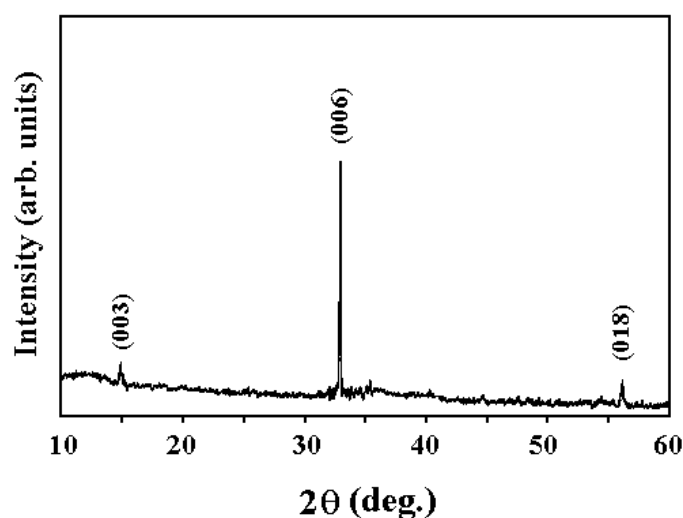


Figure 8(a). XRD pattern of CuAlO_2 thin film deposited on Si substrate, with post-annealing time (t_a) 60 min.

For the films deposited at other annealing times (t_a) e.g. 30 min, 90 min, 120 min and 150 min, the XRD patterns show identical peaks and no significant changes have been observed in the intensity of the peaks and, therefore, not shown here. This is probably because, in all cases, the annealing temperature was kept fixed (at 473 K) and the lowest time of annealing (i.e. 30 min) of our films may be sufficient enough to saturate the grain growth at that particular deposition temperature (473 K) and, hence, no further change in the XRD patterns of our films with increase in post-annealing time was observed. This indicates that in our case, post deposition annealing time has no (or almost insignificant) effect on the structural properties of the films. Fig. 8(b) shows the film deposited on glass substrates with 60 min

post-annealing time. The figure shows similar peaks as that deposited on Si substrate [Fig. 8(a)], but the intensities of the peaks were slightly lesser and the peak-sizes were slightly broader than that deposited on Si substrates. Table 8 shows the comparison between the theoretical d-values given in JCPDS file and observed d-values obtained from XRD data of sintered CuAlO_2 powder (Fig. 7), D. C. sputtered CuAlO_2 thin film (Fig. 8).

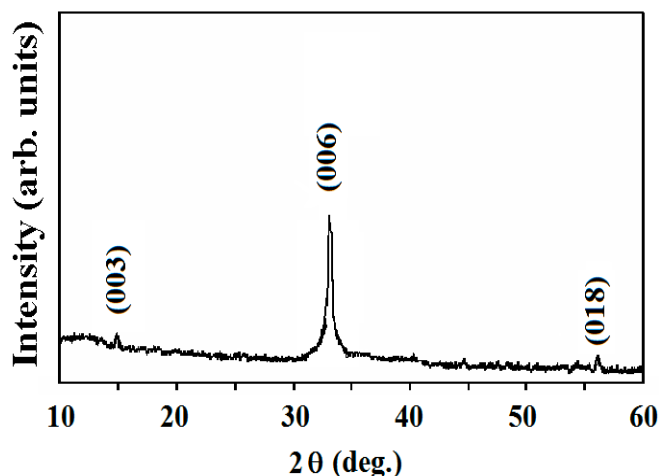


Figure 8(b). XRD pattern of CuAlO_2 thin film deposited on Si substrate, with post-annealing time (t_a) 60 min.

Table 8 Comparison between the theoretical d-values, observed d-values of CuAlO_2 powder, D. C. sputtered and reactive D. C. sputtered CuAlO_2 thin films.

h k l	d-values from JCPDS file card # 35-1401 (d_{JCPDS}) (Å)	Observed d-values for CuAlO_2 powder (d_{powder}) (Å)	Observed d-values for CuAlO_2 thin film deposited by D. C. sputtering on Si substrate ($d_{\text{DC-Sputter}}$) (Å)
0 0 3	5.610	---	5.700
0 0 6	2.820	2.830	2.800
1 0 1	2.440	2.450	---
0 1 2	2.376	2.378	---
1 0 4	2.133	2.133	---
1 0 7	1.732	1.732	---
0 1 8	1.612	1.611	1.620
1 1 0	1.426	1.428	---
0 0 $\bar{1}2$	1.401	1.401	---
1 1 6	1.274	1.275	---
2 0 2	1.225	1.225	---
1 1 9	1.148	1.140	---

The information on particle size of very small crystallites from the measured Full-Widths-at-Half-Maximum (FWHM) of the diffraction peaks can be estimated from the well-known Scherrer formula [230]

$$L = \frac{x \lambda}{\beta_1 \cos \theta} \quad (3)$$

where L is the particle size, β_1 is the particle-broadening of diffraction peaks measured at FWHM of the peak at a certain 2θ value, x is a correction factor ($= 0.9$) and λ is the wavelength of the X-ray used. It is to be mentioned here that when the size of the individual crystallites in a polycrystalline sample is less than 100 nm, the term “particle size” is usually used [230]. Although the grain size of our sample is not clearly determined from SEM micrograph (shown in Ref. [160]), but a rough estimation shows that it may fall within the limit mentioned above and, therefore, we have used the term “particle size” here.

In polycrystalline thin films, due to the interaction between grains of the films as well as that with the substrate, a single grain in the polycrystalline thin film is not free to deform in the same way as an isolated crystal would, if subjected to the same deforming force. As a result of this restraint by its neighbors, a deformed grain in a polycrystalline aggregate usually is in a state of tension or compression. Thus an “internal stress” or “residual stress” is generated within the films. This residual stress produces uniform or non-uniform strain within the film. If the grains are subjected to a uniform tensile strain at right angles to the X-ray reflecting planes, corresponding diffraction peaks shift to the lower angles but do not change otherwise. Similarly for uniform compressive strain, the diffraction peaks shift to the higher angles with no change otherwise. On the other hand, if the strain is non-uniform then the diffraction peak will be broadened, which is called “strain broadening” [230]. The relation between this broadening and the strain can be obtained by differentiating the Bragg’s law as follows [230]:

$$\begin{aligned} 2\Delta d \sin \theta + 2d \cos \theta \Delta \theta &= 0 \\ \Rightarrow \Delta \theta &= -\frac{\Delta d}{d} \tan \theta \\ \Rightarrow \Delta(2\theta) &= -2 \varepsilon \tan \theta; & [\Delta d / d = \varepsilon] \\ \Rightarrow \Delta\beta &= -2 \varepsilon \tan \theta; & [\beta = 2\theta] \end{aligned} \quad (4)$$

where $\Delta\beta$ is the extra broadening of the diffraction peaks over and above the instrumental breadth (therefore also called “instrumental broadening”), ε is the strain generated within the films, θ is the Bragg angle. Now the above equation contains both tensile and compressive strain and must be divided by two to obtain maximum tensile strain alone or maximum compressive strain alone, if these two are assumed equal. Hence the equation for strain broadening for only one type of strain will be

$$\Delta\beta = -\varepsilon \tan \theta \quad (5)$$

Now if both the effect of “particle-size broadening” and “strain-broadening” is taken into consideration, then the total broadening (β) can be expressed as a linear combination of equations 3 and 5 as follows [231]:

$$\beta = \beta_1 + |\Delta\beta| = \frac{\lambda}{L \cos\theta} + \varepsilon \tan\theta$$

$$\Rightarrow \frac{\beta \cos\theta}{\lambda} = \frac{1}{L} + \frac{\varepsilon \sin\theta}{\lambda} \quad (6)$$

where β is the FWHM of the observed peaks, L is the effective particle size, ε is the effective strain. A plot of $\frac{\beta \cos\theta}{\lambda}$ vs. $\frac{\sin\theta}{\lambda}$ will be a straight-line, slope of which will give the estimation of the effective strain, whereas the intercept on $\frac{\beta \cos\theta}{\lambda}$ axis will carry the information of the effective particle size. Fig. 9 represents the plot of $\frac{\beta \cos\theta}{\lambda}$ vs. $\frac{\sin\theta}{\lambda}$, obtained from the XRD pattern of the CuAlO_2 thin film deposited by D. C. sputtering on Si substrate, with $t_a = 60$ min (shown in Fig. 8(a)). Slope of the graph depicts the strain value as 8.52×10^{-3} and the intercept on y-axis gives the particle size as ~ 26 nm.

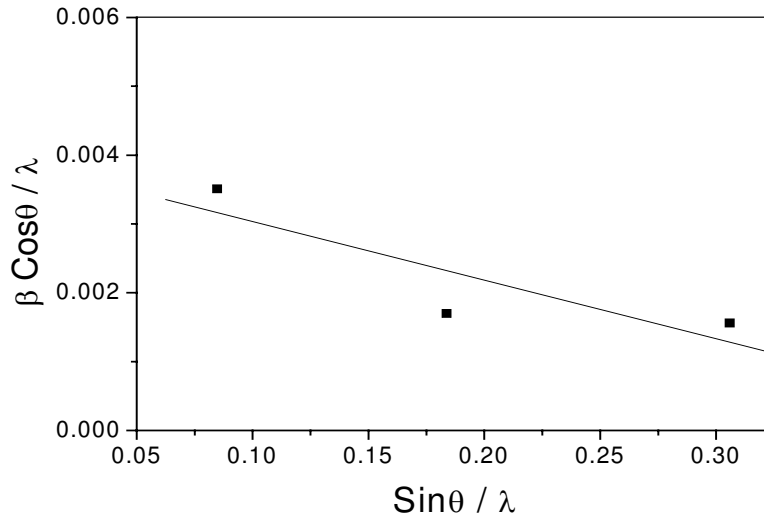


Figure 9. Plot to determine strain & particle size of CuAlO_2 thin film deposited by D. C. sputtering, with $t_a = 60$ min.

(ii) Compositional analyses

Compositional analyses of the D. C. sputtered films deposited with various post-deposition oxygen annealing times (t_a) were done by EDX measurements. Results suggest slight deviation from the stoichiometric composition within the films with increase in post-deposition oxygen-annealing time (t_a). The percentage of excess oxygen within the films ranges from 0.5 at % (for annealing time 30 min) to 10 at % (for the films annealed for 120

min and above) over stoichiometric value. The Cu : Al stoichiometry remained close to 1 : 1 for all the samples (i.e. in the ratio Cu : Al : O = 1 : 1 : 2+x, percentage of x w.r.t. 2 is given here). Previously, Gao and co-authors [154] also observed similar 1:1 atomic ratio of Cu:Al (more precisely 1.06:1.00, and taken as unity within experimental error) in their nanocrystalline CuAlO_2 thin film from EDX analysis. We have observed that for the films post-annealed for 30, 60 and 90 min, the percentages of excess oxygen were around 0.5 at %, 2.5 at % and 5 at % respectively over stoichiometric value. Compositional analyses of the films post-annealed for 120 min and above, show percentage of excess oxygen within the films more than 10 at % over stoichiometric value. Table 9 shows the composition of D. C. sputtered CuAlO_{2+x} thin films for different values of t_a and corresponding chemical formula of the material. These “excess” oxygen atoms are supposed to lie in the lattice positions and (or) interstitial positions and produce enhanced p-type conductivity of the films, which will be discussed in details in later chapters.

Table 9. Composition of D. C. sputtered CuAlO_2 thin films for different values of t_a .

Post-annealing time (t_a) (min)	Cu / Al ratio	Atomic % of excess oxygen	Chemical formula of the film
30	1	0.5	$\text{CuAlO}_{2.01}$
60	1	2.5	$\text{CuAlO}_{2.05}$
90	1	5.0	$\text{CuAlO}_{2.10}$
120	1	10.0	$\text{CuAlO}_{2.20}$
150	1	12.0	$\text{CuAlO}_{2.24}$

(iii) FT-IR studies

Fourier Transform Infra-red spectroscopic (FT-IR) analyses of D.C. sputtered CuAlO_2 thin films were performed. Films were deposited on Si substrates. Wavenumber varied from 400 cm^{-1} to 4000 cm^{-1} . Fig. 10 represents the FT-IR spectra of the CuAlO_2 film deposited by D. C. sputtering technique and post-annealed for 60 min. All bands have been assigned to the absorption peaks of Cu-O, O-Cu-O, Al-O bond vibrations. The broad peak ranging from 500 cm^{-1} to 900 cm^{-1} is actually consisting of a number of peaks, which can be obtained by deconvoluting the peak. The absorption peaks near 550 cm^{-1} and 600 cm^{-1} may be assigned to Cu-O stretching vibration and O-Cu-O antisymmetric vibration respectively. The peak around 600 cm^{-1} originates due to Al-O stretching vibration in AlO_6 octahedra of CuAlO_2 structure. Peaks ranging from 700 cm^{-1} to 900 cm^{-1} may be assigned to short Al-O stretching vibrations in distorted AlO_6 octahedra. Peak around 1000 cm^{-1} may be assigned to Si-O-Al vibration, which occurs due to Si substrate used [232, 233]. Peak at 2349 cm^{-1} is a CO_2 peak and the broad peak around 3000 cm^{-1} - 3500 cm^{-1} is due to O-H stretching vibration, which may be incorporated from the atmospheric contaminations. From the literature survey, it becomes clear that there is no reported study on FT-IR of the CuAlO_2 . So there may remain some unidentified peaks, such as $\sim 1633 \text{ cm}^{-1}$ in our FT-IR spectra. It must be mentioned here that the assignments of the peaks for different vibrational modes of CuAlO_2 is a simplification of the vibrational treatment of different inorganic aluminates as well as copper complexes in organic solvents. A rigorous vibrational treatment of inorganic solids is generally very difficult. Strictly speaking, the different vibrational modes are those of the whole unit cell of

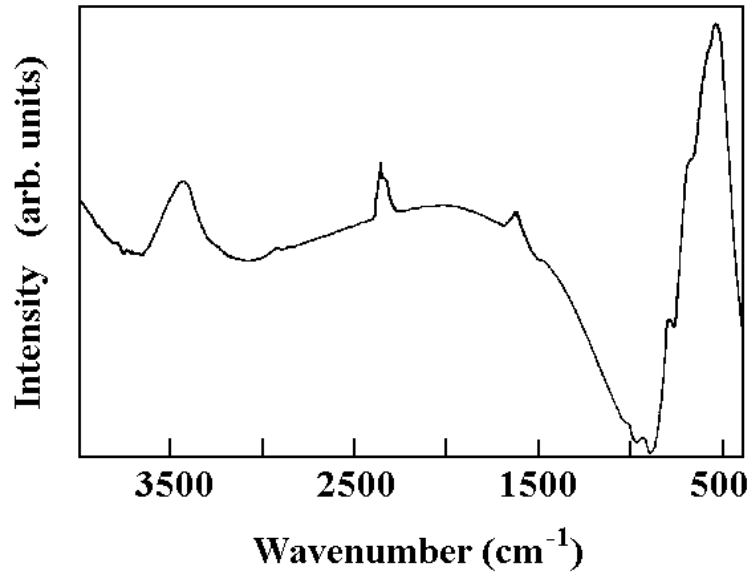


Figure 10 FT-IR spectrum of CuAlO₂ thin film deposited by D.C. sputtering on Si substrate.

the crystal and, therefore, the number of fundamental frequencies are quite high and, hence, detailed assignment of the observed frequencies to the vibrational modes is nearly impossible [233]. In such cases, simplified methods have been applied as follows [233-235]: if a solid A_xB_yO_z is constituted of AO_m and BO_n coordinated groups, two extreme cases must be considered:

- a) If the AO_m and BO_n groups have different vibrational frequencies, then the vibrational interactions between these groups are weak and, therefore, neglected. The groups are assumed to be vibrating ‘independently’ [236].
- b) If the AO_m and BO_n groups have similar vibrational frequencies, then the vibrational interactions between the groups are very large and the vibrations of those groups are taken as a whole [235].

Between these extreme cases, a number of intermediate cases are characterized by weak or moderate interactions [234]. It is quite evident that the assignment of an absorption peak to a vibrational mode of a given coordinated group is meaningful only if the concept of “independent” vibrations is a good approximation for the group under consideration. Now, as CuAlO₂ is a layered-structured material with AlO₆ octahedral layers connected by O-Cu-O dumbbell layers (shown in Fig. 2b), the two layers may be approximated to be vibrating independently. This argument seems reasonable if we theoretically calculate the vibrational frequencies of Cu-O and Al-O bonds. From the equation of simple harmonic oscillator, the frequency of oscillation will be expressed as

$$\nu = \frac{1}{2\pi} \sqrt{\frac{K}{\mu}} \quad (7)$$

where ν is the vibrational frequency, K is the force constant of the bond, μ is the reduced mass. For Cu-O, $\mu_{\text{Cu-O}} = 2.12 \times 10^{-23}$ gm and $K = 2.25 \times 10^5$ dynes cm^{-1} . For Al-O, $\mu_{\text{Al-O}} = 1.67 \times 10^{-23}$ gm and $K = 2.60 \times 10^5$ dynes cm^{-1} [232]. Calculations show that $\bar{\nu}_{\text{Cu-O}} = 546.798 \text{ cm}^{-1}$ and $\bar{\nu}_{\text{Al-O}} = 662.35 \text{ cm}^{-1}$. Although these values will be quite different from the ‘actual’ values when these bond vibrations will be influenced by the neighboring atoms of a three-dimensional network, but, here we are concerned about the difference between the above-mentioned two values. As these values are fairly different, therefore, our argument of independent vibrations of the two coordinated groups in CuAlO_2 is reasonable. And, that is why, we assigned the broad peaks around 400 cm^{-1} to 700 cm^{-1} shown in Fig. 10 to the absorption peaks of Cu-O, O-Cu-O, Al-O bond vibrations.

But, strictly speaking, the concept of ‘independent’ vibration is an approximate one because there is always a more or less important influence of neighboring groups to a certain bond vibration. Also the vibrational frequencies are influenced by any distortion or deformation of the coordinated groups (which is very frequent in thin films). Another additional effect may be present where the coordinated groups are interlinked by common oxygen atoms (as in our case) to form a chain or sheet or three-dimensional network. This affects the vibrational frequencies of a certain bond vibration. As a consequence, the calculated frequencies and the observed values will be quite different. That is why in our cases we have not assigned a vibrational mode to certain frequency, rather to a range of frequencies.

(iv) UV-Vis-NIR measurements

Optical properties of CuAlO_2 thin films are extremely important because of its possible applications in the field of optoelectronics technology. High transparency coupled with high conductivity is the main feature for TCOs as mentioned earlier. Therefore detailed optical characterization and determination of related parameters are the most significant part of the analyses of TCOs. Following this point of view, we have studied the optical properties of CuAlO_2 thin films in details. Three types of films with different post-deposition annealing times ($t_a = 30, 60$ and 90 min) were studied. Fig. 11, 12 & 13 show the transmittance (T) and reflectance (R) spectra of the films with $t_a = 60, 90$ and 30 min respectively. The films were deposited on glass substrates, taking similar glass as reference. Hence the spectra are for the film only. The thicknesses of all the films were 500 nm. Slight noises present around 800 nm to 900 nm in all the graphs are artifacts of detector crossover.

The transmittance (T), reflectance (R) and absorption coefficient (α) of a specimen is related by the equation [237]

$$T = \frac{(1-R)^2 e^{-\alpha d}}{1-R^2 e^{-2\alpha d}} \quad (8)$$

where d is the film thickness and here the multiple internal reflections within the film are considered. Now at the region of fundamental absorption, α will be quite high, so also αd . So we can neglect the 2^{nd} term of the denominator of eqn. (8) and rewrite it as [237, 238]

$$T \approx (1-R)^2 e^{-\alpha d} \quad (9)$$

Knowing T, R and d, absorption coefficients can be determined. If R is not known, then from transmittance data of two samples of known thicknesses d_1 & d_2 , α can be obtained from the relation [237]

$$\frac{T_1}{T_2} \approx e^{\alpha(d_2 - d_1)} \quad (10)$$

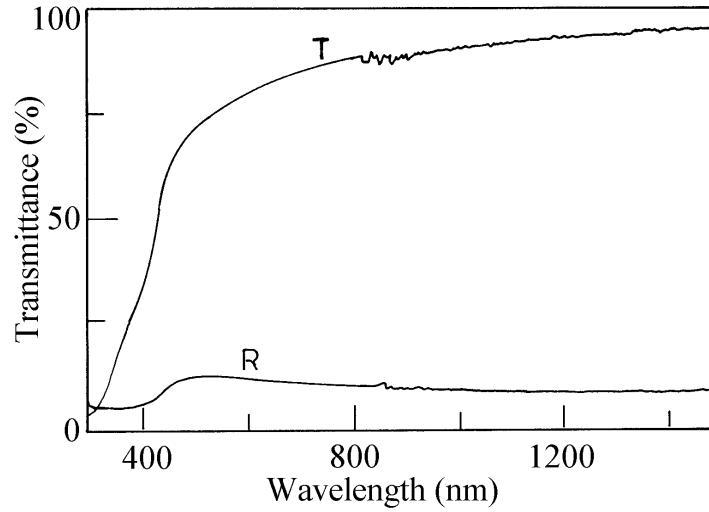


Figure 11. Transmittance (T) and reflectance (R) spectra of CuAlO_2 thin film, post annealed for 60 min. The spectral range is from 300 nm to 1500 nm.

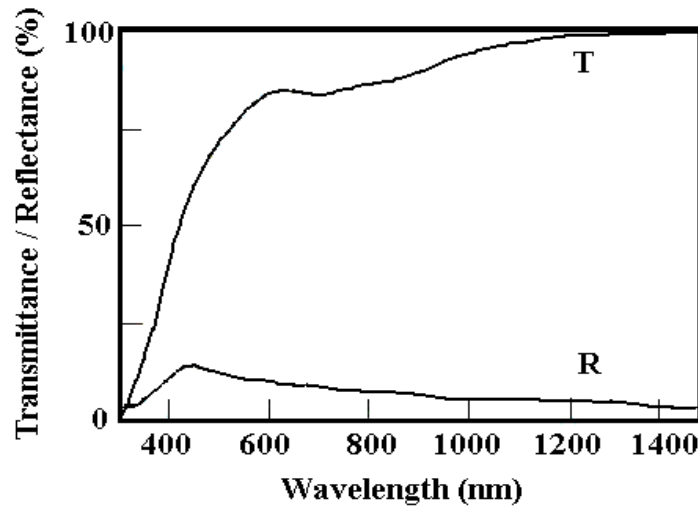


Figure 12. UV-Vis-NIR spectra of D. C. sputtered CuAlO_2 thin film with $t_a = 90$ min.

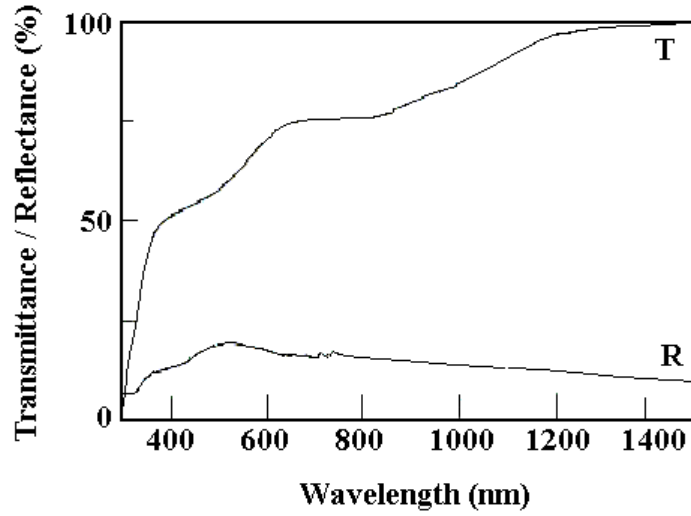


Figure 13. UV-Vis-NIR spectra of D. C. sputtered CuAlO_2 thin film with $t_a = 30$ min.

Beyond the absorption edge if one can observe the interference effect in the transmittance and reflectance spectra due to the multiple internal reflections within the film, then it will be possible to find the refractive index (n) of the material by measuring the wavelengths (λ_1 and λ_2) at two adjacent maxima. The expression will be [237]

$$n = \frac{\lambda_1 \lambda_2}{|\lambda_1 - \lambda_2|} \quad (11)$$

Now, according to the schematic diagram shown in Fig. 14, in the spectral region of fundamental absorption, as a first approximation, T , R and α will be related by the following equation [239] (here, we have neglect the internal multiple reflections for TCOs, unlike Eqs. 8 and 9)

$$T \approx (1 - R)e^{-\alpha d} \quad (12)$$

and

$$R = \frac{(n-1)^2 + k^2}{(n+1)^2 + k^2} \quad (13)$$

where n is the refractive index and k is the extinction coefficient, which is related to the wavelength (λ) and absorption coefficient (α) by the following equation:

$$k = \frac{\lambda \alpha}{4\pi} \quad (14)$$

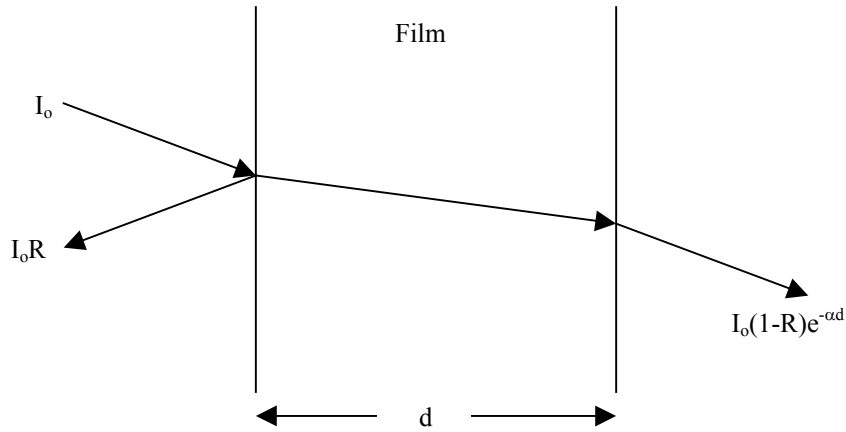


Figure 14. Schematic diagram of incident (I_0), reflected (I_0R) and transmitted [$I_0(1-R)e^{-\alpha d}$] rays in a thin film of thickness d . Multiple internal reflections are neglected.

Now, for transparent medium (as in our p-CuAlO₂ films), $k^2 \ll (n-1)^2$ and Eq. 13 will be reduced to

$$n = \frac{1 + \sqrt{R}}{1 - \sqrt{R}} \quad (15)$$

and the absorption coefficients (α) can be calculated by rewriting Eq. 12 as

$$\alpha = \frac{1}{d} \ln\left[\frac{1-R}{T}\right] \quad (16)$$

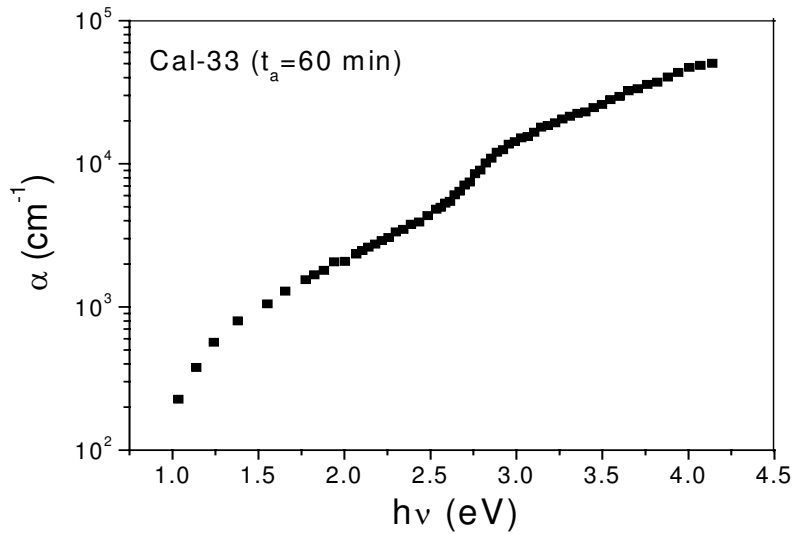


Figure 15(a). Energy dependence of absorption coefficient of CuAlO₂ thin film, post-annealed for 60 min.

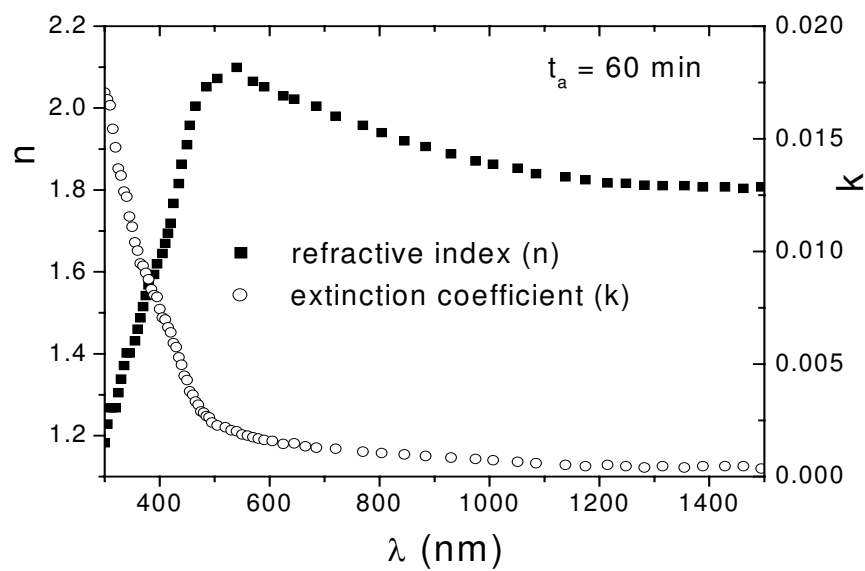


Figure 15(b). Spectral variation of refractive indices (n) and extinction coefficients (k) of CuAlO_2 thin film post-annealed for 60 min.

Fig. 15(a) and **(b)** show the spectral variation of α , k and n of CuAlO_2 thin film post-annealed for 60 min. It has been observed that the refractive index varies between 1.2 to 2.1 in the wavelength range of 300 nm to 1500 nm. Although there are no reported data on the refractive indices of CuAlO_2 thin film, but these data are reasonable when compared with other TCOs such as ITO (1.75 to 2.0 in the wavelength range of 400-1200 nm [240]) and CdO (1.31 to 2.84 in the wavelength range of 500 – 2500 nm [241]).

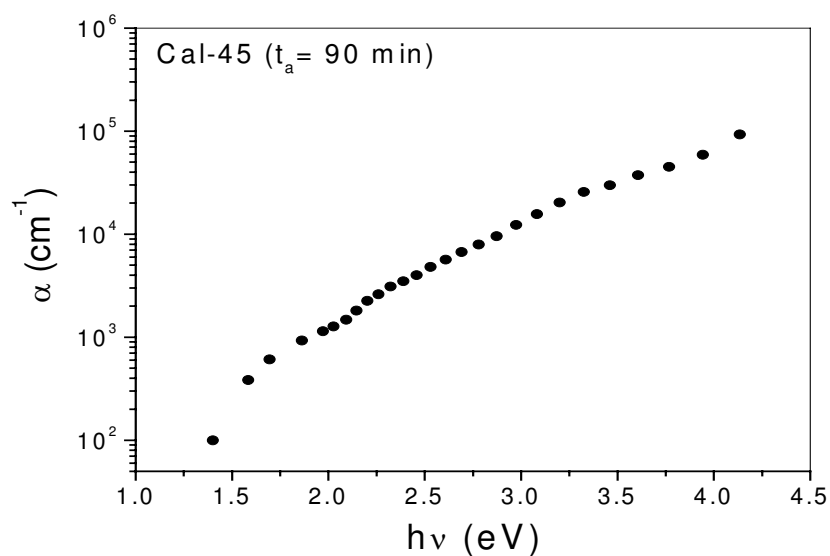


Figure 16(a) Energy dependence of absorption coefficient of CuAlO_2 thin film, post-annealed for 90 min.

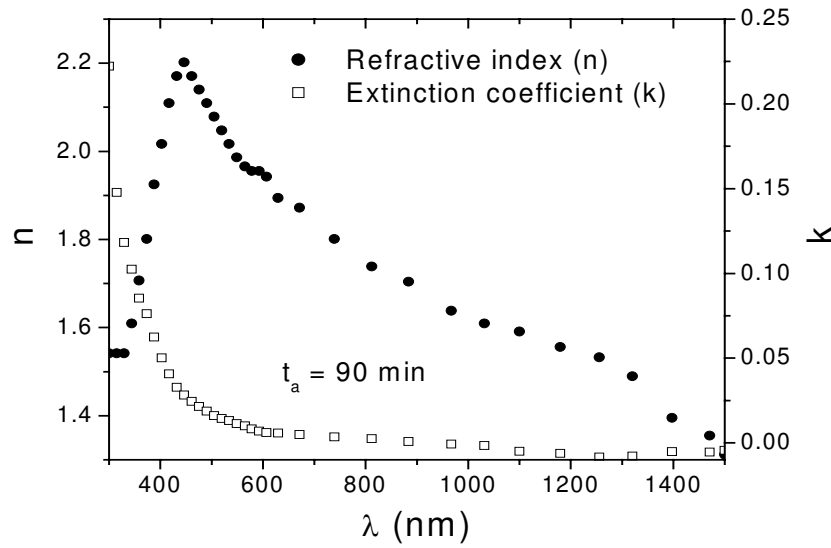


Figure 16(b). Spectral variation of refractive indices (n) and extinction coefficients (k) of CuAlO_2 thin film post-annealed for 90 min.

Fig. 16(a) and (b) show the spectral variation of α , k and n of CuAlO_2 thin film post-annealed for 90 min, whereas **Fig. 17(a) and (b)** show the same for CuAlO_2 film post-annealed for 30 min. In these cases also, we have observed the variation of n between 1.3 and 2.5 within the specified wavelength range. A comparative study of the average visible transmittance, and the ranges of α and n of the three types of films (with different t_a) are furnished in **Table 10**.

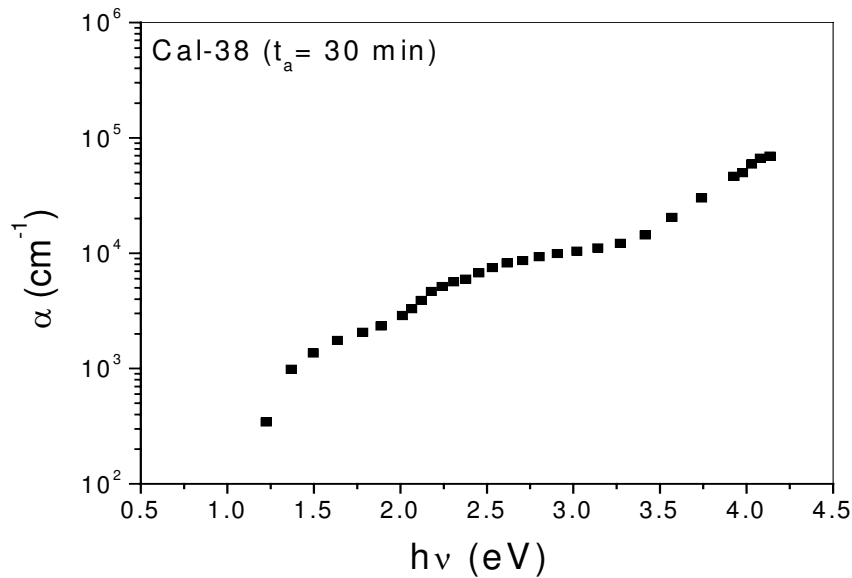


Figure 17(a). Energy dependence of absorption coefficient of CuAlO_2 thin film, post-annealed for 30 min.

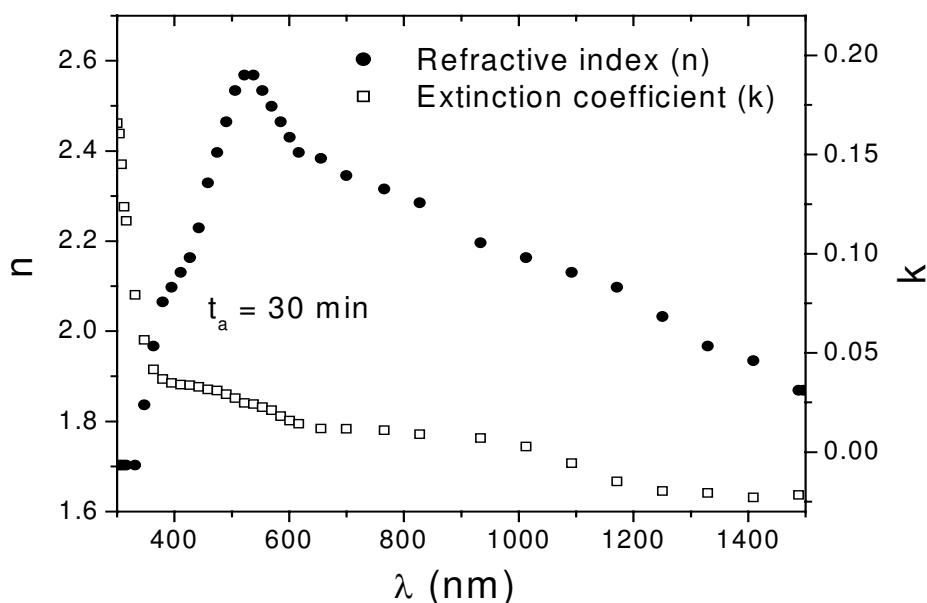


Figure 17(b). Spectral variation of refractive indices (n) and extinction coefficients (k) of CuAlO_2 thin film post-annealed for 30 min.

Table 10. Comparison of different optical parameters of three types of CuAlO_2 thin films with different post-annealing times (t_a).

Film No.	t_a (min)	Average visible transmittance (%)	Range of refractive indices (n)	Range of absorption coefficient (α) (cm^{-1})	Bandgap (E_g)	
					Direct (eV)	Indirect (eV)
CAL-38	30	65	1.7 – 2.6	3.4×10^2 – 7.0×10^4	3.81	2.8
CAL-33	60	80	1.2 – 2.1	2.3×10^2 – 5.9×10^4	3.7	2.1
CAL-45	90	75	1.3 – 2.2	9.9×10^1 – 9.4×10^4	3.8	2.32

In the range of the onset of absorption edge, the absorption coefficients (α) can be described by the relation for parabolic bands, i.e. [237, 238].

$$(\alpha h\nu)^{1/n} = A(h\nu - E_g) \quad (17)$$

where E_g is the band gap of the material, the exponent n depends on the type of transition. For direct allowed transition, $n=1/2$, for indirect allowed transition, $n=2$, and for direct forbidden transition, $n=3/2$. The factor A also depends on the type of transition. For direct allowed

$$\text{transition, } A \approx \frac{e^2 \left(2 \frac{m_h^* m_e^*}{m_h^* + m_e^*}\right)^{3/2}}{n c h^2 m_e^*}; \text{ for direct forbidden transition, } A = \frac{4}{3} \frac{e^2 \left(\frac{m_h^* m_e^*}{m_h^* + m_e^*}\right)^{5/2}}{n c h^2 m_e^* m_h^* h \nu}; \text{ and}$$

$$\text{for indirect allowed transition, } A \propto \frac{(m_h^* m_e^*)^{3/2}}{\pi^4 h^6}; \text{ (n = refractive index of the material,}$$

m_h^* & m_e^* are the effective masses of holes and electrons respectively) [242]. To

determine the possible transitions, $(\alpha h \nu)^{1/n}$ vs. $h \nu$ were plotted for different values of n .

The $(\alpha h \nu)^2$ vs. $h \nu$ and $(\alpha h \nu)^{1/n}$ vs. $h \nu$ plots for three types of films post-annealed for 90 min, 60 min and 30 min are shown in **Fig. 18(a), (b) and (c)** respectively. Extrapolating the linear portion of the graphs to the $h \nu$ axis we have obtained the direct and indirect band gaps as ~ 3.8 eV and 2.32 eV for the sample post-annealed for 90 min respectively, ~ 3.7 eV and 2.1 eV for the sample with $t_a = 60$ min and ~ 3.81 eV and 2.8 eV for the sample post-annealed for 30 min respectively (shown in **Table 10**). These values are comparable to those reported previously by Kawazoe et al (3.5 eV)[64] and Yanagi et al (3.5 eV & 1.8 eV) [67] for their pulsed laser deposited CuAlO_2 thin films and also fall in the range theoretically calculated by Robertson et al (3.91 eV & 2.1 eV) [106]. Also Stauber et al [145] obtained the direct

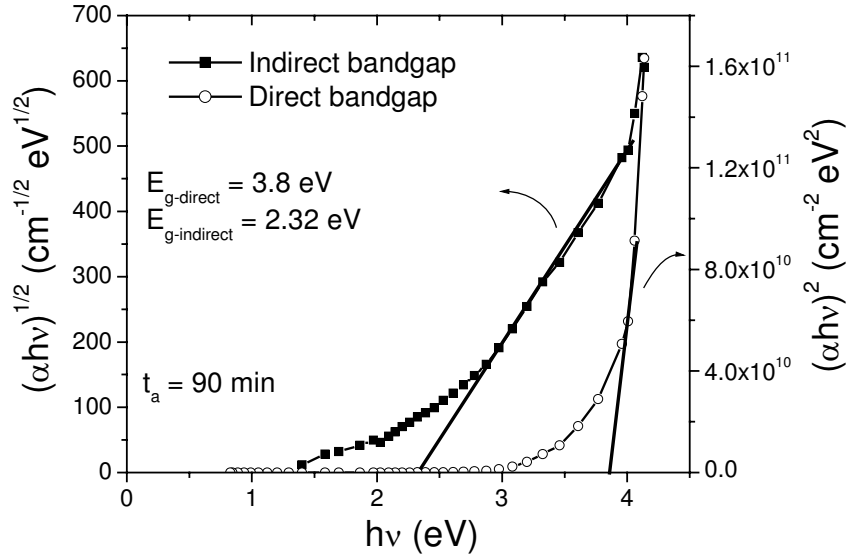


Figure 18(a). Determination of bandgaps of CuAlO_2 thin film post-annealed for 90 min.

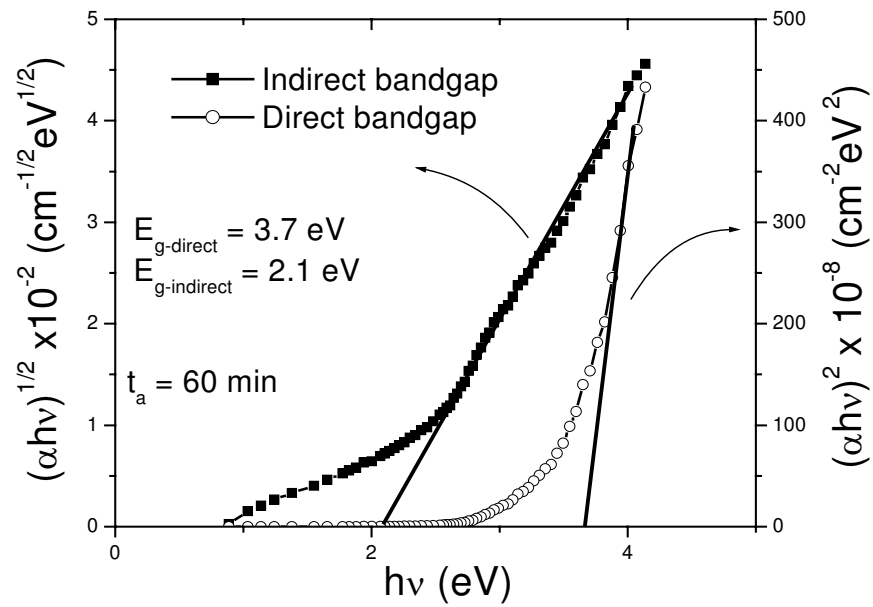


Figure 18(b). Determination of bandgaps of CuAlO_2 thin film post-annealed for 60 min.

bandgap of their R. F. sputter deposited CuAlO_2 thin film around 3.5 eV whereas Wang and Gong [149] reported the direct bandgap of their plasma enhanced chemical vapor deposited (PECVD) copper aluminum oxide films around 3.6 to 3.75 eV.

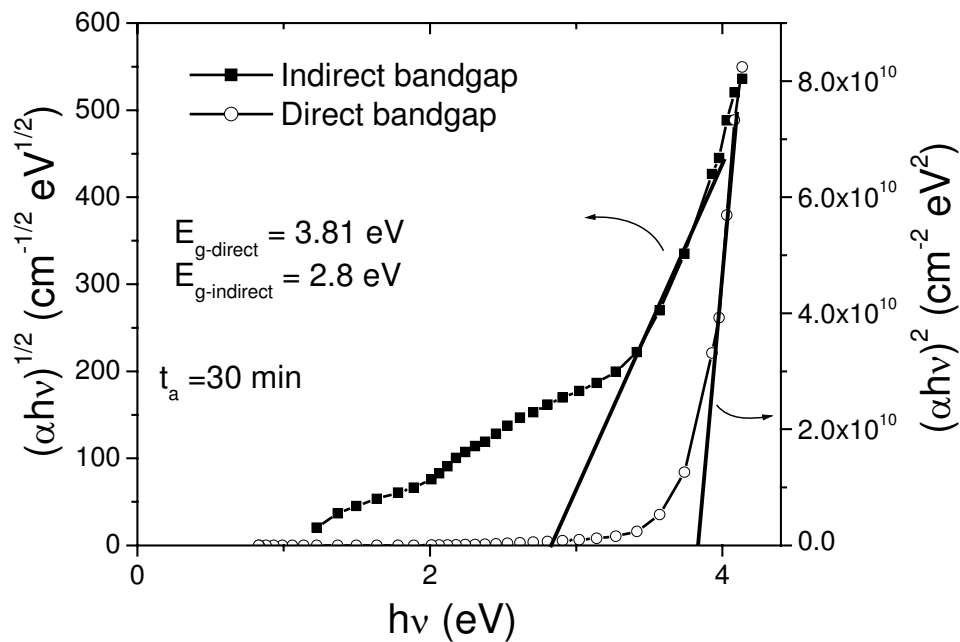


Figure 18(c). Determination of bandgaps of CuAlO_2 thin film post-annealed for 30 min.

(v) **Electrical properties and Hall studies**

Electrical properties of CuAlO₂ thin films have been studied by standard four-probe methods. All electrical contacts were made by silver paint, which showed linear I-V characteristics over a wide range of voltages and temperatures. **Fig. 19** shows I-V characteristics of one contact at room temperature indicating ohmic *nature* of it over the voltage range upto 150 V.

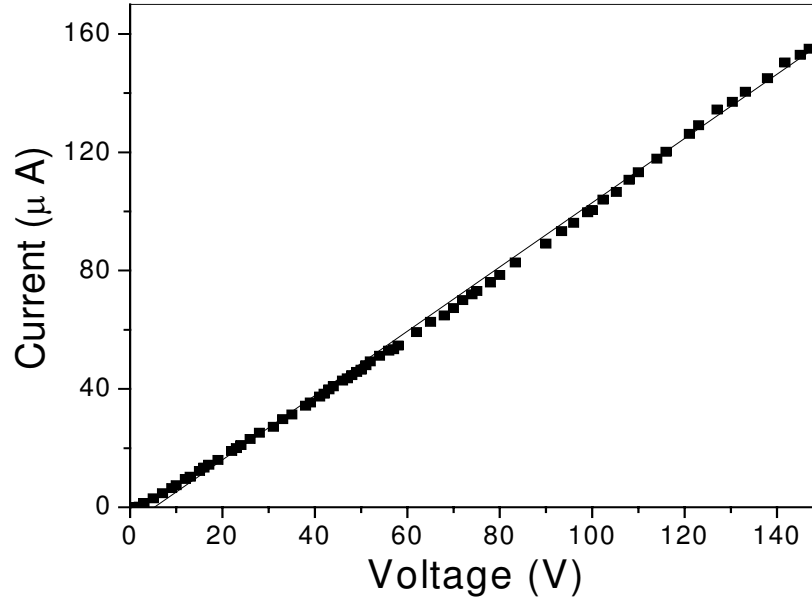


Figure 19. Verification of ohmic *nature* of the contacts.

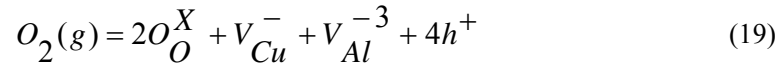
The thermally activated conduction of a semiconductor can be given by the relation [142]

$$\sigma = \sigma_0 \exp\left[-\frac{E_a}{kT}\right] \quad (18)$$

where σ_0 is a temperature independent factor, E_a is the activation energy of the material. For p-type semiconductor (as in our p-CuAlO₂ sample), this is the energy difference between the acceptor level and the top of the valence. Therefore, a plot of $\ln\sigma$ vs. $1/T$ should be a straight-line whose slope would carry the information of the activation energy of the material. We have determined the temperature dependence of conductivity of D. C. sputtered CuAlO₂ thin films for several sets of samples having different post-deposition oxygen-annealing times (t_a) ranging from 30 min to 150 min respectively and observed any variation in the electrical characteristics of these films and then tried to explain it. **Fig. 20** represents the temperature variation (from 300 K to 575 K) of the conductivity (σ) of the films for $t_a = 30, 60, 90, 120$ and 150 min. The thickness of the films was around 500 nm estimated from cross-sectional SEM. An increase in the room temperature conductivity (σ_{RT}) was observed with the increase in annealing times (t_a) upto 90 min. (For example, films with $t_a = 90, 60$ and 30 min, $\sigma_{RT} =$

0.39, 0.16 and 0.09 S cm^{-1} respectively). The conductivities range from a minimum of 0.014 S cm^{-1} (for $t_a = 150 \text{ min}$) to a maximum of 5.0 S cm^{-1} (for $t_a = 90 \text{ min}$) in the above temperature range. Previously, Kawazoe et al. [64] and Yanagi et al. [67] obtained the room-temperature conductivities for their pulsed laser deposited CuAlO_2 thin films on sapphire substrates as 0.095 S cm^{-1} and 0.34 S cm^{-1} respectively. These values are quite comparable to our films post-annealed for 30 min and 90 min respectively.

Defect chemistry plays an important role for the increase in p-type conductivity of this material. Metal deficit (or excess oxygen) within the crystallite sites of the material enhances the p-type conductivity. This deviation from the stoichiometric composition of the components can be induced by regulating the post-deposition annealing time (t_a) in oxygen atmosphere. A detailed discussion on nonstoichiometry and defect chemistry is given in **Section 3**. Now re-writing **Eq. 1** for CuAlO_2 , we get [222, 223]:



where O_O , V_{Cu} , V_{Al} and h denote lattice oxygen, Cu vacancy, Al vacancy and hole respectively. Superscripts X , $-$ and $+$ denote effective neutral, negative and positive charge states respectively.

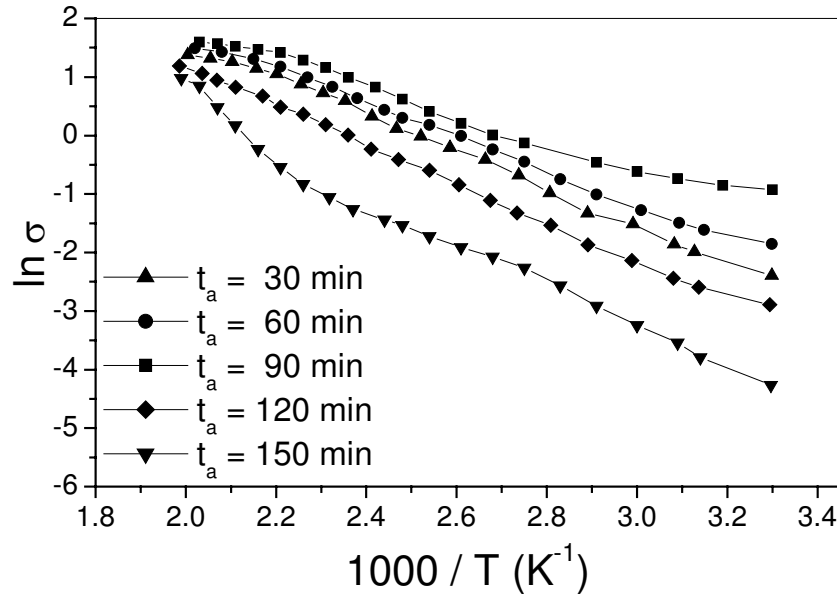


Figure 20. Temperature variation of conductivity of CuAlO_2 thin films for five sets of samples post-annealed for 30 min, 60 min, 90 min, 120 min and 150 min.

Composition analyses of the films [as given in the **Section 5.1(ii)**] showed that for the unannealed films, the composition is almost stoichiometric. But Hot-probe measurement confirmed the p-type *nature* of these films. Therefore, it can be argued that some amount of excess oxygen may be present in the unannealed films but the amount is so low that it could not be measured within our experimental limit. This argument seems reasonable if we

compare our result with the previously reported values where it has been stated that intercalation of oxygen into the CuAlO_2 thin film was not easy [109] and Thomas [65] suggested that the chemical formula of this material would be CuAlO_{2+x} with as low as 0.001 at % of excess oxygen (i.e. $x = 1/50,000$) over stoichiometric value within the film prepared by Kawazoe et al [64]. Later Yanagi et al. [67] performed post-deposition oxygen annealing of the films prepared by the same method as that of Kawazoe and co-authors [64] and observed a significant increase in the carrier conduction within the films. Although they have not reported the composition of the films, but this enhanced p-type conductivity is most probably due to the presence of excess (nonstoichiometric) oxygen within the film, induced due to post-annealing. Similarly, Wang and Gong [149] observed a significant increase in the conductivity of their copper aluminum oxide films after annealing in air. This may be another experimental proof of the suspected p-type conduction caused by excess oxygen. Following this argument we have performed the post-deposition oxygen annealing of our films to induce excess oxygen within the films for getting enhanced p-type conductivity. We have observed that for the films post-annealed for 30, 60 and 90 min, the percentages of excess oxygen were around 0.5 at %, 2.5 at % and 5 at % respectively over stoichiometric value (c.f. **Table 9**). The Cu : Al stoichiometry remained close to 1 : 1 for all the samples. On the other hand, as shown in **Fig. 20**, an increase in the conductivity with t_a has been observed upto 90 min. Although very little, but still, slight increase in the oxygen content within the films leads to an increase in the conductivity of the films, supporting the above reasoning. But we have seen a decrease in the conductivity when the annealing times were 120 min and above (for $t_a = 120$ min, $\sigma_{\text{RT}} = 0.055 \text{ S cm}^{-1}$ and for $t_a = 150$ min, $\sigma_{\text{RT}} = 0.014 \text{ S cm}^{-1}$, as shown in **Fig. 20**). Compositional analyses of the films post-annealed for 120 min and above show percentage of excess oxygen within the films more than 10 at % over stoichiometric value (cf. **Table 9**). This suggests that although the presence of excess oxygen within the films (with $t_a = 120$ min and above) are evidenced but they are not acting favorably to increase the hole conductivity within the films. These excess oxygen atoms, most probably, lay in the grain boundary regions as trap states, which put hindrance in the carrier conduction and, hence, a decrease in the conductivity of these films is observed. On the other hand, for the films post-annealed for 30, 60 and 90 min, show an increase in the conductivity along-with an increase in the excess oxygen content within the films as mentioned earlier. Therefore, in these cases, the excess oxygen atoms may be acting favorably to generate holes within the films. But it must be admitted that the maximum conductivity obtained for our films was not as much as it would have been. So, we suppose that in all cases, whether it is for the films with $t_a = 90$ min or less (when an increase in σ with t_a was observed) or those with $t_a = 120$ min or above (when a decrease in σ with t_a was observed), adsorbed oxygen atoms as ‘trapped states’ in the grain-boundary regions are always present. In the previous section [**Section 5.1(i)**], we have estimated the particle size of our films as 26 nm from XRD data. As the particle size is in nanometer order, a large number of grain-boundaries are present in the films, so also considerable amount of trapped states in these grain-boundary regions are present, which put hindrance in the carrier conduction. But for the films with $t_a = 90$ min or less, greater proportion of excess oxygen may be acting favorably towards the hole generation and, hence, dominate the grain-boundary scattering. This may be the reason for the increase in the conductivity with t_a in this region. On the other hand, for the films with $t_a = 120$ min and above, greater proportion of the excess oxygen atoms may be adsorbed in the grain-boundary

regions, which probably be correlated with the larger time of exposure of these films in the oxygen atmosphere [243]. Hence, grain-boundary scattering, masks the increase in the conductivity and, therefore, we observe a decrease in σ with t_a in this region. But the exact mechanism is still not fully understood.

The activation energies (E_a), which correspond to the minimum energy required to transfer carriers from acceptor level to the valence band (for p-type materials), have been obtained from the slope of the graphs (Fig. 20). The values are 196, 245, 270, 284 and 325 meV for $t_a = 90, 60, 30, 120$ and 150 min respectively. As expected, the sample with highest conductivity has least E_a value and vice-versa. These activation energy values are comparable to the previously obtained values by Kawazoe et al. (200 meV) [64] and Yanagi et al. (220 meV)[67]).

Hall effect measurements were done for three types of samples with $t_a = 30, 60$ and 90 min. All the Hall coefficients were positive, which confirms the p-type *nature* of the samples. The Hall coefficient (R_H) for the sample with $t_a = 90$ min ($\sigma_{RT} = 0.39 \text{ S cm}^{-1}$), has been obtained as $+4.6 \text{ cm}^3 \text{ C}^{-1}$ corresponding to a hole concentration (n_p) of $1.2 \times 10^{18} \text{ cm}^{-3}$. For the sample with $t_a = 60$ min ($\sigma_{RT} = 0.16 \text{ S cm}^{-1}$), these values are $+13.9 \text{ cm}^3 \text{ C}^{-1}$ and $4.5 \times 10^{17} \text{ cm}^{-3}$ respectively. And for the sample with $t_a = 30$ min ($\sigma_{RT} = 0.09 \text{ S cm}^{-1}$), R_H and n_p are $+22.5 \text{ cm}^3 \text{ C}^{-1}$ and $2.8 \times 10^{17} \text{ cm}^{-3}$ respectively. For unannealed films as well as for the films post-annealed for 120 min and above, the Hall measurements could not be performed, but the p-type *nature* of the films was confirmed by Hot-probe method. Maximum carrier concentration obtained by us is one order of magnitude higher than that reported by Kawazoe et al. [64], but still one order less than that of Yanagi et al. [67]. Details of the different electrical parameters of CuAlO_2 thin films are furnished in Table 11 and the variation of these parameters with respect to t_a is shown in Fig. 21 (a) and (b).

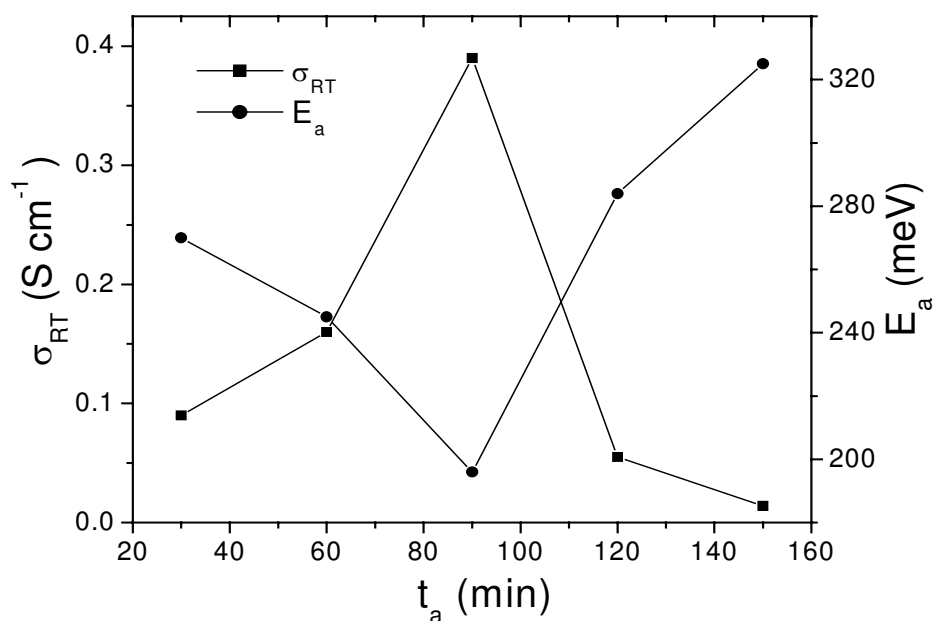


Figure 21(a). Variations of room-temperature conductivity and activation energy of D. C. sputtered CuAlO_2 thin films with post-annealing times.

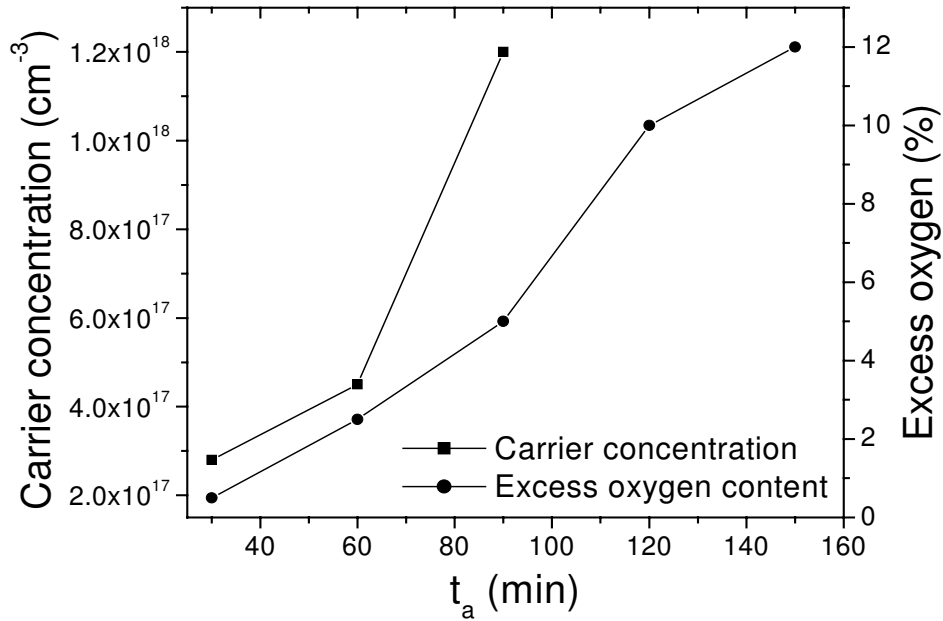


Figure 21(b). Variations of room-temp carrier concentration and excess oxygen content.

Table 11. Different Electrical parameters of CuAlO_2 thin films, deposited at different annealing times.

t_a (min)	σ_{RT} (S cm^{-1})	R_H ($\text{cm}^3 \text{C}^{-1}$)	n_p (cm^{-3})	E_a (meV)	Chemical formula
90	0.39	+4.60	1.2×10^{18}	196	$\text{CuAlO}_{2.10}$
60	0.16	+13.9	4.5×10^{17}	245	$\text{CuAlO}_{2.05}$
30	0.09	+22.5	2.8×10^{17}	270	$\text{CuAlO}_{2.01}$
120	0.055	---	---	284	$\text{CuAlO}_{2.20}$
150	0.014	---	---	325	$\text{CuAlO}_{2.24}$

(vi) Thermoelectric properties

Thermoelectric properties of D. C. sputtered CuAlO_2 thin films have been studied for three types of films having different post-deposition annealing times e.g. 30, 60 and 90 min. The measurements were done from room temperature (300 K) to 550 K. **Fig. 22** shows the temperature dependence of Seebeck coefficients (S) for three types of films. All the Seebeck coefficients are positive in *nature*, which again confirmed p-type *nature* of the films. Room temperature Seebeck coefficients (S_{RT}) of the films were obtained as $+230 \mu\text{V K}^{-1}$ (for $t_a = 90$ min), $+141 \mu\text{V K}^{-1}$ (for $t_a = 60$ min) and $+120 \mu\text{V K}^{-1}$ (for $t_a = 30$ min). As shown in the

figure, the Seebeck coefficients initially decrease from room-temperature to around 390 K and then increase to almost $+400 \mu\text{V K}^{-1}$, for further increase in temperature [244]. Previously, Kawazoe et al. [64] and Yanagi et al. [67] obtained the room temperature Seebeck coefficients for their pulsed laser deposited CuAlO_2 thin film as $+183 \mu\text{V K}^{-1}$ and $+214 \mu\text{V K}^{-1}$ respectively, very much comparable to our values. On the other hand, Koumoto et al. [223] determined the Seebeck coefficient of CuAlO_2 single crystal as well as polycrystal at 600 K around $180 \mu\text{V K}^{-1}$ and $150 \mu\text{V K}^{-1}$ respectively. Also Benko and Koffyberg [97] reported a relatively high value of S_{RT} ($670 \mu\text{V K}^{-1}$) of CuAlO_2 powdered pellets. It has been observed that, in our D. C. sputter-deposited CuAlO_2 thin film, S_{RT} increases with the increase in conductivity of the films. This observation is consistent with the Hicks model [245, 246], where the natural superlattice structure was proposed to show high thermoelectric figure of merit (ZT) due to increase in both S and σ according to the following equation:

$$ZT = \frac{S^2 \sigma T}{\kappa} \quad (20)$$

where ' σ ' is the electrical conductivity, ' κ ' is thermal conductivity and 'S' is the Seebeck coefficient.

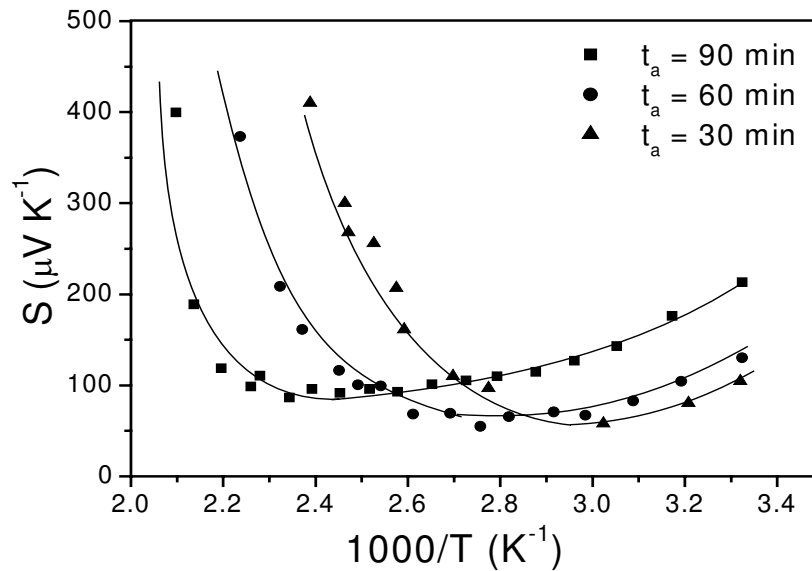


Figure 22. Seebeck coefficient vs. $1000/T$ of CuAlO_2 thin films.

To achieve high ZT, increase in S and (or) σ and decrease in κ are required. But for simple materials, increase in S leads to a decrease in σ . Similarly, an increase in σ is followed by an increase in κ according to Wiedemann-Franz law. So ZT effectively remains more or less constant. To increase Z, various models have been proposed in the last decade. Amongst them, the most exciting proposal by Hick et al. [245, 246] was superlattice quantum-well materials, having an effective two-dimensional density of states for carriers. This density of

state is given by $\frac{m}{\pi \hbar^2 a}$, where 'm' is the carrier mass and 'a' is the quantum-well width.

These authors assumed infinite potential barrier with zero barrier width and showed a considerable increase in Z . Later, Lin-Chung et al. [247] and Broido et al. [248] included the effects of thermal transport in the finite barrier layers and carrier tunneling between layers in the above model to get a modified Z . Encouraged by these findings, various new materials, having layered structure, have been investigated in the last few years, which include NaCo_2O_4 [249], $(\text{ZnO})_5\text{In}_2\text{O}_3$ [250] and CuAlO_2 single crystal [223] etc.

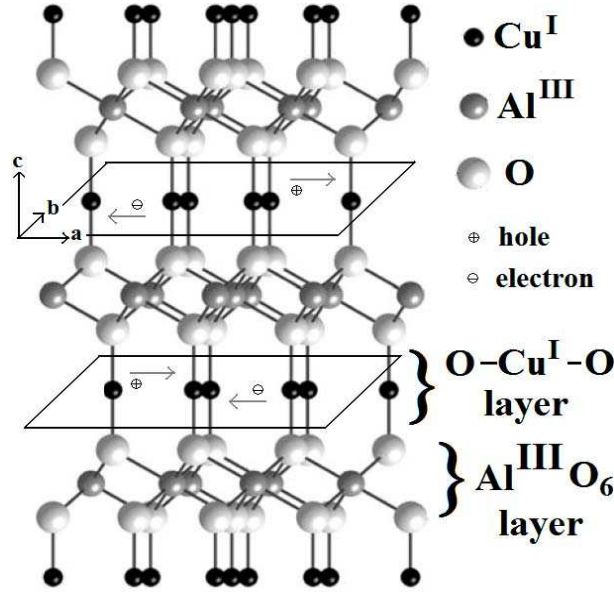


Figure 23. Layered-structure of CuAlO_2 showing the carriers confined in the ab -plane.

Structure of CuAlO_2 delafossite has been shown in **Fig. 23** and described in details in **Section 3**. The crystal structure is an alternative stacking of Cu^{I} and layers of nominal AlO_2 composition consisting of Al-O_6 octahedra sharing edges. Each Cu atom is linearly coordinated with two oxygen atoms to form a O-Cu-O dumbbell unit placed parallel to the c -axis. O-atoms of O-Cu-O dumbbell link all Cu layers with the AlO_2 layers [99]. This structure suggests that CuAlO_2 has a layered structure where carriers can easily move two-dimensionally along ab -plane than to move across the Al-O insulating layers. In the XRD pattern of our CuAlO_2 thin film (shown in **Fig. 8**, section 5.1), we have obtained a strong (006) peak, which is typical of a texture where the c -axis is perpendicular to the substrate (hence parallel to the normal, 'n' to the substrate, i.e. $c \parallel n$). Now, according to our experimental set up (cf. section 4.4), carriers in the films are expected to move along the ab -plane. Hence the above argument of two-dimensional confinement of carriers along the ab -plane is valid for our films. Although, the reason behind the enhanced thermoelectric properties shown by the materials possessing layered structure, is still not fully understood, but Koumoto et al. [223] suggested that this may be correlated with the low dimensionality of the crystal structure and behavior of electrons and phonons in an anisotropic structural environment. Recently, Wang et al. [251] suggested that spin entropy might be responsible

for enhanced thermopower in $\text{Na}_x\text{Co}_2\text{O}_4$ having layered structure [249]. Whether this can be correlated with the good thermoelectric properties of CuAlO_2 , is a question and intense research is needed in this direction.

The variation of thermo-electric power (S) with temperature is given by [252]:

$$S = \frac{k}{e} \left(A + \frac{\Delta E_f}{kT} \right) \quad (20)$$

with

$$A = \frac{5}{2} - s \quad (21)$$

and

$$\tau = \tau_0 e^{-s} \quad (22)$$

where 'k' is the Boltzmann constant, 'e' is the electronic charge, ' ΔE_f ' is the energy difference between Fermi level and the upper edge of the valence band, ' τ ' is the relaxation time for electron scattering, 's' is a constant, which is different for different scattering mechanism and ' τ_0 ' is a constant, which is a function of temperature but independent of the electronic charge, e.

From Eq. 20, we can obtain the Fermi level (E_f), from the slope of the S vs. $1/T$ graph. From the **Fig. 22**, we determined the Fermi energies for three types of samples from the linear portion of the graphs near room temperature, and the values are 130, 151 and 200 meV for $t_a = 90, 60$ and 30 min respectively. Previously, Benko and Koffyberg [97] have determined the Fermi energy of CuAlO_2 powder ($\sigma = 1.69 \times 10^{-3} \text{ S cm}^{-1}$) from the thermopower measurement, as 190 meV, which is comparable to our sample having lowest room temperature conductivity ($\sigma_{RT} = 0.09 \text{ S cm}^{-1}$, $t_a = 30$ min). As previously mentioned, from the slope of the $\ln \sigma$ vs. $1000/T$ plots (**Fig. 20**), we have obtained the activation energy (E_a) values, which give the estimation of acceptor levels. Comparing these values with the values of Fermi levels, we can say that according to the band picture, Fermi level lies between the upper edge of the valence band and the acceptor level, which is typical of a non-degenerate p-type semiconducting material with acceptors not fully ionized. Hence a continuous increase in conductivity with temperature was observed for all three types of samples. Also it has been observed that the sample with maximum conductivity has its Fermi level nearest to the valence band, which is obvious for a p-type material. The values of various thermoelectric parameters of the D. C. sputtered CuAlO_2 thin films are furnished in **Table 12** and a comparison between the activation energy (E_a) and Fermi energy (E_f) is also given in **Table 12**. **Fig. 24** represents the temperature dependence of thermoelectric power factor (σS^2) of CuAlO_2 thin film for the temperature range of 300 K to 500 K. The values range from $1.1 \times 10^{-7} \text{ Wm}^{-1}\text{K}^{-2}$ at a temperature around 300 K (for $t_a = 30$ min) to $7.5 \times 10^{-5} \text{ Wm}^{-1}\text{K}^{-2}$ around 500 K (for $t_a = 90$ min). Koumoto et al. [223] obtained these values roughly as $1.12 \times 10^{-5} \text{ Wm}^{-1}\text{K}^{-2}$ at 550 K for CuAlO_2 single crystal and $7.1 \times 10^{-6} \text{ Wm}^{-1}\text{K}^{-2}$ at 700 K for CuAlO_2 polycrystal. Also Park et al [253] obtained the power factor for CuAlO_2 ceramic as 2×10^{-5}

$\text{Wm}^{-1}\text{K}^{-2}$ at 550 K. These values are comparable to the values reported by us. Also, recently Kurotori and co-authors [254] reported significant increase in the thermoelectric properties of CuAlO_2 , when doped with Zn and Ca. All these reports suggest that this class of material may become very good candidate of thermoelectric converter, and may bring renaissance in the thermopower industry.

Table 12. Different thermoelectric properties of D. C. sputtered CuAlO_2 thin films with different post-deposition oxygen annealing times (t_a).

t_a (min)	S_{RT} ($\mu\text{V K}^{-1}$)	E_a (meV)	E_f (meV)	σS^2 ($\text{W m}^{-1} \text{K}^{-2}$)
90	+230	196	130	2.16×10^{-6}
60	+141	245	151	2.43×10^{-7}
30	+120	270	200	1.10×10^{-7}

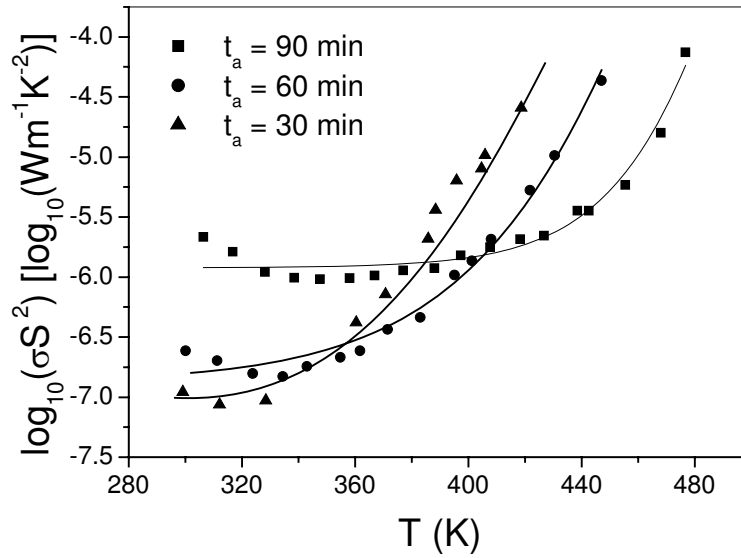


Figure 24. Thermoelectric power factor vs. temperature of CuAlO_2 thin films.

5.2. Properties of Reactive Sputtered Films

i) X-ray diffraction studies

We have also prepared the CuAlO_2 thin films by reactive D. C. sputtering technique. Details of the experimental conditions are furnished in **Section-4.2**. **Fig. 25(a)** shows the XRD spectrum of the reactive D. C. sputtered CuAlO_2 thin film deposited on Si (400) substrate. It shows a strong (006) orientation. Similar orientations was observed by previous workers [64, 67] for their pulsed laser deposited film as well as by ours DC sputter deposited CuAlO_2 thin films [160]. Alongwith the above peak, other peaks were also observed in the XRD spectrum, which could be assigned for (003), (101), (012), (104) and (018) reflections

of crystalline CuAlO_2 . Also no peaks corresponding to starting materials e.g. Cu and Al metal powders as well as their oxides, were found in the pattern. This conclusively inferred that the reactants were completely mixed to give the proper phase of the copper aluminium oxide and no residual metal oxides remained in the film. It is to be noted that previously Ong and Gong [146] deposited copper aluminium oxide thin films by R. F. magnetron reactive co-sputtering of Cu and Al metal targets, whereas Tsuboi and co-authors [147] used D. C. reactive sputtering of facing targets of Cu and Al metals and a rotating substrate. But they obtained

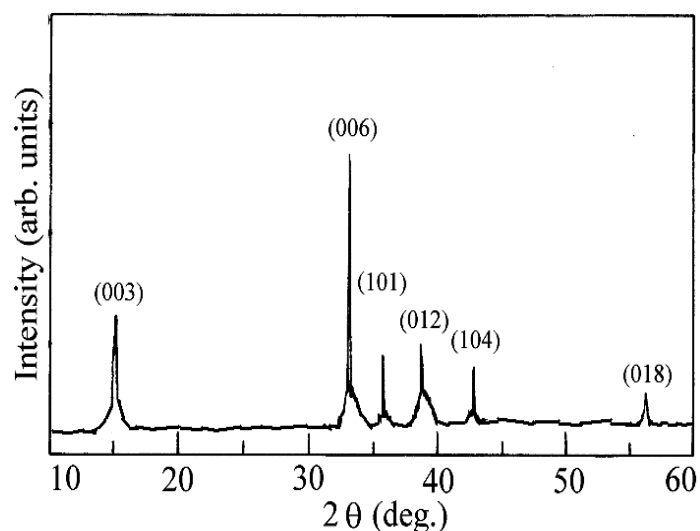


Figure 25(a). XRD pattern of the reactive D. C. sputtered CuAlO_2 thin film.

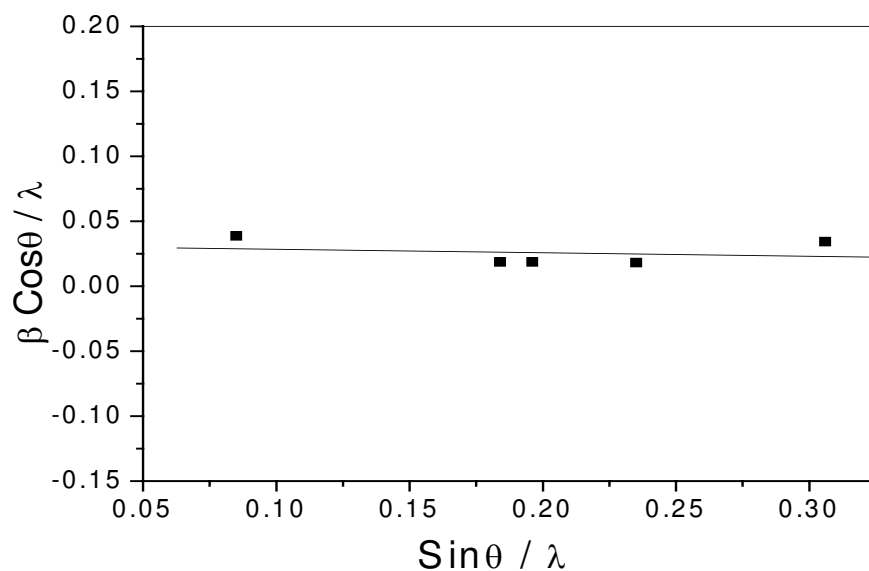


Figure 25(b). Plot to determine strain and particle size of CuAlO_2 thin film deposited by reactive D. C. sputtering.

phase impure films. Also the crystallinity of the films was poor. XRD pattern of our reactive D. C. sputtered film shows better crystallinity, resulting in good electrical properties of the films as described in later chapters. **Fig. 25(b)** gives the plot of $\frac{\beta \cos\theta}{\lambda}$ vs. $\frac{\sin\theta}{\lambda}$. From the slope and intercept, the strain and particle size were determined according to **Eq. 6**. These values were found to be ~ 32 nm and 2.7×10^{-2} respectively.

Table 13 shows the comparison between the theoretical d-values obtained from JCPDS file (d_{JCPDS}) and observed d-values obtained from XRD data of reactive sputtered CuAlO_2 thin film (d_{reactive}) (**Fig. 25-b**) and also compared with D. C. sputtered CuAlO_2 thin film ($d_{\text{DC-Sputter}}$) (**Fig. 8**). **Table 14** compares the effective particle size and effective strain of reactive sputtered and D. C. sputtered (**Fig. 9**) CuAlO_2 thin films. All the data furnished in these two tables for D. C. sputtered films have the post-annealing time 60 min. Since the XRD patterns of the other post-annealed (e.g. 30 min, 90 min) D. C. sputtered films have identical peaks as mentioned earlier, all the related parameters will be identical and, therefore, not furnished here.

Table 13. Comparison between the theoretical d-values, observed d-values of CuAlO_2 powder, D. C. sputtered and reactive D. C. sputtered CuAlO_2 thin films.

h k l	d_{JCPDS} (Å)	d_{reactive} (Å)	$d_{\text{DC-Sputter}}$ (Å)
0 0 3	5.61	5.67	5.70
0 0 6	2.82	2.79	2.80
1 0 1	2.44	2.48	---
0 1 2	2.376	2.374	---
1 0 4	2.133	2.111	---
1 0 7	1.732	---	---
0 1 8	1.612	1.618	1.620

Table 14. Comparison between the effective particle size and effective strain of D. C. sputtered and reactive D. C. sputtered CuAlO_2 thin films.

Deposition technique	Effective particle size (nm)	Effective strain
Reactive sputtered thin film	32	2.70×10^{-2}
D. C. sputtered thin film	26	8.52×10^{-3}

(ii) Compositional analyses

In reactive D. C. sputtering method, films were post-annealed for 60 min and the composition of the film was in the ratio of Cu : Al : O = 1 : 1 : 2.08. Therefore, the chemical formula of the films may be written as $\text{CuAlO}_{2.08}$. This means that the percentage of excess oxygen in the reactive D. C. sputtered films is around 4 at %. It has been observed that the percentage of excess oxygen within the reactive sputtered films, is close to that of D. C. sputtered films with $t_a = 90$ min (cf. **Table 9**). This is probably because of the presence of

excess oxygen atmosphere during the reactive sputtering process and higher substrate temperature.

(iii) FT-IR studies

FT-IR spectrum of reactive sputtered films are shown in **Fig. (26)**. As expected, most of the peaks are similar to that obtained in the films deposited by D. C. sputtering (shown in **Fig. 10**). The broad peak around 400 cm^{-1} to 600 cm^{-1} consists of a number of peaks which have been assigned to the absorption peaks of Cu-O, O-Cu-O, Al-O bond vibrations as mentioned in the **Section 5.1 (iii)**. The broad peak around 800 cm^{-1} to 1100 cm^{-1} is actually consisting of two peaks. Deconvoluting it, the two peaks are obtained around 900 cm^{-1} and 1030 cm^{-1} . First one may be assigned to the short Al-O stretching vibrations in distorted AlO_6 octahedra, whereas second one may be assigned to Si-O-Al vibration, which occurs due to Si substrate used. Small hump around 2500 cm^{-1} is a CO_2 peak and the broad peak around 3100 cm^{-1} - 3500 cm^{-1} is due to O-H stretching vibration, which may be incorporated from the atmospheric contamination. Similar to the **Fig. 10**, here also, we have got an unidentified peak around 1600 cm^{-1} . Also another peak around 2800 cm^{-1} remained unidentified in the spectrum. As there is no detailed literature on the FT-IR studies of this material, this may become an important field of work in the recent future.

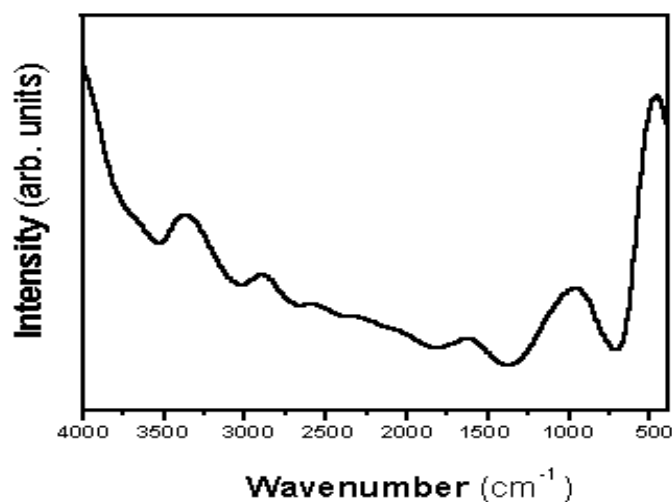


Figure 26. FT-IR spectra of reactive sputtered CuAlO_2 thin films.

(iv) UV-Vis-NIR measurements

The optical properties of the reactive D. C. sputtered thin films have also been studied. The films were deposited on glass substrates and the film thicknesses were measured around 500 nm from cross-sectional SEM. **Fig. 27** shows the UV-Vis-NIR spectra of reactive D. C. sputtered CuAlO_2 thin film in the wavelength range of 300 nm to 1500 nm . These films were post-annealed for 60 min . The average visible transmittance of the film is found to be $\sim 85 - 90\%$. We have critically analyzed the variations of transmittance (T) and reflectance (R) in terms of absorption coefficients (α) to derive information on the optical transitions occurring

in these films. Now in the fundamental absorption region, the value of α is calculated according to the Eq. 16. Also the extinction coefficients (k) and refractive indices (n) are calculated from Eq. 14 and Eq. 15 respectively. The spectral variations of α , n and k are shown in the inset of Fig. 27 and Fig. 28 respectively. For the determination of the bandgaps

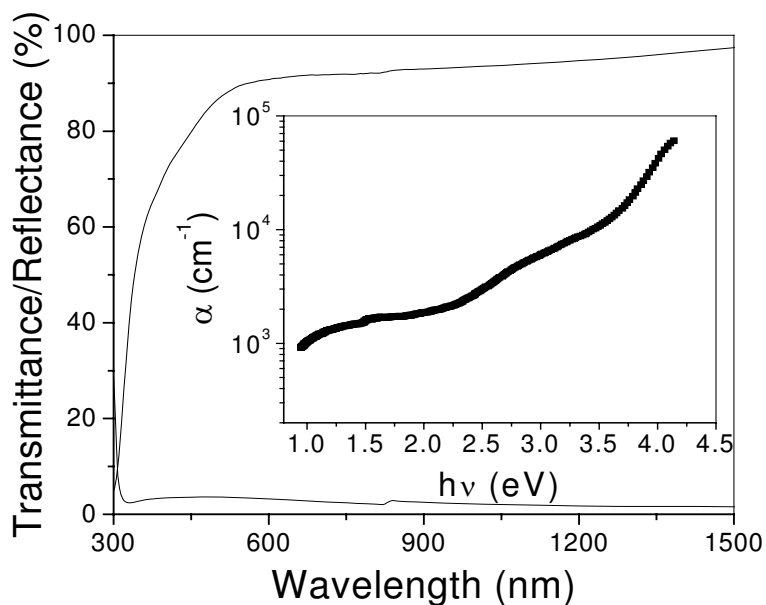


Figure 27. UV-Vis-NIR spectra of reactive D. C. sputtered CuAlO_2 thin film. **Inset:** Energy dependence of absorption coefficients.

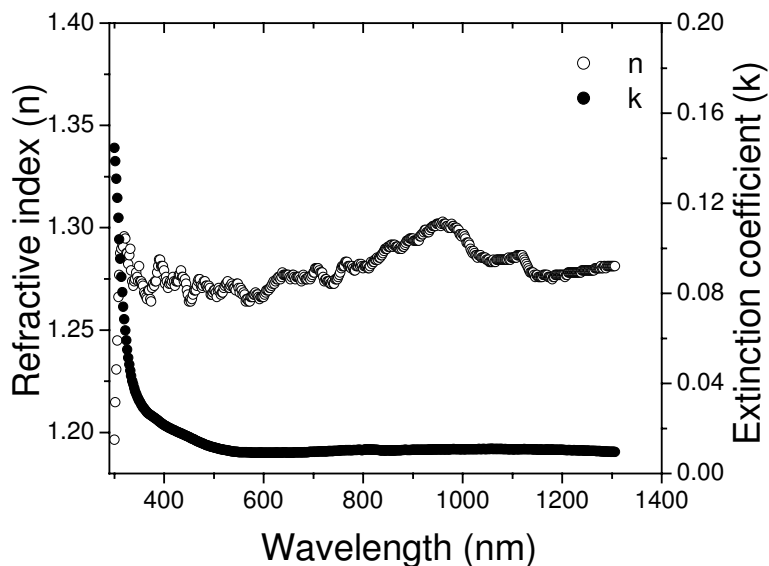


Figure 28. Spectral variation of extinction coefficients and refractive indices of reactive D. C. sputtered CuAlO_2 film.

of reactive sputtered CuAlO_2 thin film, **Eq. 17** has been used. **Fig. 29** shows the evaluation of direct and indirect bandgap values obtained from extrapolating the linear portion of the graphs to the $h\nu$ axis. The direct and indirect bandgap values, we have obtained, as 3.90 eV and 1.89 eV respectively, which are comparable to the previously reported values [64, 67] as well as those of D. C. sputtered films obtained by us (cf. **Table 10**), but slightly greater than the previously reported reactive co-sputtered Cu-Al-O thin films prepared by Ong and Gong (2.9-3.3 eV) [146]. This is mainly because of their phase impure films, which contain some amount of CuO within the copper aluminum oxide samples. A comparison between the direct and indirect bandgap values of reactive sputtered thin films with D. C. sputtered films with different post-annealing times are furnished in **Table 15**.

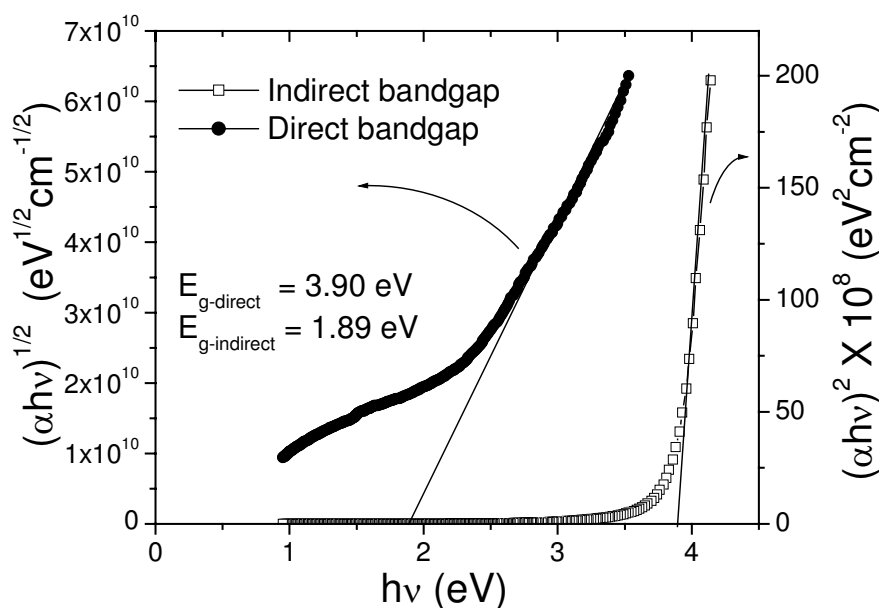


Figure 29. Determination of bandgaps of reactive sputtered CuAlO_2 film.

Table 15. Comparison between the bandgap values of CuAlO_2 thin films deposited by D. C. and reactive sputtering.

D. C. sputtered films						Reactive D. C. sputtered films	
$T_a = 30$ min		$T_a = 60$ min		$T_a = 90$ min		$E_{g\text{-direct}}$ (eV)	$E_{g\text{-indirect}}$ (eV)
$E_{g\text{-direct}}$ (eV)	$E_{g\text{-indirect}}$ (eV)	$E_{g\text{-direct}}$ (eV)	$E_{g\text{-indirect}}$ (eV)	$E_{g\text{-direct}}$ (eV)	$E_{g\text{-indirect}}$ (eV)		
3.81	2.8	3.7	2.1	3.8	2.32	3.90	1.89

(v) Electrical properties and Hall studies

Temperature variation of the conductivity of reactive D. C. sputtered CuAlO_2 thin film has also been studied in the temperature range of 300 K to 550 K according to **Eq. 18**. In this

case also the contacts were made by silver paint and the ohmic *nature* of the contacts were verified accordingly. **Fig. 30** represents $\ln \sigma$ vs. $1000/T$ plot of the reactive sputtered CuAlO_2 thin film on glass substrate. The film thickness was ~ 500 nm obtained from cross-sectional SEM (not shown here). The temperature variation of conductivity of the CuAlO_2 thin films were studied below the room temperature by previous authors [64, 67], but no study on high temperature conduction was reported. The straight-line *nature* of the Arrhenius plot indicates the thermally activated conduction as often found in semiconductors. Room temperature conductivity of the film was obtained as 0.22 S cm^{-1} , which is comparable to that obtained by D. C. sputtered films post-annealed for 60 min. From the slope of the graph we get the value of activation energy (E_a) which corresponds to the minimum energy required to transfer carriers from acceptor level to the valence band and the value of E_a comes out as 250 eV, which is comparable to that of D. C. sputtered films post-annealed for 60 min.

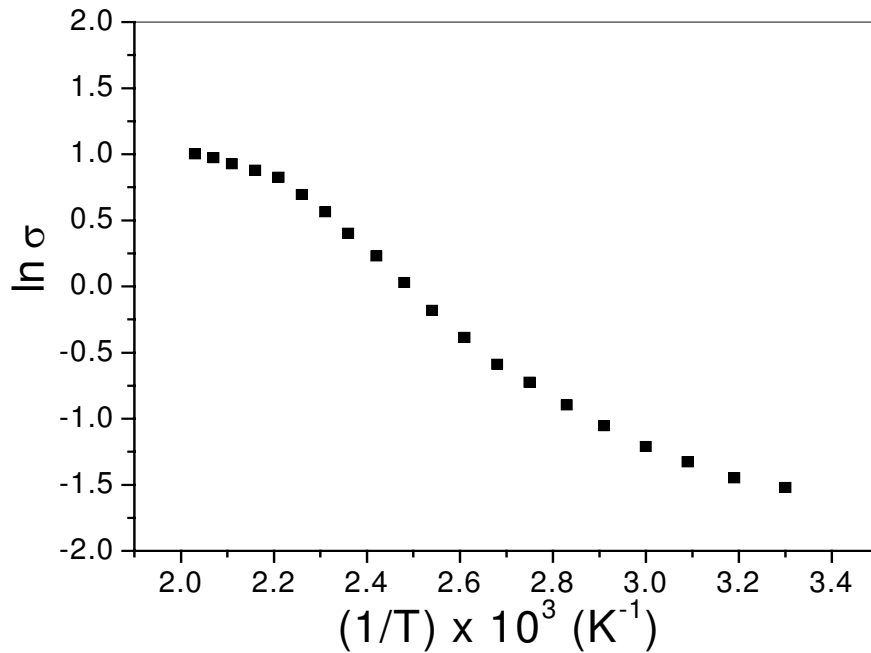


Figure 30. Temperature variation of conductivity of reactive sputtered CuAlO_2 thin film.

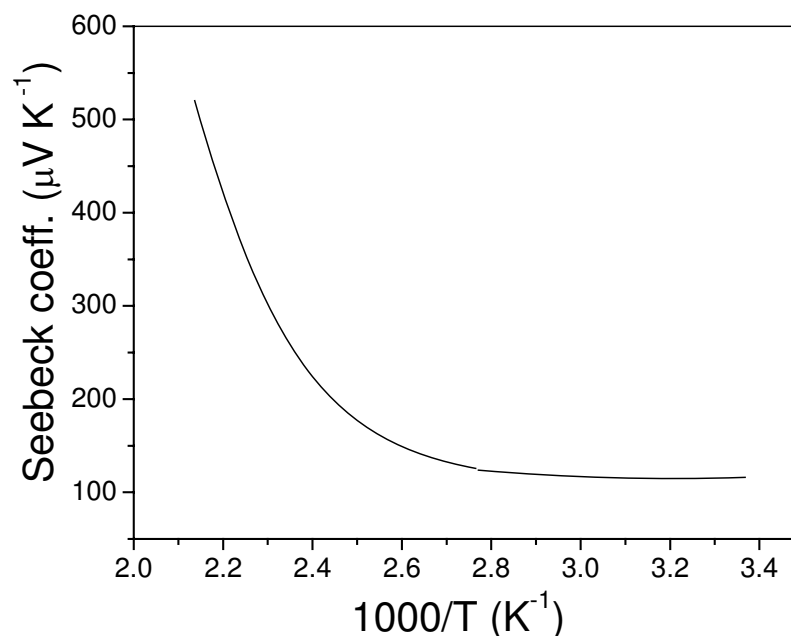
Hall measurements of reactive D. C. sputtered films were done at room temperature. Hall coefficient of the films was determined to be $R_H = 14.1 \text{ cm}^3 \text{ C}^{-1}$, corresponding to carrier density $4.4 \times 10^{17} \text{ cm}^{-3}$. Positive value of Hall coefficient confirmed the p-type conductivity of the film. The carrier concentration of this film is comparable to that of D. C. sputtered film post-annealed for 60 min. As far as conductivities of previously reported reactive sputtered copper aluminium oxide films are concerned, Tsuboi et al [147] obtained phase impure copper aluminium oxide films (a mixture of CuAlO_2 and Cu_2O) with maximum conductivity around 0.1 S cm^{-1} . A comparison between the electrical parameters of reactive sputtered film and D. C. sputtered films is furnished in **Table 16**.

Table 16. Comparison between the electrical properties of reactive sputtered and D. C. sputtered films.

Synthesis technique	t_a (min)	σ_{RT} (S cm^{-1})	E_a (meV)	R_H ($\text{cm}^{-3}\text{C}^{-1}$)	n (cm^{-3})
Reactive sputtering	60	0.22	250	+ 14.1	4.4×10^{17}
D. C. Sputtering	30	0.09	270	+ 22.5	2.8×10^{17}
	60	0.16	245	+ 13.9	4.5×10^{17}
	90	0.39	196	+ 4.60	1.2×10^{18}

(vi) Thermoelectric properties

Thermoelectric properties of reactive sputtered CuAlO_2 film show almost similar *nature* as those of D.C. sputtered films (cf. **Fig. 22**). **Fig. 31** shows the temperature dependence of Seebeck coefficient. The room temperature Seebeck coefficient (S_{RT}) is found to be $+115 \mu\text{V K}^{-1}$, which lies between that of D. C. sputtered films with $t_a = 30$ min and 60 min (cf. **Table 12**). Positive values of the Seebeck coefficients also confirm the p-type *nature* of the films. The Seebeck coefficients range from $+115 \mu\text{V K}^{-1}$ to $520 \mu\text{V K}^{-1}$, at 300 K to 470 K respectively. The Fermi energy of reactive sputtered film has been calculated from the slope of the linear portion of the curve in **Fig. 31**, near room temperature, according to the **Eq. 20**. The Fermi energy as obtained is 100 meV, which is slightly less than that of the D. C. sputtered film with $t_a = 90$ min (cf. **Table 12**). This type of band structure is typical of a non-degenerate semiconducting material with Fermi level lying between acceptor level (which corresponds to the activation energy, $E_a = 250$ meV) and the top of the valence band.

Figure 31. Temperature variation of Seebeck coefficient of reactive sputtered CuAlO_2 thin film.

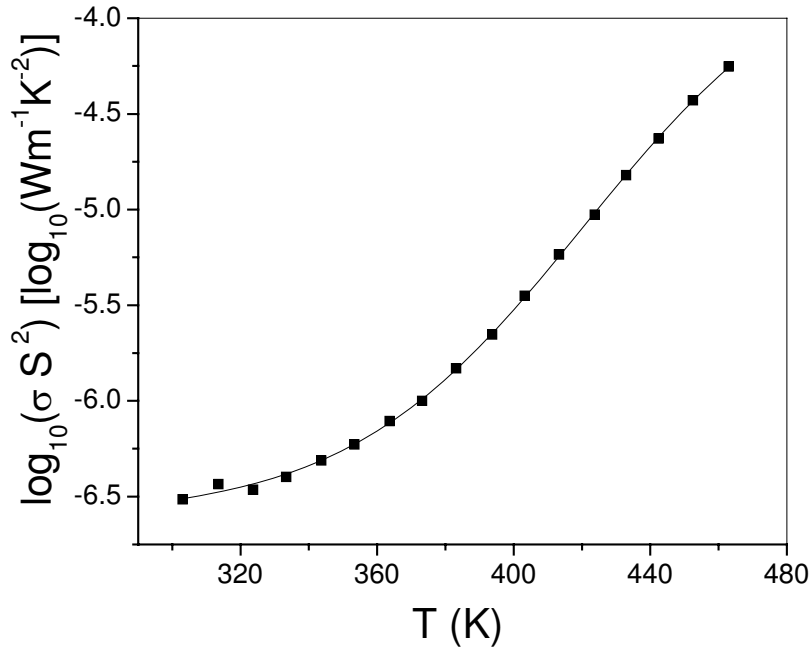


Figure 32. Temperature variation of thermoelectric power factor of reactive sputtered CuAlO_2 thin film.

Fig. 32 represents the temperature dependence of thermoelectric power factor (σS^2) of CuAlO_2 thin film for the temperature range of 300 K to 460 K. The values range from $3.09 \times 10^{-7} \text{ Wm}^{-1}\text{K}^{-2}$ at temperature around 300 K to $5.5 \times 10^{-5} \text{ Wm}^{-1}\text{K}^{-2}$ around 460 K. These are also comparable to those of D. C. sputtered films. A comparison between different thermoelectric parameters of D. C. sputtered and reactive sputtered films is furnished in **Table 17**.

Table 17. Different thermoelectric properties of D. C. sputtered and reactive sputtered CuAlO_2 thin films with different post-deposition oxygen annealing times (t_a).

Synthesis technique	t_a (min)	S_{RT} ($\mu\text{V K}^{-1}$)	E_f (meV)
Reactive D. C. sputtering	60	+ 115	100
D. C. Sputtering	30	+ 120	200
	60	+ 141	151
	90	+ 230	130

5.3. Properties of Wet-Chemical Dip-Coated Films

(i) Structural properties

Beside physical processes like D. C. sputtering and reactive sputtering, we have also synthesized CuAlO_2 thin film by wet-chemical dip-coating process. The experimental procedure is furnished in details in **Section 4.3**. **Fig. 33** shows the XRD pattern of the dip

coated copper aluminium oxide thin film on glass substrate. The pattern reveals a strong (006) orientation of CuAlO_2 phase. Very small peaks of (012), (107), $(00\bar{1}2)$, (116) and (119) reflections have also been observed. As the intensities of these peaks are quite small (7 % to 2 %) compared to the (006) peak, so our film shows a preferential (006) orientation. A comparison with vacuum deposited films (PLD-process by Kawazoe et al. [64], Yanagi et al. [67] and sputter-deposited by us [160, 161]) shows similar (006) orientation. As far as the copper aluminium oxide films deposited by solution processes are concerned, Tonooka et al. [153] had not reported any XRD data of the film. But the XRD data of the powdered samples were shown, which depicted the presence of a mixture of CuAlO_2 , CuO and CuAl_2O_4 phases in the sample. But they suggested that the powdered sample prepared by nitrate route (at 1100°C) would give maximum percentage of CuAlO_2 phase with a strong (012) orientation. It is worthwhile to mention that, for XRD pattern of CuAlO_2 powdered sample, all the previous reports showed a high (012) orientation, whereas in the thin film, a strong (006) orientation was observed [64, 67, 160]. On the other hand, Ohashi and co-authors [157] reported the XRD pattern of their sol-gel deposited multiphase copper aluminum oxide films which consisted of a mixture of CuAlO_2 , CuO and Cu_2O . As shown in our XRD pattern (**Fig. 33**), a small peak of $\text{Cu}_2\text{Al}_2\text{O}_4$ phase has been observed [113]. As its intensity is as low as 7 % of the (006) peak of CuAlO_2 phase, so it may be concluded that our copper aluminium oxide thin film has very high percentage of CuAlO_2 phase with a strong (006) orientation. Also no peaks of starting materials (e.g. CuCl and AlCl_3) or any reactant species such as metal oxides have been found in the pattern. It is noteworthy that synthesis of copper aluminium oxide thin films by spray technique [156] at 525°C yielded amorphous films. But a transition to crystalline *nature* was observed at a deposition temperature of 570°C with a small (101) reflection of CuAlO_2 phase. But this film also not phase pure as it contained small amount of CuO phase as depicted from their XRD pattern [156].

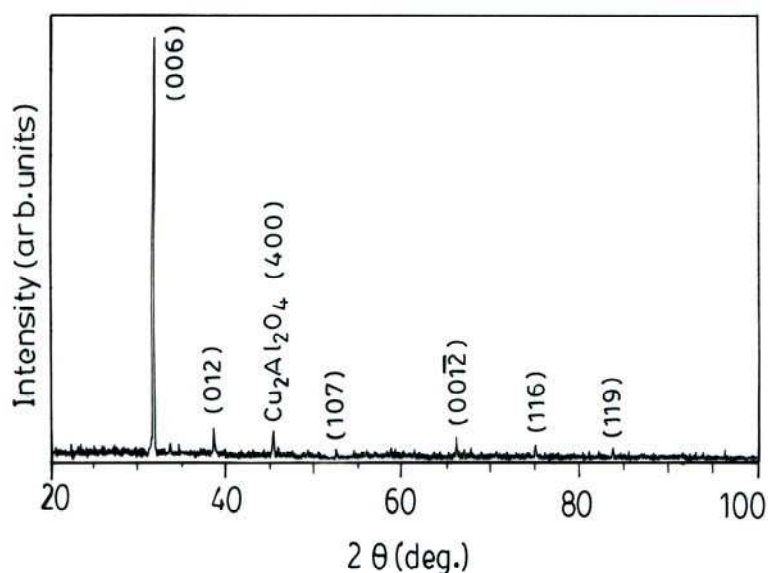


Figure 33. XRD pattern of copper aluminium oxide thin film deposited on glass substrate.

(ii) Surface morphology

Fig. 34 shows the scanning electron micrograph (SEM) of a typical CuAlO_2 thin film deposited on glass substrate. Existence of a smooth surface with finer grains and well defined grain boundaries are observed and with some bigger clusters dispersed on the surface, which resulted due to the agglomeration of finer grains. Cross-sectional SEM reveals the thickness of the film around $\sim 1.5 \mu\text{m}$.

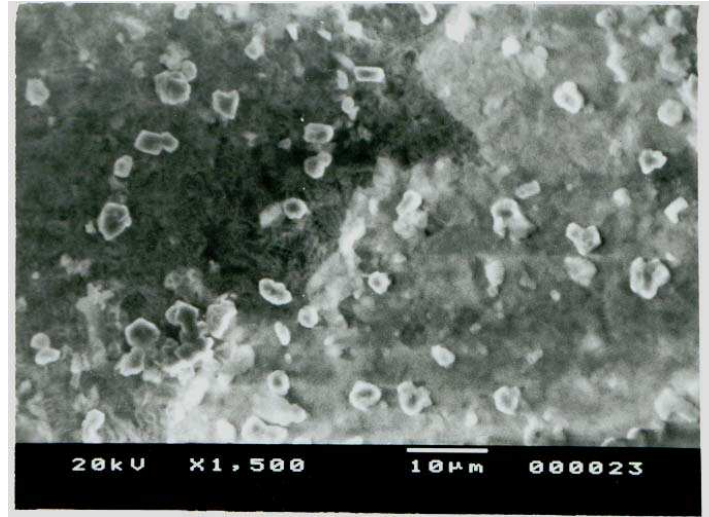


Figure 34. SEM micrograph of copper aluminium oxide thin film on glass substrate.

Previously, Ohashi et al. [157] reported the SEM micrograph of their sol-gel dip-coated copper aluminium oxide film and observed a smooth surface with fine particles but interior of the film was found to be porous with larger grains. On the other hand, Bouzidi et al. [156] reported very smooth surface morphology of their copper aluminium oxide thin film deposited by spray technique at 500°C , cross-sectional SEM of which revealed the thickness of their film $\sim 1 \mu\text{m}$.

(iii) Optical properties

Fig. 35 shows the transmission spectrum of copper aluminium oxide thin film deposited on glass substrate in the wavelength range of 300 nm to 800 nm, taking similar glass as reference. It shows nearly 90 % transmittance in the wavelength range of 500 nm to 800 nm.

From the transmittance data, using Manifacier model [254] we have calculated the absorption coefficients (α) at the region of strong absorption by re-writing **Eq. 16** (neglecting reflectance, R) as follows:

$$\alpha = \frac{1}{d} \ln\left(\frac{1}{T}\right) \quad (23)$$

where d is the film thickness and T is the transmittance obtained from **Fig. 35**.

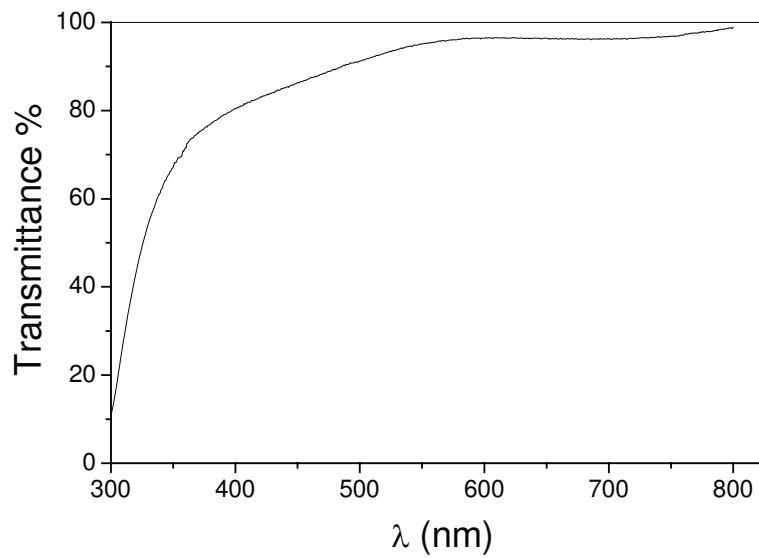


Figure 35. Transmittance vs. wavelength plot of copper aluminium oxide thin film deposited on glass substrate.

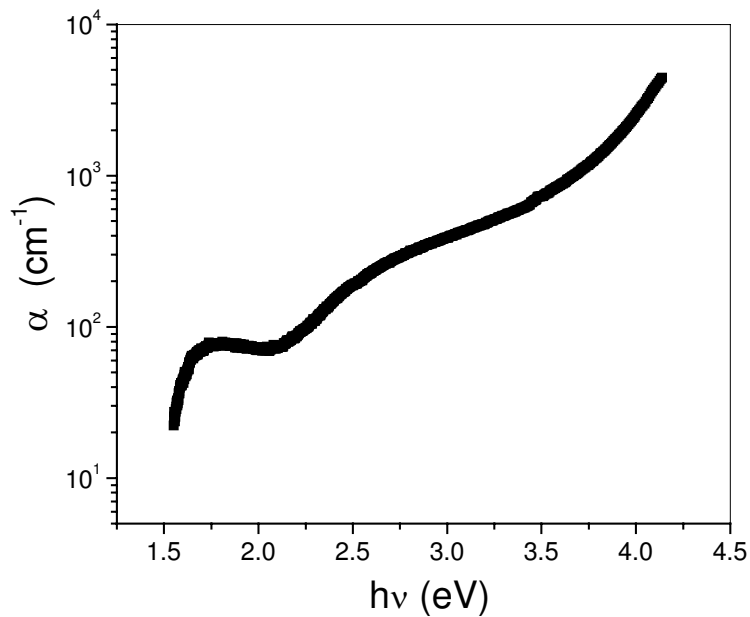


Figure 36. Energy dependence of absorption coefficient of CuAlO_2 thin film prepared by dip-coating process.

Fig. 36 shows the spectral variation of absorption coefficient for wet-chemical dip-coated copper aluminium oxide thin film. The value of α varies from 22.0 to $4.5 \times 10^2 \text{ cm}^{-1}$ in the wavelength range of 300 to 800 nm . **Fig. 37** represents the spectral variation of extinction coefficient (k) according to the **Eq. 14**. The value of k varies from 1.42×10^{-3} to 106.23×10^{-3}

in the spectral range of 300 to 800 nm. These values are comparable to the D.C. sputtered as well as reactive sputtered films shown in **Fig. 15**, **16**, **17** and **Fig. 29**.

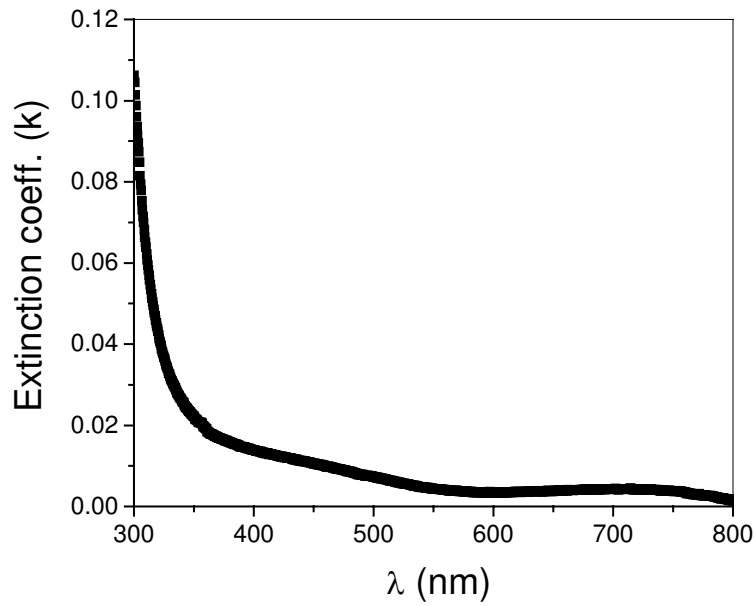


Figure 37. Spectral variation of extinction coefficients (k) of copper aluminium oxide thin film deposited by wet-chemical method.

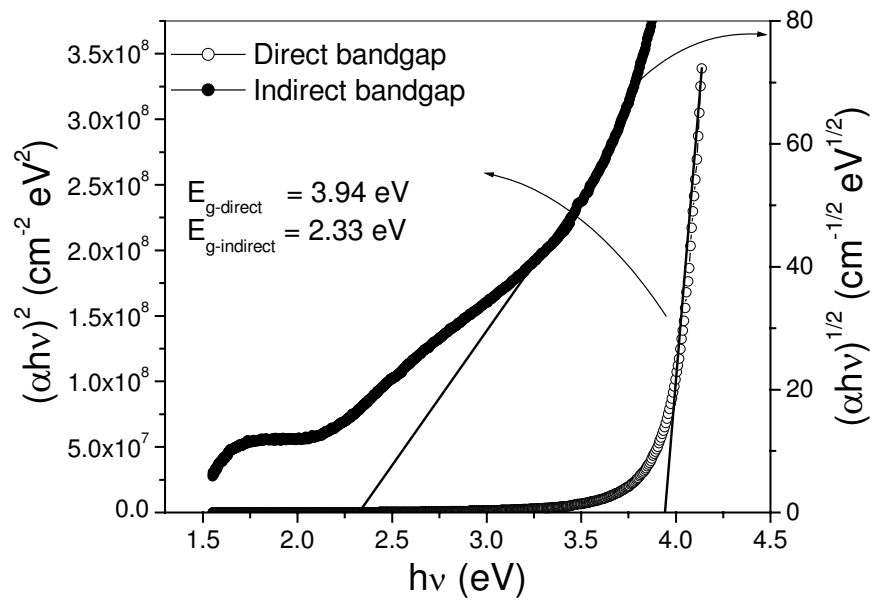


Figure 38. Plot to determine direct bandgap of copper aluminium oxide thin film.

Using these values of α the *nature* and value of the optical band gap has been determined according to **Eq. 17**. To determine the possible transitions, $(\alpha h\nu)^{1/n}$ vs. $h\nu$ were plotted for different values of n . The $(\alpha h\nu)^2$ and $(\alpha h\nu)^{1/2}$ vs. $h\nu$ plots are shown in the **Fig. 38**. Extrapolating the linear portion of the graphs to the $h\nu$ axis we have obtained the direct and indirect band gap values as 3.94 eV and 2.33 eV respectively. As far as bandgap value of chemically deposited copper aluminium oxide is concerned, Bouzidi et al [156] reported the direct bandgap for their spray-deposited copper aluminium oxide as 3.87 eV. Also these values nearly agree with the value reported previously by others [64, 67] and us [160, 161]. **Table 18** compares the various optical parameters of chemically deposited copper aluminium oxide films with that of D. C. sputtered and reactive sputtered CuAlO_2 films by us.

Table 18. Comparison of different optical parameters of wet-chemical deposited CuAlO_2 thin film with that of physically deposited films.

Process	Post-annealing time (min)	Average visible transmittance (%)	Bandgap (E_g)	
			Direct (eV)	Indirect (eV)
Wet-chemical	---	80	3.94	2.33
D. C. sputtering	30	65	3.81	2.80
	60	80	3.70	2.10
	90	75	3.80	2.32
Reactive sputtering	60	85	3.90	1.89

(iv) Electrical properties

Electrical properties of chemically deposited copper aluminum oxide thin films have been studied by standard four-probe methods. All electrical contacts were made by silver paint, which showed linear I-V characteristics over a wide range of voltages and temperatures. **Fig. 39** represents $\ln\sigma$ vs. $1000/T$ plot of the copper aluminum oxide film on glass substrate from room temperature (300 K) to 570 K. The straight-line *nature* of the Arrhenius plot indicates the thermally activated conduction, as often found in semiconductors. Room temperature conductivity of the film was obtained as $4.0 \times 10^{-3} \text{ S cm}^{-1}$. This value is quite comparable to the previously reported copper aluminum oxide films prepared by chemical routes ($5.0 \times 10^{-3} \text{ S cm}^{-1}$ by Tonooka et al. [153], $4.0 \times 10^{-3} \text{ S cm}^{-1}$ by Bouzidi et al. [156]). As far as CuAlO_2 films prepared by physical processes are concerned, this value is one order less than that obtained by Kawazoe et al. [64] (0.095 S cm^{-1}) for their pulsed laser deposited film. Also a comparison with sputter deposited films prepared by us [160, 161], this value comes out to be two orders of magnitude less as shown in **Table 19**. This may be due to the higher number of defect states formed within the film. It is generally observed that the films produced by SGDC route contains higher defect states than that produced by vacuum deposited films. Proper regulation of the deposition parameters as well as intentional substitutional doping of the film are required to increase the conductivity which is the next aim of our work.

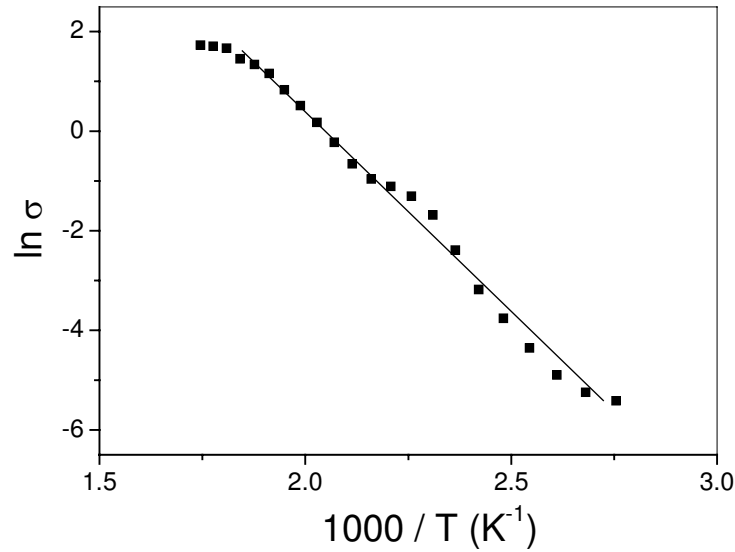


Figure 39. Temperature variation of conductivity of copper aluminum oxide thin films.

Table 19. Comparison between different electrical parameters of CuAlO₂ thin films, deposited by various processes.

Process	Post-annealing time (min)	σ_{RT} (S cm ⁻¹)
Wet-chemical	---	0.004
DC sputtering	90	0.39
	60	0.16
	30	0.09
	120	0.055
	150	0.014
Reactive sputtering	60	0.22

Thermoelectric power (TEP) of the CuAlO₂ thin films deposited on glass substrates was measured over the temperature range 308 – 488 K. Room temperature Seebeck coefficient was found to be +206 $\mu\text{V K}^{-1}$. Positive values of Seebeck coefficients confirmed the p-type conductivity of the film. Also Hot-probe measurement confirms the p-type *nature* of the films.

6. Transparent Junctions

Fabrication of transparent junction is the most important aspect in the field of p-TCO technology. Amongst various junctions, transparent p-n heterojunction diode is the simplest one with rectifying properties. It is also the simplest structure to fabricate. We have synthesized n-ZnO: Al / p-CuAlO₂ heterojunction diode on glass substrates with considerable electro-optical properties. The process and results are furnished below.

6.1. Fabrication of All-Transparent Diode

The all-TCO p-n hetero-junction diode having the structure: n-ZnO: Al / p-CuAlO₂ were fabricated on glass substrates. The n-type layer was taken as aluminum doped zinc oxide films (ZnO: Al), which was deposited on commercial glass substrates (of size 18 mm X 8 mm) by Sol-Gel-Dip-Coating technique. Thereafter these n-layer coated glasses were used as the substrates for the deposition of p-layer (p-CuAlO₂ film) by D. C. sputtering technique. Six independent junctions (1 mm X 1 mm) were fabricated on a single substrate using proper masking. Details of the deposition procedures are furnished below.

Deposition of n-layer: ZnO films were deposited on glass substrates by SGDC route from a starting solution of zinc acetate dihydrate ($\text{Zn}(\text{CH}_3\text{COO})_2 \cdot 2\text{H}_2\text{O}$) and isopropyl alcohol ($\text{Pr}^i\text{-OH}$). Since zinc acetate has low solubility in isopropyl alcohol, diethanolamine (DEA) was added (with $[\text{DEA}]/[\text{Zn}^{2+}] = 1.5$) to get transparent solution and to keep the solution stable in dip-coating process. Doping of Al was done by the addition of controlled amount of aluminum nitrate ($\text{Al}(\text{NO}_3)_3 \cdot 9\text{H}_2\text{O}$) to the solution. Then the resultant solution was stirred and refluxed, keeping the temperature at 343 K for one hour. The atomic ratio of Al/Zn in the initial solution was varied from 0.32 % to 1.62 % and the concentration of zinc acetate was fixed at 0.85 mol/L. Distilled water (with $[\text{H}_2\text{O}]/[\text{Zn}^{2+}] = 14$) and acetic acid (with $[\text{H}^+]/[\text{Zn}^{2+}] = 2$) were added for better stability of the solution and to avoid gelation or precipitation. The pH of the solution was kept around 7.0. Lastly, stirred and refluxed solution was aged for half an hour to get the resultant solution. Then the ultrasonically cleaned glass substrates were dipped vertically into the solution and withdrawn at a speed of 8 cm/min to coat them with the required material. The coated substrates were dried at room temperature for 10 minutes and heated at ~ 423 K for 10 minutes in open atmosphere for gelation. This process was repeated for 2-3 times for getting a desired thickness. Finally the films were heated at 573 K for one hour to obtain crystalline ZnO: Al films. The details of the deposition conditions were reported elsewhere [255]. It is to be noted that although the Al concentration in the starting solution was varied from 0.32 % to 1.62 % to get $\text{Zn}_{1-x}\text{Al}_x\text{O}$ films with varied opto-electrical properties, but for the fabrication of the diode, those films were chosen which were having Al concentration of 1.62 % in the starting solution. This is because of the better comparability of the electrical and optical properties of these films with the corresponding p-layer (CuAlO₂ films).

Deposition of p-layer: The n-layer coated glass was used as the substrate in the D. C. sputtering process to deposit p-CuAlO₂ thin film. Mica masks were used on the n-ZnO: Al coated glass substrates for preferential deposition of p-CuAlO₂ layers on desired position. Initially, solid-state reaction between stoichiometric ratios of Cu₂O and Al₂O₃ powder at 1400 K produced CuAlO₂ powder. This powder was then pressed into a pellet and was used as a target for D. C. sputtering. The sputtering unit was evacuated by standard rotary-diffusion arrangement upto a base pressure of 10^{-6} mbar. The pellet was arranged properly by aluminum holder to act as upper electrode and the negative terminal of the D. C. power supply unit was connected to it. n-layer coated glass substrates were placed on the lower electrode and connected to the ground of the power supply. The electrode distance was taken as 1.8 cm. Ar and O₂ (3 : 2 vol. ratio) were taken as sputtering gas and the sputtering was done at an elevated substrate temperature (~ 453 K) to achieve high crystallinity in the film. Post-deposition annealing of the film (at 473 K) for 30 min in an O₂ atmosphere (at a pressure of 0.2 mbar) was performed to induce nonstoichiometry in the film for enhancing p-type

conductivity. Details of the deposition conditions are furnished in details in **Section 4.1** (cf. **Table 6**). A flow-chart of the diode fabrication process is shown in **Fig. 40** and the corresponding schematic diagram of the diode structure is given in **Fig. 41**.

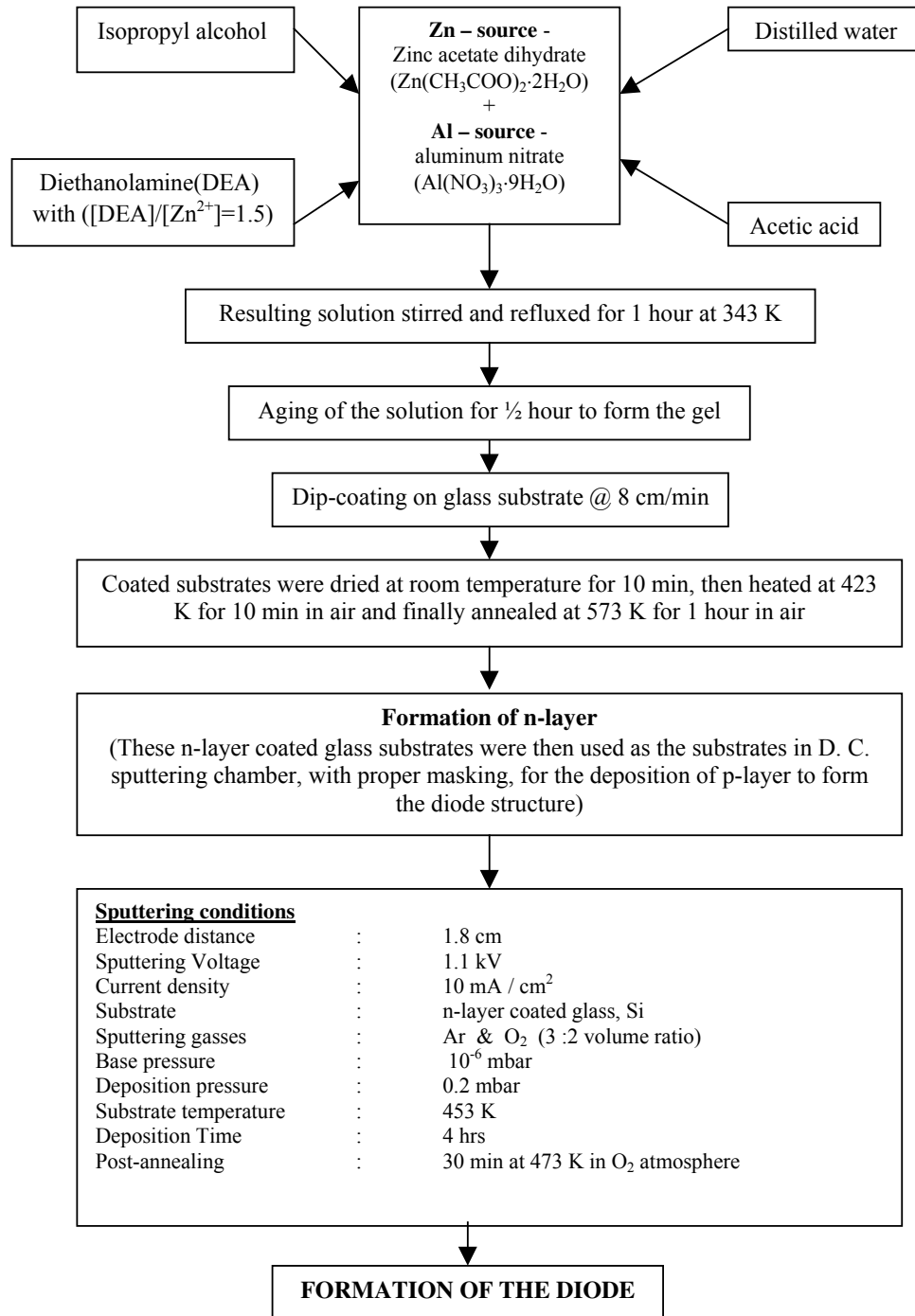


Figure 40. Flow-chart of the diode fabrication.

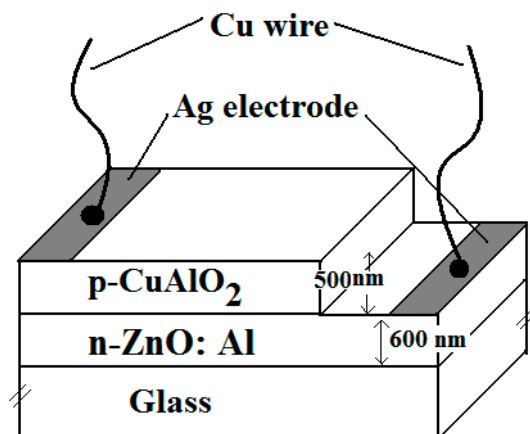


Figure 41. Schematic diagram of n-ZnO: Al / p-CuAlO₂ diode structure.

The optical transmittance of the diodes was measured by UV-Vis-NIR spectrophotometer (SHIMADZU-UV-3101-PC). All electrical measurements were done by standard four-probe method using Keithley-6514 electrometer under vacuum condition ($\sim 10^{-3}$ mbar). For ohmic contacts, evaporated silver electrodes were used with proper masking in both types of layers, which showed linear I-V characteristics over a wide range of voltages and temperatures. Thereafter the electrical connections were made by Cu leads with silver paints, as shown in Fig. 41.

6.2. Characterizations of the Diode

Structural properties of the films were studied by X-ray diffractometer (XRD, BRUKER, D8, ADVANCE) using the $\text{Cu K}\alpha$ (1.5406 Å) radiation. Fig. 42 shows the XRD patterns of individual layers of CuAlO_2 (pattern-a) and ZnO: Al (pattern-b) on glass substrates respectively, deposited under the same conditions as that used for diode fabrication. All the peaks match with the standard JCPDS files (# 35-1401, for CAO [113]) and (# 36-1451, for ZnO) respectively, as shown by the circles and lines in the figure. The XRD pattern for CuAlO_2 is similar to that given in Fig. 8(b). Also no peaks of starting materials and any other reactant species have been found which conclusively indicate that the reactants were completely mixed to form the proper phase of the materials. As stated earlier, the XRD pattern of the p-layer is obtained for p- CuAlO_2 thin film deposited on bare glass substrate under the same conditions as that used for diode fabrication. But it is worthwhile in mentioning that, here we have not taken into account the change in crystal quality of the p-layer due to the presence of ZnO: Al layer underneath, to fabricate the diode. It must be admitted that the crystal structure of ZnO: Al film might affect the crystal quality of the CuAlO_2 in terms of intensity and sharpness of the XRD peaks. And it might not be unreasonable to speculate that the presence of crystalline ZnO film underneath might have improved the crystal quality of CuAlO_2 film with respect to bare glass substrate, which, in turn, enhances the formation of rectifying junction.

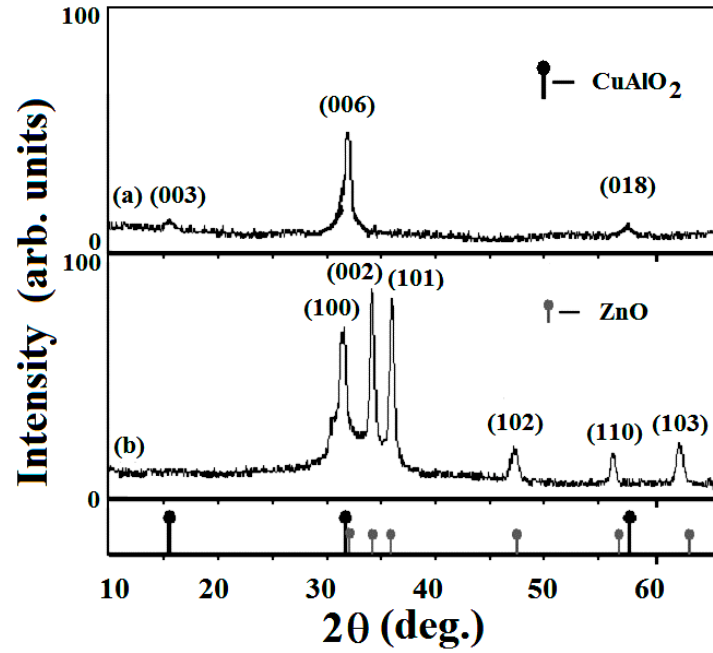


Figure 42. XRD patterns of (a) p-CuAlO₂, (b) n-ZnO: Al films. Lines and circles represent the reference patterns of corresponding materials.

The optical transmission spectrum of the n-ZnO: Al / p-CuAlO₂ diode is shown in **Fig. 43**. As mentioned earlier, the thickness measurements were done by cross-sectional

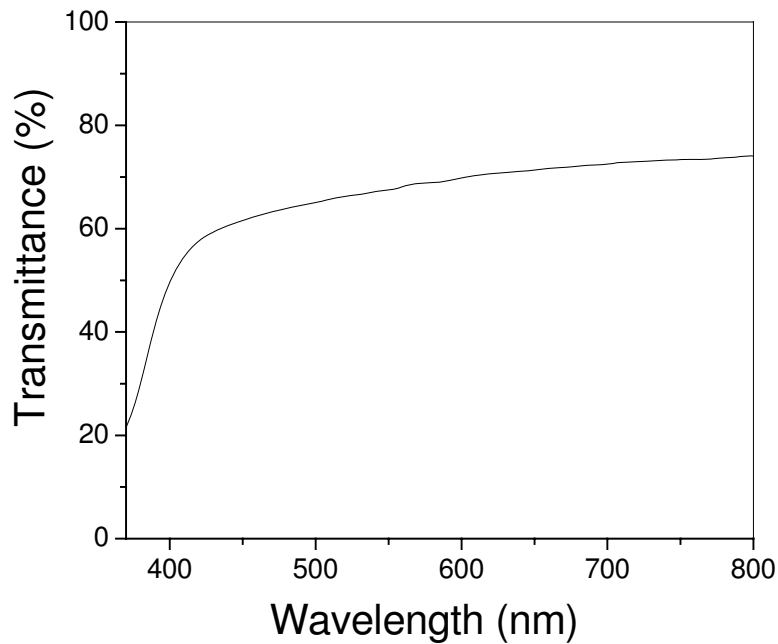


Figure 43. Optical transmission spectra of the n-Zn_{1-x}Al_xO / p-CuAlO_{2+x} diode deposited on glass substrate.

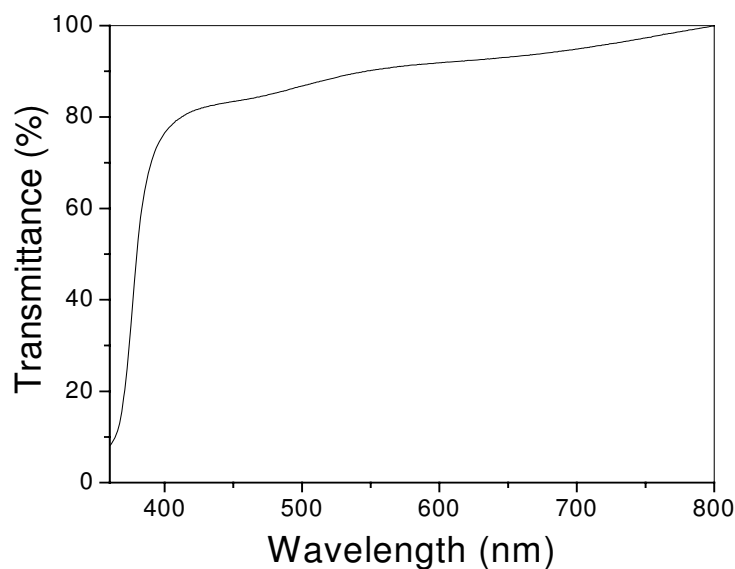


Figure 44. Optical transmission spectra of n-ZnO: Al film.

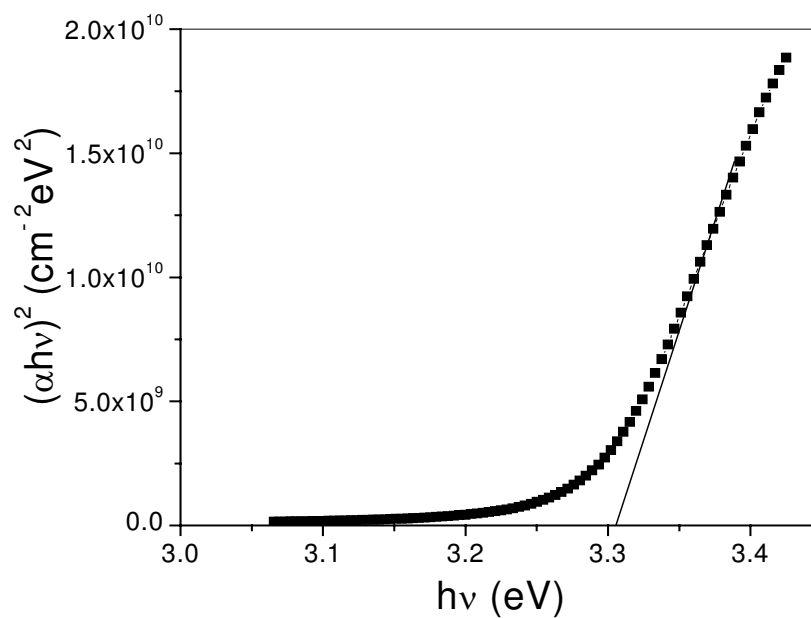


Figure 45. Determination of direct bandgap of n-ZnO: Al film.

SEM (not shown here). The thicknesses were found to be 600 nm for ZnO: Al film and 500 nm for CuAlO_2 film respectively, making the total device thickness around 1100 nm as shown in the inset of **Fig. 41**. The visible transparency of the diode is around 60 %, which indicates its potential application in ‘Invisible Electronics’ [65]. It is to be noted that the visible transparency of the individual p-layer with identical deposition condition as that used for diode fabrication is around 75 % as shown in **Fig. 13, Section 5.1**. On the other hand, the

visible transparency of the n-layer is around 80% as shown in **Fig. 44**. A comparison of these spectra shows that the starting point of the fundamental absorption region of the diode structure is comparable to that of n-ZnO: Al layer, which is having lower bandgap energy (3.31 eV, as shown in **Fig. 45**). Previously, Tonooka et al. [172] obtained the average visible transmittance of their n⁺-ZnO / n-ZnO / p-Cu-Al-O diode around 60 %. As far as other all-oxide transparent diodes are concerned, Sato et al. [66] reported 20 % visible transmittance for their p-NiO / i-NiO / i-ZnO / n-ZnO structure, Kudo et al. [165] obtained 70 % - 80 % visible transmittance for p-SrCu₂O₂ / n-ZnO diode, Hoffman and co-authors [170] reported 35 % to 65 % visible transmittance in a p-CuY_{1-x}Ca_xO₂ / n-Zn_{1-x}Al_xO / n⁺-ITO heterojunction diode, Yanagi et al. [103] obtained 60 % to 80 % transmittance for their p-CuIn_{1-x}Ca_xO₂ / n-CuIn_{1-x}Sn_xO₂ homojunction diode in the visible region.

Electrical properties of the individual layers have been studied in details and represented in our previous literatures [243, 244, 255]. **Fig. 46** represents the temperature variation of individual n- and p-layers deposited under identical conditions as that during diode fabrication. A comparative study of different electro-optical properties of the individual films is furnished in **Table 20**. For proper fabrication of rectifying junction, a comparable electro-optical property of the individual p- and n-layers is very important, and in that respects ZnO: Al film is widely used because of its easy controllability of carrier concentration by varying percentage of Al during deposition. This is necessary in order to match the carrier concentrations with those positive holes in p- CuAlO₂ which is more difficult to control. Also possibility of low-temperature deposition of crystalline ZnO films on glass as well on as plastic substrates [61] has make ZnO films one of the most promising component for the fabrication of transparent diodes in the field of ‘Invisible Electronics’.

Table 20. Different electrical and optical properties of individual p-CuAlO₂ layer (cf. Table 11, 12) and n ZnO: Al layers [255].

Film	Direct bandgap ($E_{g-direct}$) eV	Room-temperature conductivity (σ_{RT}) (S cm ⁻¹)	Activation energy (E_a) (meV)	Fermi energy (E_f) (meV)	Carrier concentration (n) (cm ⁻³)
n-ZnO: Al	3.31	0.08	550	280	2.6×10^{17}
p-CuAlO ₂	3.81	0.09	270	200	2.8×10^{17}

The current-voltage characteristics of the transparent diodes have been measured by Keithley-6514 electrometer. For ohmic contacts, evaporated silver electrodes were used with proper masking in both types of layers, which showed linear I-V characteristics over a wide range of voltages and temperatures. Thereafter the electrical connections were made by Cu leads with silver paints. The I-V characteristic of the diode is shown in **Fig. 47**, which shows rectifying properties, indicating proper formation of the junction. The turn-on voltage obtained around 0.8 V. However, it varied from 0.6 V to 1.0 V from junction to junction. This indicates considerable reproducibility of the junctions. The forward-to-reverse current ratio is approximately ~ 30 at ± 4 V. Maximum current obtained at 5 V is around 1 μA and a small leakage current as low as 30 nA was observed at a reverse bias of -4 V. Previously, Tonooka et al. [172] reported the average turn on voltage of their n-ZnO/p-Cu-Al-O diode ~ 0.5 V,

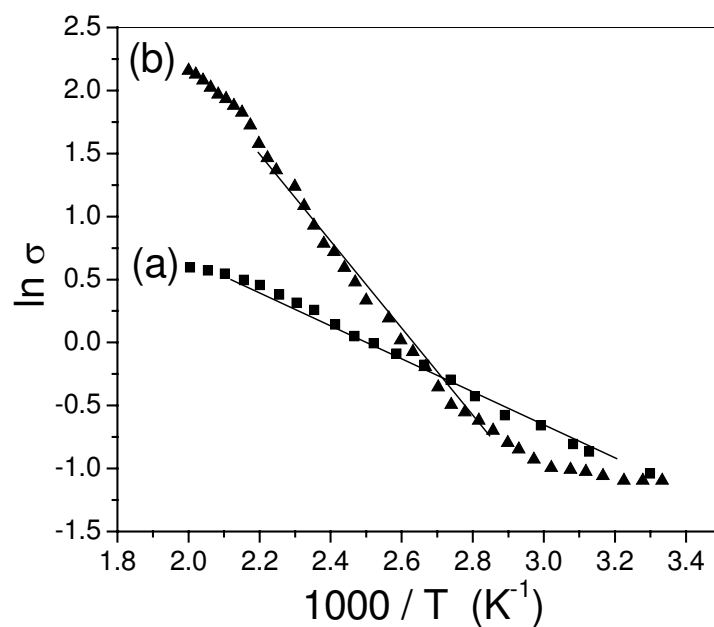


Figure 46. Temperature variation of conductivity of (a) p-CuAlO₂ and (b) n-ZnO: Al films.

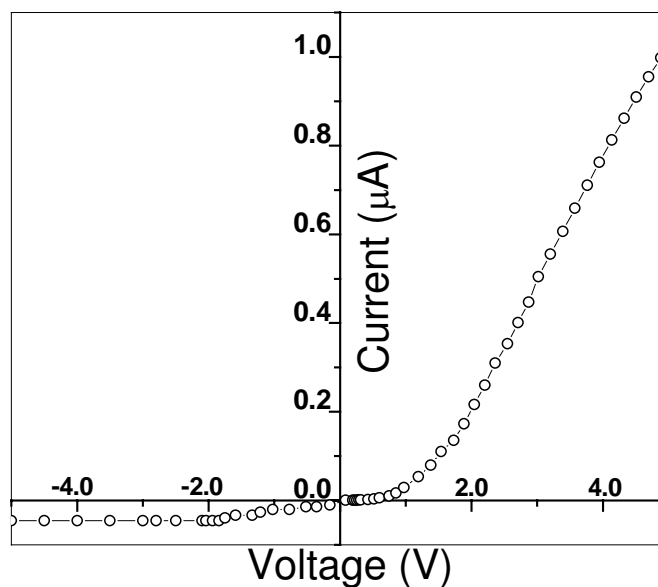


Figure 47. Current–Voltage characteristics of p-CuAlO₂ / n-ZnO: Al diode.

which is comparable to ours. Generally, for heterojunction diodes, the structural imperfections at grain boundaries as well as at the interface deteriorate the efficiency of the diode [165]. Also the inherent difficulty in manufacturing these all-oxide diodes is that the p and n-layers must be produced under oxidizing and reducing conditions respectively, so that optimal processing for one type is detrimental to the other [110]. All these facts must be

addressed with considerable attention for diverse applications of these heterojunction all-oxide transparent diodes in the field of “Invisible Electronics”.

If we probe into the bandstructure of the interface, considering the bandgaps of n-ZnO: Al and p-CuAlO₂ as 3.31 eV (cf. **Fig. 45**) and 3.81 eV (direct), 2.8 eV (indirect, cf. **Fig. 18c**) respectively, then the depletion barrier height comes out within the range of 3.3 eV to 2.3 eV (for this calculation, the position of Fermi level of both p and n type materials are obtained from thermo-electric power measurements of the materials. For p-CuAlO₂ films this value is around 200 meV (cf. **Table 12**) and for n-ZnO: Al films it is around 280 meV [255]. The activation energy values are obtained from **Fig. 46** and furnished in **Table 20**). But these values are quite larger than that of the observed turn-on voltage, which is around 0.8 V. This inconsistency between the turn-on voltage and the barrier height may be explained in the following way: Investigation of previous literatures about the band structure calculations of Mattheis [111] and experimental findings of Cava et al. [225] of similar delafossite p-CuYO_{2+x} material, we see the existence of some midgap impurity bands within the material due to the interstitial oxygen doping, which decreases the effective bandgap of the material. In a similar way it can be argued that in our p-CuAlO₂ thin films, excess oxygen intercalation and probably some unintentional impurity incorporation may give rise to some new and deep states within the bandgap via self-compensation [256], which further reduces the effective bandgap of the material, so also the barrier height. This might provide an explanation of the low turn-on voltage of the p-CuAlO₂ / n-ZnO: Al hetero-junction diode.

7. Nanocrystalline P-CuAlO₂ Thin Films

Fabrication of nanostructured p-TCOs, coupled with the already existing and well-known materials of nanostructured n-TCOs, will give an added impetus in the field of “Invisible Electronics” by creating the opportunity for the fabrication of nano-active devices, which can have highly efficient applications in the optoelectronics device technology. We have synthesized nanostructured p-CuAlO₂ thin films by D.C. sputtering technique by reducing the deposition time and substrate temperature during deposition. Effect of deposition time on crystallinity, particle size, strain, bandgap etc of the film has been investigated. Also photoluminescence properties of this nanocrystalline material have been reported here.

7.1. Preparation of the Nanostructured Film

(i) CuAlO₂ Powder Preparation

Polycrystalline CuAlO₂ powder was synthesized in the same procedure as described in **Section 4.1(i)**. At first Cu₂O and Al₂O₃ powder (both 99.99 %) were taken with Cu / Al atomic ratio 1 : 1 and mixed for 1 hr. Then the mixture was heated in alumina boat at 1100°C for 24 hours in air to form the CuAlO₂ powder. The sintered body was then reground and pressed into pellets by hydrostatic pressure of about 200 kgf / cm². These pellets were placed in aluminum holder by some appropriate arrangement, which was used as the target for sputtering.

(ii) Nanocrystalline CuAlO_2 Film Deposition

The sputtering unit was evacuated by standard rotary-diffusion arrangement upto a base pressure of 10^{-6} mbar. The target was then pre-sputtered for 10 min to remove contamination, if any, from the surface and then the shutter was displaced to expose the substrates in the sputtering plasma. Films were deposited on ultrasonically cleaned glass and Si substrates, which were placed on the lower electrode and connected to the ground of the power supply. Before placing into the deposition chamber the glass substrates were cleaned at first by mild soap solution, then washed thoroughly in deionized water and also in boiling water. Finally they were ultrasonically cleaned in acetone for 15 minutes. Si substrates were first immersed in 20 % HF solution for 2 minutes for removing surface oxide layers. Then they were cleaned in deionized water and finally with alcohol in an ultrasonic cleaner. The electrode distance was taken as 1.5 cm. Ar and O_2 (3 : 2 vol. ratio) were taken as sputtering gases. Details of the deposition conditions were described in **Section 4.1**. Only differences from the previous deposition conditions are the deposition time (t_d), which ranges from 3 min to 45 min (instead of 240 min, cf. **Table 6**) and the lower substrate temperature, which was kept at 373 K (instead of 453 K, cf. **Table 6**). This is because, generally at higher substrate temperature, the particles tend to coalesce to form bigger clusters, which is unwanted for the formation of nano-structured films. The variation in the deposition time is done to observe the changes in the nanostructure and optical properties of the films. Also no post-annealing of the films was performed.

7.2. Characterization and Discussion

The target pellets as well as the films were characterized by X-ray diffractometer (XRD, BRUKER, D8 ADVANCE) to observe the proper phase formation of the material. To study the nanostructure of the films, transmission electron microscopy (TEM, HITACHI-H600) analyses were performed. For TEM measurements, the films were directly deposited on carbon coated copper grids. Optical studies have been performed by measuring the transmittance and reflectance of the films, deposited on glass substrates, in the wavelength region 300 nm - 800 nm using a UV-Vis spectrophotometer (HITACHI-U-3410). Photoluminescence studies were performed by HITACHI F-4500 instrument for the films deposited on Si substrates. The thicknesses of the films were measured by optical interferometric process.

Structural properties: The XRD pattern of the synthesized CuAlO_2 powder, which was used for target preparation has already been presented in **Fig. 7** and described in **Section 5.1**. The peaks of the powdered material confirm the proper phase formation of the required target material. This target material was then used for the thin film preparation.

Four sets of samples were prepared by D. C. sputtering technique having deposition times (t_d) as 3 min, 9 min, 15 min, 45 min, to observe any variation in the XRD patterns and its effect on particle size. Another set of sample is also prepared for deposition time 150 min, which is used as the reference bulk material to compare with the nanocrystalline films. This film has almost similar structural and optical properties as that deposited for 240 min and described in **Section 5.1**. **Fig. 48** represents the XRD patterns of sputter-deposited nanocrystalline CuAlO_2 thin films on Si substrates with deposition times (t_d) 15 min (pattern-

#1) and 45 min (pattern-#2). For the film with $t_d = 15$ min (curve-#1), two broad peaks of (101) and (012) reflections are observed along with two smaller peaks of (107) and (018) reflections. On the other hand for the film deposited in 45 min (curve-#2), a slightly stronger peak of (006) reflections and a small peak of (018) reflections are observed along with the presence of a broad and considerably attenuated hump representing (101) and (012) reflections. It is worthwhile to mention in this connection that in all the previously reported XRD patterns of CuAlO_2 thin films by us (cf. **Fig. 8**) as well as by others [64, 67], a strong (006) orientation were present, whereas the XRD patterns of sintered targets show either a preferred (012) orientation [64] or (101) orientation [67]. Likewise, we have also observed a (101) orientation for the sintered target (cf. **Fig. 7**). But for the films deposited in 15 min, due to smaller deposition time, the film thickness was quite low (~ 90 nm) and quasi-continuous formation of the film restricted the growth of any preferred orientation. And therefore two broad peaks of (101) and (012) reflections are present and as obvious, resemble close to the sintered target. Also, due to the nanocrystalline *nature* of the film, the peaks are quite broader and peak intensities are fairly low. On the other hand, for the films with $t_d = 45$ min, due to longer deposition time, a slightly stronger (006) orientation in the film is observed, along with two considerably attenuated (101) and (012) peaks, which is similar to that reported previously by Kawazoe, Yanagi, Hosono and co-authors [64, 67], for their pulsed laser deposited CuAlO_2 thin films on sapphire substrates. For the films deposited in 150 min, the XRD pattern is almost similar to that shown in **Fig. 8**. A stronger (006) peak is observed along with two smaller peaks of (003) and (018) reflections. This shows that with increase in the deposition time, the films become more and more (006) oriented. Also it is to be mentioned here, that, in the XRD patterns of the films with $t_d = 3$ min and 9 min, due to nanocrystalline *nature* and low film thicknesses (~ 30 nm for $t_d = 3$ min and ~ 60 nm for $t_d = 9$

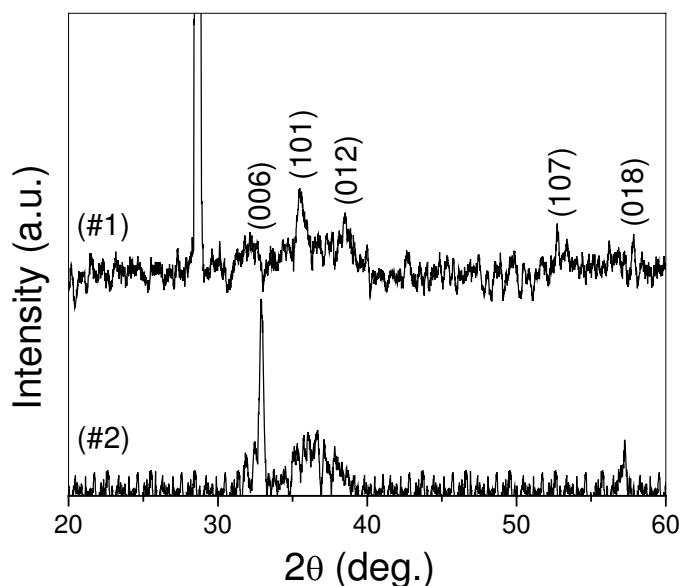


Figure 48. XRD pattern of nano-crystalline CuAlO_2 thin film deposited for (#1) 15 min and (#2) 45 min.

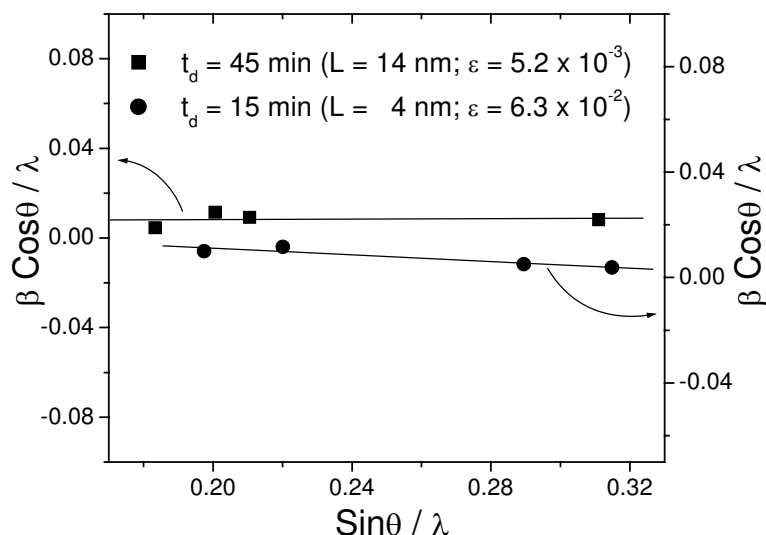


Figure 49. Determination of strain (ϵ) and particle size (L) of the nano-structured CuAlO_2 thin films deposited for 15 min and 45 min.

min), the intensity of the peaks are very low (i.e almost became indistinguishable from the background noise) and therefore no satisfactory representable results were obtained, and that is why not shown here. But the nanocrystalline *nature* of these films were confirmed from transmission electron microscopic measurements and the structural information were extracted from selected area electron diffraction patterns (SAED), which have been described in the later part of this paper.

The information on strain and the particle size of the deposited films were obtained from the FWHMs of the diffraction peaks, according to the **Eq. 6** given in **Section 5.1**. **Fig. 49** represents the plot of $\frac{\beta \cos \theta}{\lambda}$ vs. $\frac{\sin \theta}{\lambda}$ for the films deposited in 15 min and 45 min. From

the slopes and intercepts on y-axes, the strain (ϵ) and particle size (L) were obtained as 5.2×10^{-3} and 14 nm (for $t_d = 45$ min) and 6.31×10^{-2} and 4 nm (for the film with $t_d = 15$ min) respectively. An increase in the particle size with deposition time is observed because of the greater amount of influx of sputtered particles at higher deposition times, leading to the agglomeration of bigger particles. A comparison with these values with bulk film is furnished in **Table 21**.

Table 21. Comparison between the effective particle size and effective strain of D. C. sputtered and reactive D. C. sputtered CuAlO_2 thin films.

Deposition time (t_d) (min)	Effective particle size (nm)	Effective strain
15	4.0	6.31×10^{-2}
45	14.0	5.20×10^{-3}
240 (Bulk film. Cf. Table 14)	26.0	8.52×10^{-3}

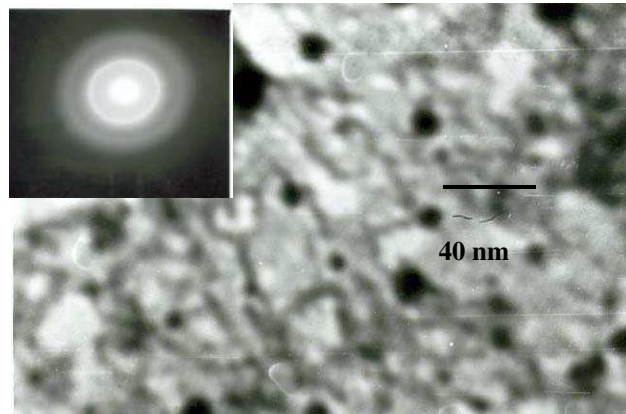


Figure 50(a). TEM micrograph of nano-structured CuAlO_2 thin film deposited for 3 min. **Inset:** SAED pattern of the same.

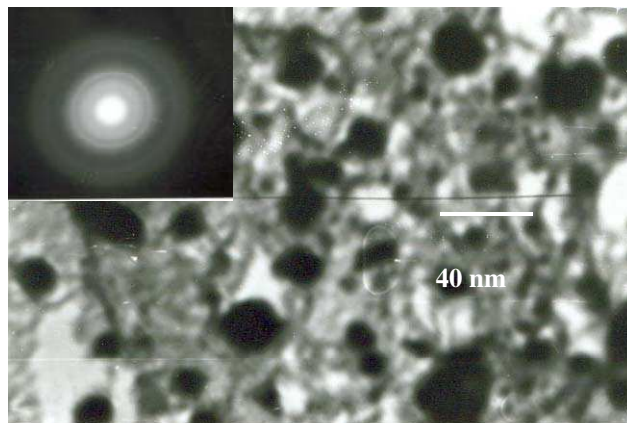


Figure 50(b). TEM micrograph of nano-structured CuAlO_2 thin film deposited for 9 min. **Inset:** SAED pattern of the same.

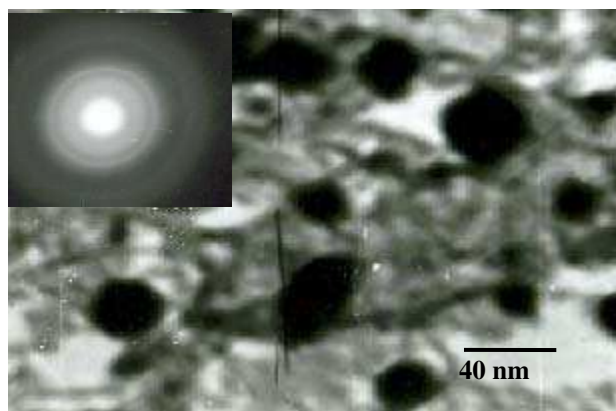


Figure 50(c). TEM micrograph of nano-structured CuAlO_2 thin film deposited for 15 min. **Inset:** SAED pattern of the same.

TEM studies: Transmission electron microscopic (TEM) analyses were done for nanocrystalline CuAlO_2 thin films with various deposition times (t_d). **Fig. 50(a), (b)** and **(c)** show the TEM micrographs of CuAlO_2 films deposited in 3, 9 and 15 min respectively. From the micrographs, the particle sizes (L) are obtained around 8 nm to 12 nm for the films deposited in 3 min (**Fig. 50a**), around 18 to 22 nm for the films deposited in 9 min (**Fig. 50b**) and around 27 to 33 nm for the films deposited in 15 min respectively (**Fig. 50c**). Previously, Gong et al [150] and Gao et al [154] reported the particle size of their nanocrystalline copper aluminium oxide films around 10 nm, which is comparable to our samples deposited in 3 min. Similar to the XRD measurements, here also, from the TEM micrographs we have observed an increase in the average particle size of our nanocrystalline CuAlO_2 thin films with increase in the deposition times. And as already mentioned, this is mainly due to the greater amount of influx of sputtered particles, which results into the agglomeration of bigger particles. Thus the average particle size increases with increase in the deposition time as observed in **Fig. 50(a), (b)** and **(c)** and when the deposition time is 45 min and above, the average particle size (L) becomes ~ 60 nm and more (not shown here). It is also note-worthy that there is a difference in the values of the particle size calculated from XRD data (L_{XRD}) and that obtained from TEM micrographs (L_{TEM}) for the films with $t_d = 15$ min and 45 min. For the films deposited in 15 min, $L_{\text{XRD}} = 4$ nm whereas average $L_{\text{TEM}} \approx 30$ nm. On the other hand, for the films deposited in 45 min, these values are 14 nm and 60 nm respectively. This is because the particle size calculated from **Eq. 6** always gives underestimated value as the term ‘ L ’, in **Eq. 6** is actually the ‘crystallite size’ rather than the ‘particle size’. When the size of individual crystallites in a polycrystalline sample is less than 100 nm, the term ‘crystallite size’ is approximately taken to be equal to the ‘particle size’ [230]. But any individual grain or particle in a sample (whether it is nanocrystalline or else), always contain quite a few number of crystallites and therefore the information extracted from **Eq. 6** about the ‘particle size’ will always be less than the ‘actual’ particle size.

As we have observed marked differences of the particle size, measured directly from TEM image and as determined indirectly from X-ray diffraction peak broadening, particularly for films deposited with higher deposition times ($t_a = 15$ min and 45 min), we suppose that larger particles (as observed by TEM) might consist of a number of smaller crystallites and in that sense, larger particles are not single crystalline.

Selected area electron diffraction pattern (SAED) of the films deposited in 3 min, 9 min and 15 min are shown in the insets of **Fig. 50(a), (b)** and **(c)**. Few diffraction rings are obtained in all the patterns which correspond to the (101) & (202) planes of the films deposited in 3 min, (101) & $(00\bar{1}2)$ for the films with $t_d = 9$ min and (101) & (018) for the films deposited in 15 min respectively. The lattice spacings (d) corresponding to these rings in the diffraction patterns were measured with the camera constant of the equipment and the diffraction ring radii were measured from the micrographs [257]. These ‘ d ’-values calculated from all the patterns along with that obtained from XRD measurements were then matched with the theoretical ‘ d ’-values obtained from JCPDS file [113] and compared in **Table 22**. It has been observed that in all the SAED patterns, a (101) orientation is present, which is similar to the target material (c.f. **Fig. 7**) as well as to that of the film deposited for 15 min (as shown in the XRD pattern of **Fig. 48**; curve-#1). Therefore, this observation basically indicates the formation of quasi-continuous films consisting of CuAlO_2 nano-particles, when the deposition time is 15 min or less, (as has been depicted from TEM micrographs shown in

Fig. 50a, b and c), whereas with further increase in the deposition time (i.e. for $t_d \geq 45$ min), the growth mechanism followed a preferred (006) orientation.

Table 22. Comparison between the experimentally obtained d-values from SAED patterns (d_{SAED}) of the nano-crystalline CuAlO_2 thin films deposited for 3 min and 9 min and that of XRD patterns (d_{XRD}) for the films deposited for 15 min and 45 min respectively with that given in JCPDS file (d_{JCPDS}).

h k l	d_{SAED} (Å)			d_{XRD} (Å)		d_{JCPDS} (Å)
	$t_d = 3$ min	$t_d = 9$ min	$t_d = 15$ min	$t_d = 15$ min	$t_d = 45$ min	
0 0 6	---	---	---	---	2.816	2.820
1 0 1	2.438	2.441	2.450	2.448	2.450	2.437
0 1 2	---	---	---	2.350	2.380	2.376
1 0 7	---	---	---	1.732	---	1.732
0 1 8	---	---	1.618	1.607	1.610	1.612
0 0 $\bar{1}$ 2	---	1.406	---	---	---	1.401
2 0 2	1.220	---	---	---	---	1.225

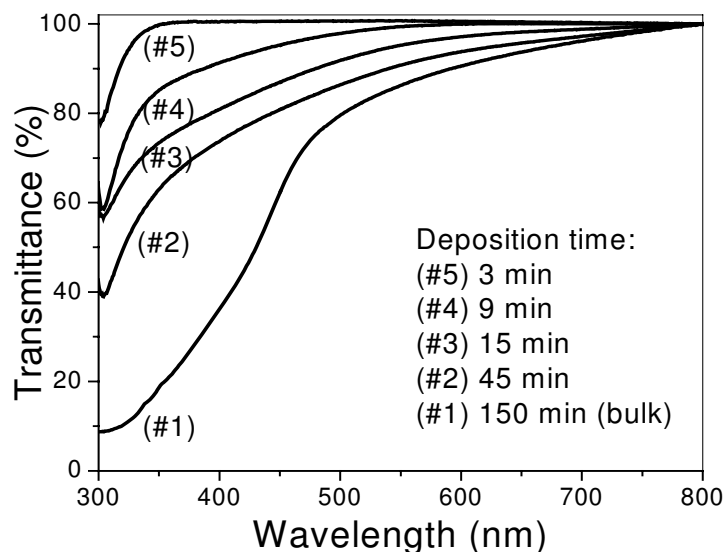


Figure 51(a). Optical transmission spectra of nanocrystalline CuAlO_2 thin films.

Optical properties: UV-Vis spectrophotometric measurements of CuAlO_2 thin films were done for the samples with deposition times 3 min, 9 min, 15 min, 45 min and 150 min. Fig. 51(a) shows the transmittance (T) vs. wavelength graphs of these films deposited on glass substrates taking similar glass as reference. Therefore the spectra are for the films only. Thickness of the films are in the range of 30 nm, 60 nm, 90 nm, 200 nm and 400 nm for the films deposited in 3 min, 9 min, 15 min, 45 min and 150 min respectively. The average visible transmittance of these films increases from 75 % to 98 % with decrease in the deposition time. This is mainly due to the decrease in the film thickness, which leads to lesser

scattering and absorption of photons. **Fig. 51(b)** represents the spectral variation of reflectance (R) of the same films deposited on glass substrates. From the transmittance (T) and reflectance (R) data, the absorption coefficients (α) of these films were measured according to the **Eq. 16**. **Fig. 52** represents the spectral variation of α in the visible range. The value of α varies from $8.61 \times 10^2 \text{ cm}^{-1}$ for film deposited for 3 min to $2.56 \times 10^4 \text{ cm}^{-1}$ for film deposited for 150 min (bulk film)

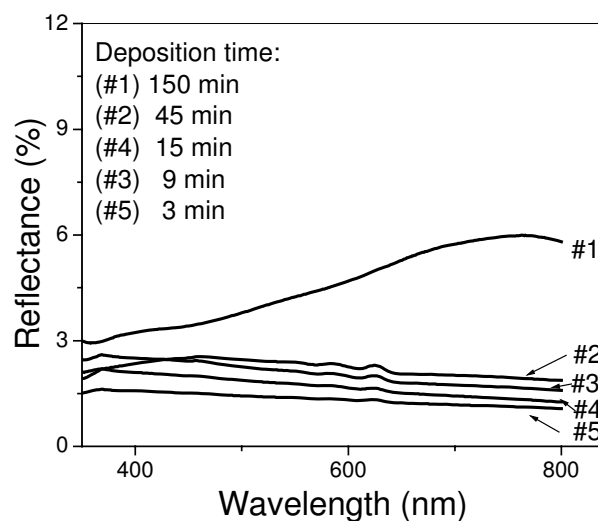


Figure 51(b). Spectral variation of reflectance of the nanocrystalline CuAlO_2 films.

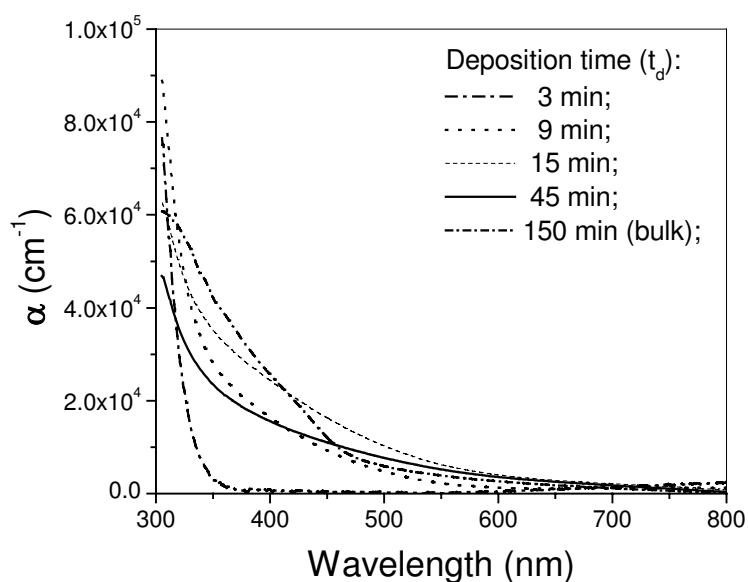


Figure 52. Variations of α with wavelength for nanocrystalline CuAlO_2 thin films for various deposition times (t_d) and thickness (d).

at 400 nm wavelength. Also the refractive indices (n) and extinction coefficients (k) of these films were determined according to **Eq. 15** and **14** respectively using the values of α and R . **Fig. 53(a)** and **(b)** show the wavelength vs. n and k plots respectively. Various optical parameters of nanocrystalline CuAlO_2 films deposited for different times are compared in **Table 23**.

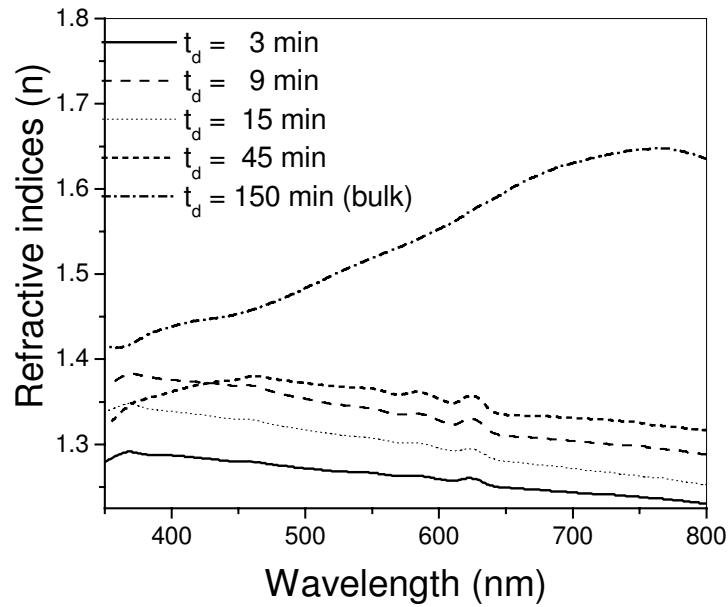


Figure 53(a). Dispersion of refractive indices of nanocrystalline CuAlO_2 thin films.

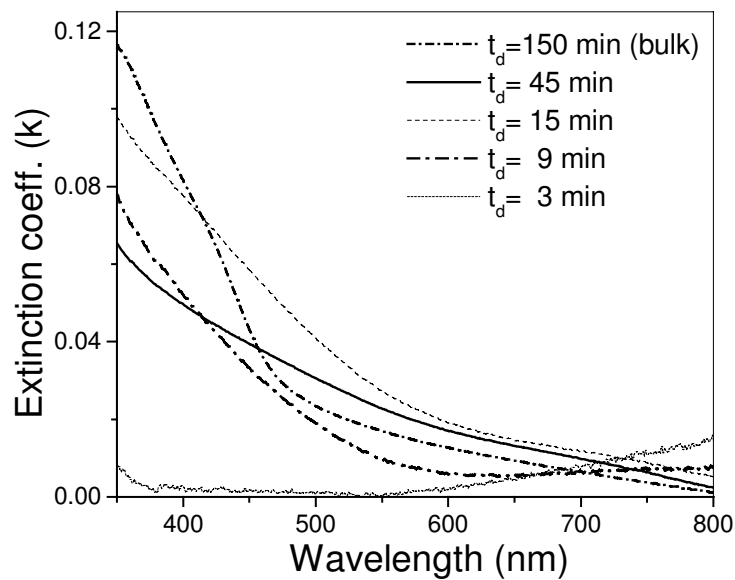


Figure 53(b). Spectral variation of extinction coeff. (k) of nanocrystalline CuAlO_2 thin films.

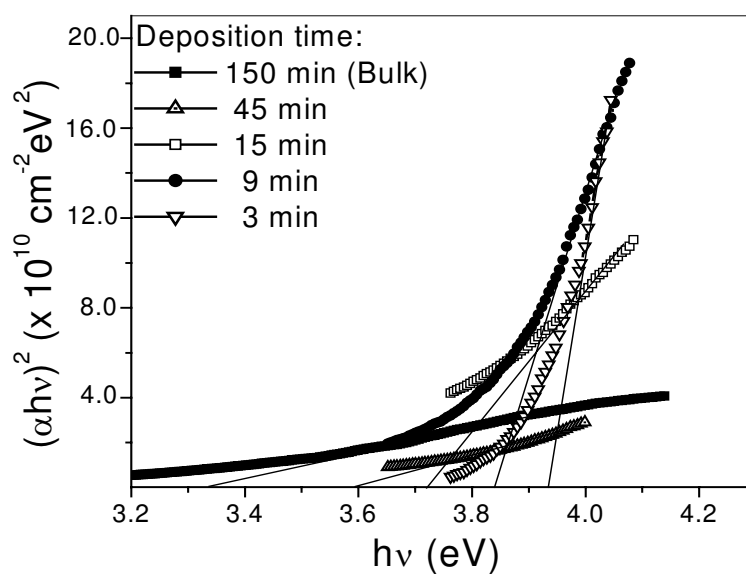


Figure 54. Determination of direct bandgaps of nanocrystalline CuAlO_2 thin film with different deposition times.

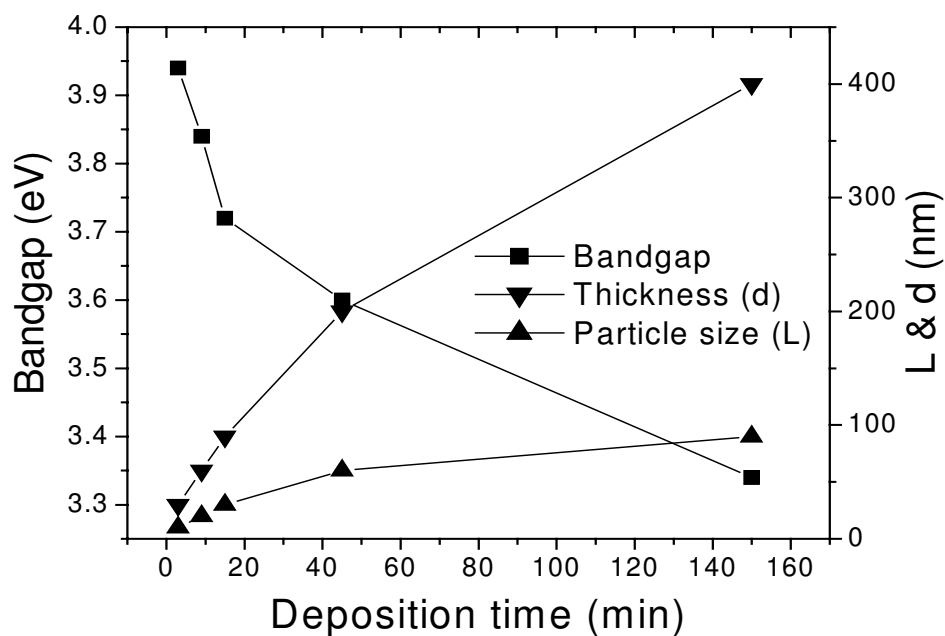


Figure 55. Variation of bandgap, particle size and thickness with deposition time.

In the range of the onset of absorption edge, the absorption coefficients (α) can be described by the relation for parabolic bands according to **Eq. 17**. The $(\alpha h\nu)^2$ vs. $h\nu$ plots for the films with different deposition times (t_d) is shown in **Fig. 54**. The direct allowed bandgap values for the films deposited for 3 min, 9 min, 15 min, 45 min and 150 min are

obtained as 3.94 eV, 3.84 eV, 3.72 eV, 3.60 eV and 3.34 eV respectively. The corresponding average particle sizes (L) are 10 nm, 20 nm, 30 nm, 60 nm and greater than 90 nm respectively. The variation of bandgaps, particle size and film thickness with deposition time is shown in **Fig. 55**. Previously, Kawazoe and co-authors [64] reported the direct allowed bandgap of their pulsed laser deposited CuAlO_2 thin film around 3.5 eV with an average visible transmittance $\sim 60\%$. But as far as nanocrystalline CuAlO_2 thin films are concerned, Gong and co-authors [150] obtained the direct bandgap of their nanocrystalline Cu-Al-O films as 3.75 eV with an average visible transmittance $\sim 35\%$. This bandgap value is comparable to our films (3.72 eV) with deposition time 15 min. But the average visible transmittance of our sample is quite higher ($\sim 80\%$) than that of Gong and co-authors ($\sim 35\%$). This is mainly due to the presence of impurity (Cu_2O) in their sample as well as higher thickness (250 nm) of these films than ours (90 nm), leading to the scattering and absorption of photons. On the other hand Gao et al. [154] obtained the direct bandgap and average visible transmittance of their nanocrystalline CuAlO_2 thin film as 3.75 eV and 60% respectively, which is nearly comparable to our values. From **Fig. 55**, we have observed the broadening of the bandgap energy of our nanocrystalline CuAlO_2 thin film with the decrease in the deposition time. This may be attributed to the quantum confinement effect put forward by Brus [69] where the size dependency of the bandgap of a semiconductor nanoparticle ($E_{g[nano]}$) is given by the following formula:

$$\Delta E = E_{g[nano]} - E_{g[bulk]} = \frac{h^2}{8\mu^* \left(\frac{L}{2}\right)^2} - \frac{1.8e^2}{\left(\frac{L}{2}\right)\epsilon} \quad (24)$$

where ΔE is the shift of the bandgap with respect to the bulk bandgap $E_{g[bulk]}$, $\frac{L}{2}$ is the radius of the nano-particles (where L is the particle diameter, taken to be equivalent to the particle size, mentioned earlier), μ^* is the reduced mass of electron-hole effective masses and ϵ is the semiconductor dielectric constant. The first term of the RHS expression in the equation represents the particle-in-a box quantum localization energy and has an $\frac{1}{L^2}$ dependence for both electron and hole. The 2nd term represents the Coulomb energy with an $\frac{1}{L}$ dependence. In the limit of large L , the value of $E_{g[nano]}$ approaches that of $E_{g[bulk]}$. As TEM micrographs (**Fig. 50a, b and c**) reveal that the average particle size of our samples decreases with the decrease in the deposition time (i.e. $L \sim 10$ nm and ~ 20 nm for $t_d = 3$ min & 9 min respectively and for $t_d = 15$ min and 45 min, $L \sim 30$ nm and ~ 60 nm, c.f. **Table 23**), the observation of bandgap widening in our samples is consistent with the quantum confinement effect explained by the **Eq. 24**. Previously, Gong et al [150] observed similar bandgap widening of their nanocrystalline Cu-Al-O films from bulk material and explained it in terms of the exciton confinement in semiconductor nanocrystals, which produces discrete, excited electronic states having higher oscillator strength and bandgaps as

an inverse function of crystallite size [72, 258] The same group also observed a blue-shift of the bandgap of co-sputter-deposited Cu-Al-O films with a variation in the Cu : Al atomic ratio in their sample [146], but whether this was due to the size-dependant bandgap widening of semiconductor nanoparticles is not quite clear for their multiphase (a mixture of CuO and CuAlO_2) samples.

Table 23. Variation of average particle size, film thickness and bandgap with the deposition time of nano-crystalline CuAlO_2 thin film.

t_d	Average particle size	Film thickness	Avg. T	α (at $\lambda=400$ nm)	n (at $\lambda=400$ nm)	k (at $\lambda=400$ nm)	Band-gap (eV)
(min)	(nm)	(nm)	(%)	(cm^{-1})			
3	~ 10	30	95	8.61×10^2	1.29	0.003	3.94
9	~ 20	60	90	1.63×10^4	1.38	0.05	3.84
15	~ 30	90	80	2.44×10^4	1.34	0.08	3.72
45	~ 60	200	75	1.56×10^4	1.36	0.05	3.60
150 (bulk)	> 90	400	65	2.56×10^4	1.44	0.08	3.34

To examine the size-dependant optical properties of CuAlO_2 nanoparticles, the photoluminescence (PL) spectroscopic measurements were also performed at room temperature. The PL spectra shown in **Fig. 56** were obtained with a 210 nm excitation wavelength and the films were deposited on Si substrates. Three spectra shown in the **Fig. 56** are for three samples deposited for 9 min (curve – a), 15 min (curve – b) and 45 min (curve – c) respectively. Three peaks obtained are around 3.56 eV, for curve – c ($\lambda = 348.5$ nm), 3.61 eV, for curve – b ($\lambda = 343.6$ nm) and 3.66 eV, for curve – a ($\lambda = 339.0$ nm) respectively. These peaks may be attributed to the UV near-band edge (NBE) emission [252] of wide bandgap CuAlO_2 , namely the recombination of free excitons through an exciton-exciton collision process. This observation again indicates the existence of direct transition type bandgap of this material, which is favorable for the optoelectronics applications like light-emitting diodes (LED). It is also note-worthy that, like other widegap semiconductors such as ZnO and LaO(CuS), where excitons can be observed at room temperature, the excitons in CuAlO_2 are supposed to have large binding energy (E_b). Although the exact value of the binding energy is not known yet, but the above argument seems reasonable if we get an indirect estimation of the binding energy by the following relation (assuming hydrogen-like model) [123]

$$E_b = \left(\frac{\mu}{m_O \epsilon_r^2} \right) \times 13.6 \text{ eV} \quad (25)$$

with

$$\frac{1}{\mu} = \frac{1}{m_e^*} + \frac{1}{m_h^*} \quad (26)$$

where μ , m_O , ϵ_r , m_e^* and m_h^* denote reduced mass, free electron mass, relative dielectric constant, effective masses of electrons and holes respectively. According to **Eq. 25**, large exciton binding energy would result from a small relative dielectric constant (ϵ_r) and a high-reduced mass (μ) of the excitons. The relative dielectric constants (ϵ_r) of CuAlO₂ thin film is estimated from the reflectance data (**Fig. 51b**), which fall within the range of 1.7 to 3.5, for the films deposited in 9 min, 15 min and 45 min respectively. These values are less than that of LaO(CuS) and ZnO [123, 259]. Therefore the reduced mass in CuAlO₂ may be considered to be large enough to generate room-temperature excitons. As has been suggested that the layered-crystal structure is responsible for the stability of excitons in LaO(CuS) [123], following similar argument, it may be considered that the super-lattice structure of CuAlO₂ [93-95] is responsible for the large reduced mass of the excitons, which, in turn, produces large binding energy to generate room temperature excitons in this material. Also, a slight blue-shift of the emission peaks are observed with decrease in the deposition time. As already mentioned previously, that a decrease in the average particle size (L) is observed with the decrease in the deposition time, t_d (i.e. for $t_d = 9$ min, 15 min and 45 min, $L \sim 20$ nm, ~ 30 nm and ~ 60 nm respectively), therefore this blue-shift may be another indication of experimentally observed bandgap enhancement results from low-dimensional quantum confinement effects.

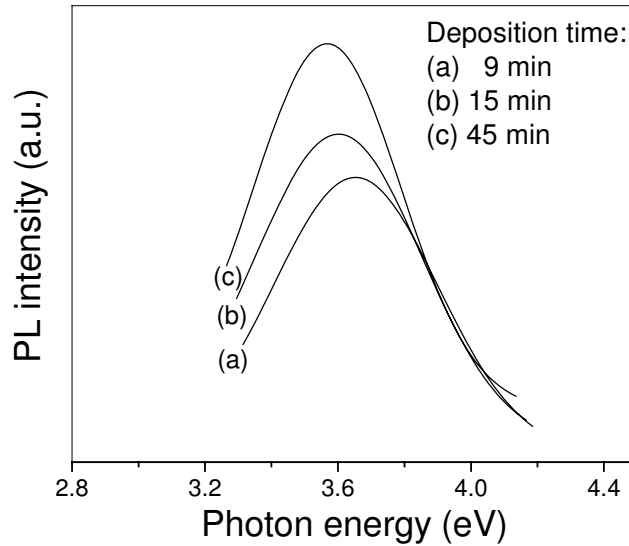


Figure 56. Photoluminescence spectra (PL) spectra of nano-structured CuAlO₂ thin films deposited for (a) 9 min, (b) 15 min and (c) 45 min.

To justify further whether quantum confinement is the most likely explanation for the observed blue-shift of the bandgap of our nano-structured CuAlO₂ thin films, we have tried to fit **Eq. 24** with reasonable values of μ and ϵ and the fit was satisfactory (within 5 % of the experimental value). On the other hand, forcing 100 % matching with **Eq. 24** and our data, we

have obtained an estimation of effective excitonic mass (μ) around $0.03 m_0$ (m_0 is the free electron mass), which appears reasonable. However, as so far there is no published data of effective masses of carriers of this material, hence, we cannot claim that the agreement is very accurate. But in another way we have indirectly estimated the value of μ from **Eq. 25**: As we have seen from photoluminescence measurements (**Fig. 56**) that our nanostructured CuAlO_2 films show exciton absorption at room temperature (300 K), therefore the binding energy (E_b) of excitons must exceed the thermal energy of $k_B T_{(T=300\text{ K})} = 26\text{ meV}$. So, putting E_b approximately around 30 meV in **Eq. 25** and the value of \mathcal{E}_r as 3.5, obtained from reflectance data (**Fig. 51b**), (this value is comparable to that of other p-type TCO like LaOCuS , which is ~ 4.0 [123] as stated earlier), the value of μ comes out as $0.03 m_0$. This value agrees with the previous one. So we can say that the quantum confinement effect is the most likely explanation for the bandgap widening of our nanostructured CuAlO_2 thin films.

Also we have observed slight decrease in the intensities of the peaks with decrease in the particle size. This may be due to the presence of some surface states in our nanostructured material. It is well known that the surface states may seriously influence the PL efficiency in nano-materials due to the high surface-to-volume ratio [260]. Larger the particle size, lesser will be the surface-to-volume ratio and therefore smaller will be the effect of surface states on PL intensity. That is why we have observed an increase in the PL intensity with the increase in the particle size as shown in **Fig. 56**. It must be mentioned here that as there are no reports on the photoluminescence properties of CuAlO_2 thin films (as literature survey depicts), therefore the exact mechanism of the different possible transitions is yet to be explored completely and intense research is needed in this direction to explore proper emission mechanism.

Hall measurements could not be performed in all of our samples. But p-type conductivity of the sample deposited for 150 min was established by thermo-power measurement and the positive value of room temperature Seebeck coefficient ($S_{RT} = +93\ \mu\text{V K}^{-1}$) of this sample confirmed the p-type *nature* of the film. But for the films deposited for 45 min and less, thermo-power measurement could not be performed and only hot-probe measurements confirmed the p-type conductivity in these films.

8. Field-Emission Properties of CuAlO_2 Thin Films

Low-macroscopic field (LMF) emission of electrons from the surface of a thin film to the vacuum in the presence of a macroscopic electric field (mean field between the parallel plates in a capacitor configuration) is currently of much interest due to the potential applications in cold cathode devices.

Here we have discussed the field-emission properties of CuAlO_2 thin film synthesized by both D.C. and reactive sputtering, and discussed in details the emission mechanism. As CuAlO_2 is a wide bandgap p-type semiconducting material, its field-emission properties may give an additional impetus on the properties of this technologically important material and may open-up a new window in the field-emission technology with a new group of materials other than carbon-based films.

8.1. Description of Apparatus

Field emission measurements were carried out by using a diode configuration consisting of a cathode (the film under test) and a stainless steel tip anode (conical shape with a 1 mm tip diameter) mounted in a liquid nitrogen trapped rotary-diffusion vacuum chamber with appropriate chamber baking arrangement. The measurements were performed at a base pressure of $\sim 7 \times 10^{-7}$ mbar. As the substrate glass was non-conducting, the negative terminal of the high voltage D. C. power supply (range is 0 to 5 kV) was connected with the films by silver paint, at least 6 mm away from the position of the anode tip. The Ohmic *nature* of the contact was checked before field emission experiment. The sheet resistance of our film was few hundred kilo-ohms/ \square and the maximum emission current measured, was almost 30 μ A. So, during emission process, if there was any voltage drop occurred between the contact and the portion of the sample just under the anode tip, it would be at the most, of the order of few volts, which was quite small compared to the applied voltages (\sim kV). Hence we neglected this drop and all the calculations were done with the applied voltages. The tip-sample distance was continuously adjustable to a few hundred μ m by spherometric arrangement with a screw-pitch of 10 μ m. The tip was first touched to the sample surface and then raised by a controlled amount according to the spherometer-scale attached to the anode. The macroscopic field is calculated from the external voltage applied (V), divided by the anode-sample spacing, d (obtained from spherometric arrangement). The current was measured by Keithley electrometer (model 6514), whose current detection range is 100 nA to 21 mA. A current limit of 1 mA was set to avoid destruction of the films from excessive current flow. The whole surface of the film was visible through the chamber view-port, which enabled us to recognize the electron emission and discharge. It was confirmed that no discharge was taking place between the anode and the sample, so the current detected, was entirely due to cold field-emission process. The schematic diagram of the field-emission apparatus was shown previously [207].

8.2. Field-Emission Properties

Fig. 57 and **Fig. 58** show the emission current (I) vs. macroscopic field (E) curves of D. C. sputtered CuAlO₂ thin film (post-annealed for 60 min) and reactive sputtered CuAlO₂ thin film (post-annealed for 60 min) respectively Both the films were deposited on glass substrates and the anode-sample separations (d) were 100, 140 and 200 μ m respectively for both the films. As obvious, it has been observed that in both cases, the

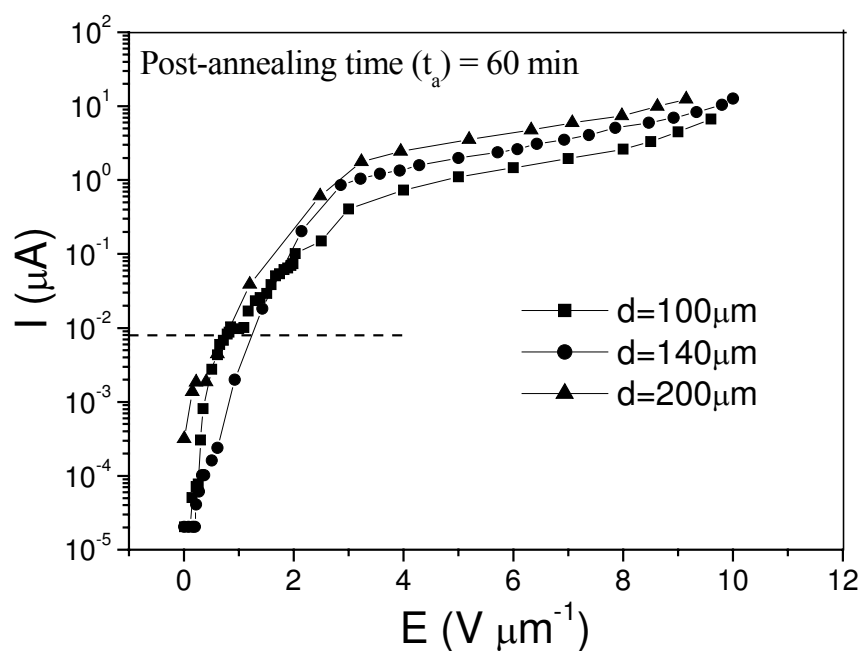


Figure 57. Emission current (I) vs. macroscopic field (E) curves for D. C. sputtered CuAlO_2 thin films post-annealed for 60 min, for different anode-sample (d) spacing.

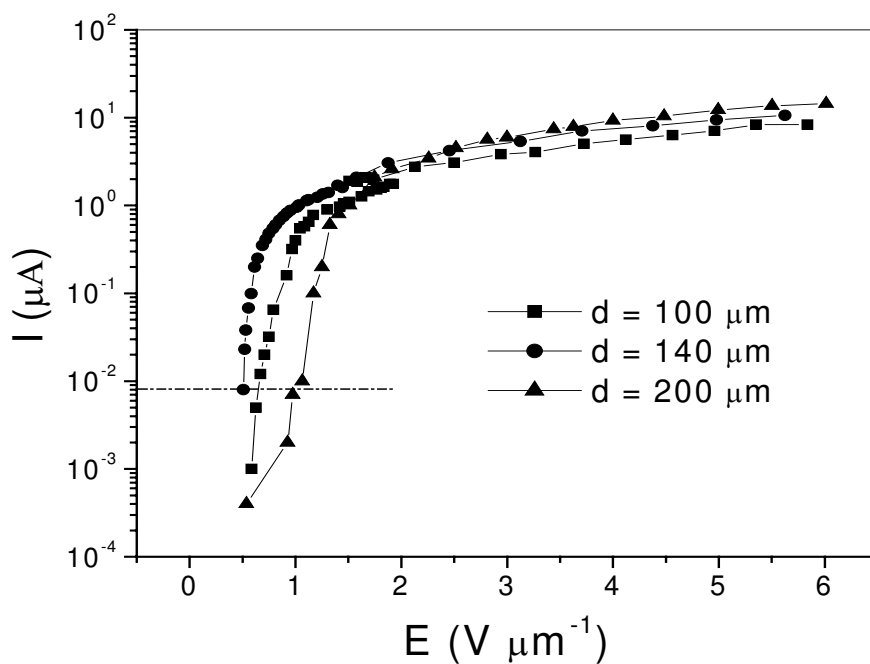


Figure 58. I-E curves for reactive sputtered CuAlO_2 thin film.

curves are almost identical in *nature*. The macroscopic field is calculated from the external voltage applied (V), divided by the anode-sample spacing, d (obtained from spherometric arrangement in the field-emission apparatus).

Theoretically, the emission current I is related to the macroscopic field E by

$$I = A a t_F^{-2} \phi^{-1} (\beta E)^2 \exp\left\{-\frac{b v_F \phi^{3/2}}{\beta E}\right\} \quad (27)$$

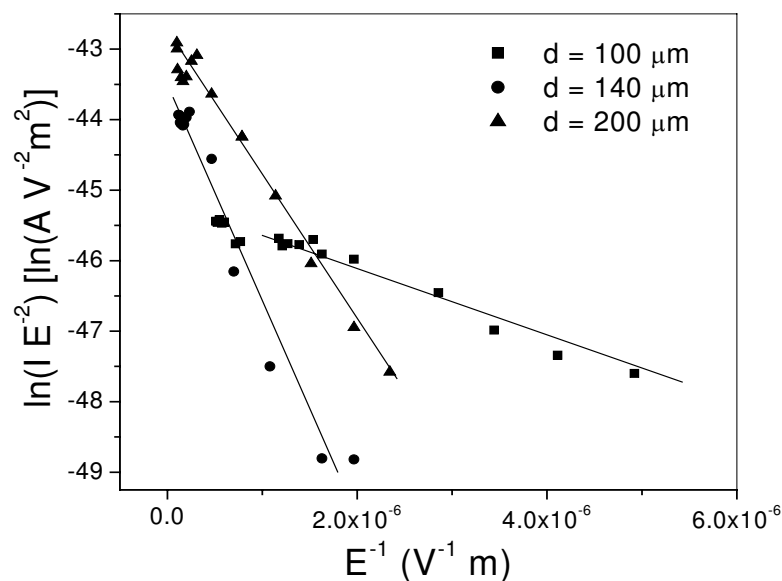
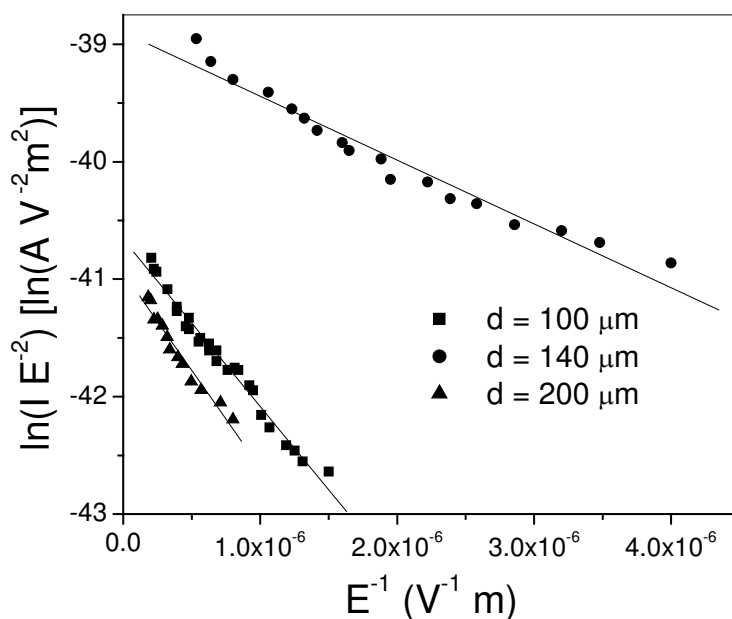
where, ϕ is the local work-function, β is the field enhancement factor discussed earlier, A is the effective emission area, a is the First F-N Constant ($= 1.541434 \times 10^{-6} \text{ A eV V}^{-2}$), b is the Second F-N Constant ($= 6.830890 \times 10^9 \text{ eV}^{-3/2} \text{ V m}^{-1}$), and v_F and t_F are the values of the special field emission elliptic functions v and t [210], evaluated for a barrier height ϕ . In so-called Fowler-Nordheim coordinates, this equation takes the form:

$$\ln\left\{\frac{I}{E^2}\right\} = \ln\{t_F^{-2} A a \phi^{-1} \beta^2\} - \frac{(v_F b \phi^{3/2} \beta^{-1})}{E} \quad (28)$$

An experimental F-N plot is modified by the tangent to this curve, taken in the mid-range of the experimental data. This tangent can be written in the form [261, 262]:

$$\ln\left\{\frac{I}{E^2}\right\} = \ln\{r A a \phi^{-1} \beta^2\} - \frac{(s b \phi^{3/2} \beta^{-1})}{E} \quad (29)$$

where r and s are appropriate values of the intercept and slope correction factors, respectively. Typically, s is of the order of unity, but r may be of order 100 or greater. Both r and s are relatively slowly varying functions of 1/E, so an F-N plot (plotted as a function of 1/E) is expected to be a good straight line. The F-N plots of our samples are shown in **Fig. 59** and **Fig. 60**, for the D. C. sputtered and reactive sputtered films respectively. It has been observed that all the I-E curves in the present work are closely fitted with straight lines. This suggests that the electrons are emitted by cold field emission process. The turn-on field, which we define as the macroscopic field needed to get an emission current $I = 8.0 \times 10^{-3} \mu\text{A}$ [cf. **Fig. 57** and **58**], (which corresponds to an estimated macroscopic current density, $J_{\text{est}} = 1 \mu\text{A}/\text{cm}^2$, where $J_{\text{est}} = I/A$, A = anode-tip area) was found at and around 0.5 to 1.2 V/ μm for both the D. C. sputtered and reactive sputtered films. These values are comparable to the conventional low-threshold field emitters like carbon nano-fibres ($\sim 1.1 \text{ V}/\mu\text{m}$) [86] but quite lower than that of amorphous carbon and DLC films (8 – 20 V/ μm), diamond films (5 – 15 V/ μm) [82, 85, 263-267], Si-C nanorods (13 – 20 V/ μm) [87] etc. It is worthwhile to mention that the definition of the turn-on field is not universal. For carbonaceous emitters like a: C, DLC,

Figure 59. F-N plots of D. C. sputtered CuAlO_2 thin film.Figure 60. F-N plots of reactive D. C. sputtered CuAlO_2 thin film.

diamond etc., some authors [80, 265] had defined it as the field for which the macroscopic current density is $1\mu\text{A}/\text{cm}^2$. But Hirakuri et al. [82] considered this value as $0.01\mu\text{A}/\text{cm}^2$, whereas Robertson [263] had chosen this at $0.1\mu\text{A}/\text{cm}^2$. But for carbon nano-fibres and Si-C nanorods, as the maximum emission current is quite large, the turn-on field is defined at a higher macroscopic current density of the order of $10\mu\text{A}/\text{cm}^2$ [86, 87] to as large as 10

mA/cm^2 [268]. In both the I- E curves (**Fig. 57** and **58**), we have observed a parallel-shift of the curves w. r. t. anode-sample separation (d), but the *nature* of the curves is identical, i.e. a slight increase in the current with the increase in the anode-sample separation, at a given field, has been observed. For example, in **Fig. 57**, at a field of $4 \text{ V}/\mu\text{m}$, the I-values were found to be $2.5 \mu\text{A}$ [for $d = 200 \mu\text{m}$], $1.5 \mu\text{A}$ [for $d = 140 \mu\text{m}$] and $0.8 \mu\text{A}$ [for $d = 100 \mu\text{m}$] respectively. Similarly, in **Fig. 58**, at a field of $4 \text{ V}/\mu\text{m}$, the I-values were found to be $10.3 \mu\text{A}$ [for $d = 200 \mu\text{m}$], $7.6 \mu\text{A}$ [for $d = 140 \mu\text{m}$] and $5.1 \mu\text{A}$ [for $d = 100 \mu\text{m}$] respectively. Similar observation was also reported by Zhou et al. [87], for their β -SiC nanorods. Although they have not given any reason for that, but we suppose that this type of shift observed for our sample, was probably due to the change in the effective emission area of the sample. And this change in the effective emission area w. r. t. 'd', might be related to the geometry of the anode. As mentioned earlier, the anode in our experiment is conical in shape with a tip diameter of 1 mm , therefore the lines of force emanating from the edge of the anode-tip, and terminating to the sample surface, are diverging in *nature*, whereas the lines of force emanating from the flat surface of the tip are parallel in *nature* (neglecting the small surface undulations of the highly polished anode-tip). Hence, the effective emission area of the sample becomes an increasing function of the anode-sample separation, 'd', as described schematically in **Fig. 61(a)**. It seems reasonable to consider this argument as a valid one, if we compare this with the experimental findings of Okano et al. [269] and Gröning et al. [270] for their diamond and DLC films respectively. Okano et al. [269] reported that their macroscopic current density was independent of the anode-sample separation. This might be related to the basic constructional differences between their field-emission apparatus and ours. Their field-emission apparatus consisted of a parallel plate arrangement of the anode and the sample, separated by spacers, as shown in **Fig. 61(b)**. So the electric lines of force between the anode and the sample were more or less parallel in *nature*; hence the effective emission area remained independent of the anode-sample spacing. On the other

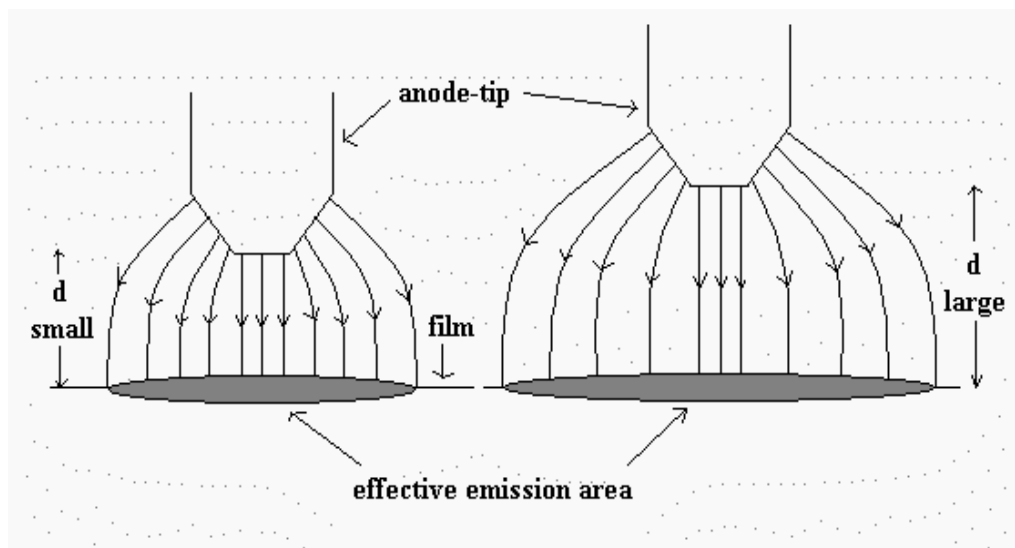


Figure 61(a). Schematic diagram of dependence of effective emission area as an increasing function of anode-sample separation, d . The sketch is not exactly to the scale.

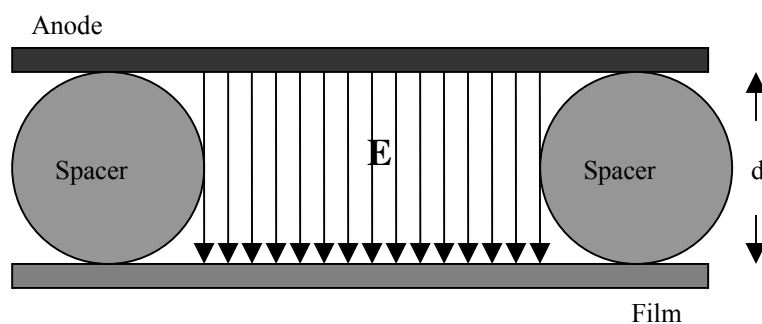


Figure 61(b). Schematic diagram of parallel plate configuration of field-emission apparatus. The sketch is not exactly to the scale.

hand, Gröning et al. [270] used a spherical stainless steel anode-tip in their field-emission apparatus. Hence, lines of force between the anode-tip and the sample in their experiment were diverging in *nature*. They observed a parallel shift in the $I - E$ curves for their sample before and after raising the field to $50 \text{ V}/\mu\text{m}$ for 1 hour of operation, keeping the anode-sample separation fixed. They argued that this parallel shift was due to the increase in the emission area of the sample and this area-enhancement was the result of the morphological changes occurred in the film during operation. Following this point of view, to see whether the area-increment in our samples is due to any morphological changes in the films or not, we have done the experiment in both ways: firstly, with increasing anode-sample spacing and secondly, with decreasing anode-sample spacing. But in both cases similar types of shifts in the $I - E$ curves were observed, indicating no (or almost negligible) morphological changes occurred in the film during operation. So our argument, that in our experimental set-up, the effective emission area of the sample becomes an increasing function of the anode-sample separation, is justified.

According to **Eq. 29**, the slope of the tangent would carry the information of the local work function (ϕ) of the emitter-tip. Assuming an ideal flat emitter with field enhancement factor (β) equal to 1, we have obtained an estimation of the values of ϕ from the F-N plots (**Fig. 59** and **60**) to lie between 1.68×10^{-3} and 5.84×10^{-3} eV for D. C. sputtered films and 1.85×10^{-3} to 4.0×10^{-3} for reactive sputtered films. But the true local work function must be much larger than these values, due to the factor, β , which depends on the shape of the emitter. Forbes et al. [271] determined its value via the ‘hemisphere on a post approximation’ (**Fig. 62**) as:

$$\beta \approx \frac{0.7L}{R} \quad (30)$$

within the range $30 \leq L/R \leq 2000$. (where, L = height of the post, and R = radius of the hemisphere). Some comments on various models for the determination of field enhancement factor are given in Ref. [271]. In the previous section [cf. **Section 5**, **Table 14**], we have furnished the particle size of both D. C. sputtered and reactive sputtered

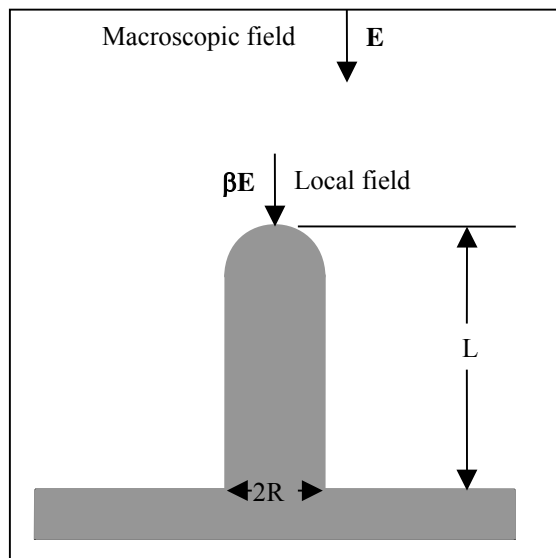


Figure 62. ‘Hemisphere on a post’ model. Macroscopic field, E , enhanced by a factor, β , determined by the height of the post, L , and radius of the hemisphere, R (Ref. [271]).

CuAlO_2 thin films as low as 26 nm and 32 nm respectively, obtained from XRD data, whereas the film thicknesses were around 0.5 μm , obtained from cross-sectional SEM. The nanometric particle sizes of our films are also justified from the SEM and TEM micrographs of the films shown in **Fig. 63(a)** and **63(b)** respectively. SEM image (**Fig. 63a**) of reactive sputtered film depicts a smooth surface of the films, indicating very small particle size, beyond the resolution of the SEM used. On the other hand, TEM micrograph (**Fig. 63b**) of the same indicates some cluster formation with particle size roughly around 30 to 40 nm (SEM and TEM images of D. C. sputtered films are almost identical in *nature*, and hence not shown here). So the emission tip radius (R) of our sample would be of the order of few nanometers (considering the sharp emission tip radii are almost 10 % of the particle size) and assuming the height of the post (L) is equal to the film thickness, the approximate β -value obtained for our samples was around 180. This value of β falls within the range (150 – 300) predicted by Gröning et al. [270], for their N-doped DLC films and they stated that this sort of β -values was not unusual even on mirror like polished copper samples. So the local work functions increased by almost two orders of magnitude, and come out in the order of 0.15 eV to 0.2 eV. But still these are approximate values and quite less than the work function of the bulk material, especially for a wide bandgap, p-type semiconductor like CuAlO_2 , as shown schematically in **Fig. 64(a)**. So these small values of ϕ may be treated as some barrier potential (barrier height, H , before Schottky lowering), which would give an estimation of the electron affinity, χ , of the material, depending on the mode of emission [213]. Although, the mechanism of the electron emission from this material is still not quite clear, but the low value of barrier height might be an indication of the dominant non-degenerate conduction-band emission, with an estimated electron affinity of the order of 0.2 eV. This low value of χ might be related to the wide bandgap of our film ($E_g = 3.7$ eV, for D. C. sputtered films and 3.9 eV for reactive sputtered films (cf. **Table 15**) respectively), as explained previously, by Robertson [81], for diamond films [212, 267], which is a p-type semiconductor having

considerable large bandgap ($E_g = 5.6$ eV). But for a p-type semiconducting material, this type of sustained conduction-band emission is unlikely, unless injection to the conduction band inside the film may take place. This injection may be related to the internal nanostructure of our material.

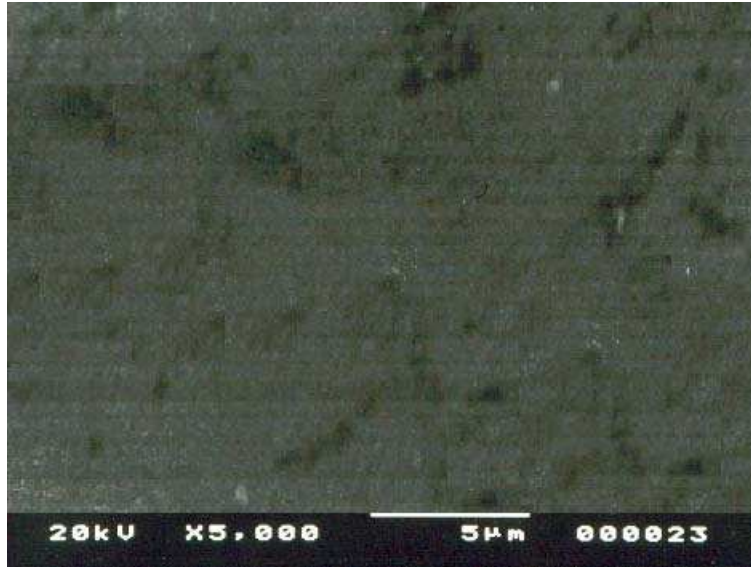


Figure 63(a). SEM micrograph of reactive sputtered CuAlO_2 thin film.

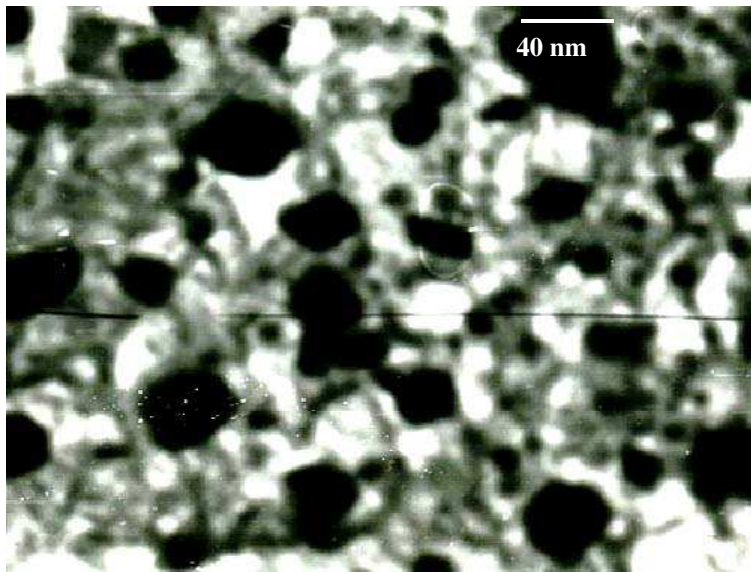


Figure 63(b). TEM micrograph of reactive sputtered CuAlO_2 thin film.

So, the 'ENH-material hypothesis', put forward by Forbes [213], that electrically nanostructured heterogeneous (ENH) materials with quasi-filamentary conducting channels inside a less conducting matrix, show low-macroscopic field emission, may be applicable to

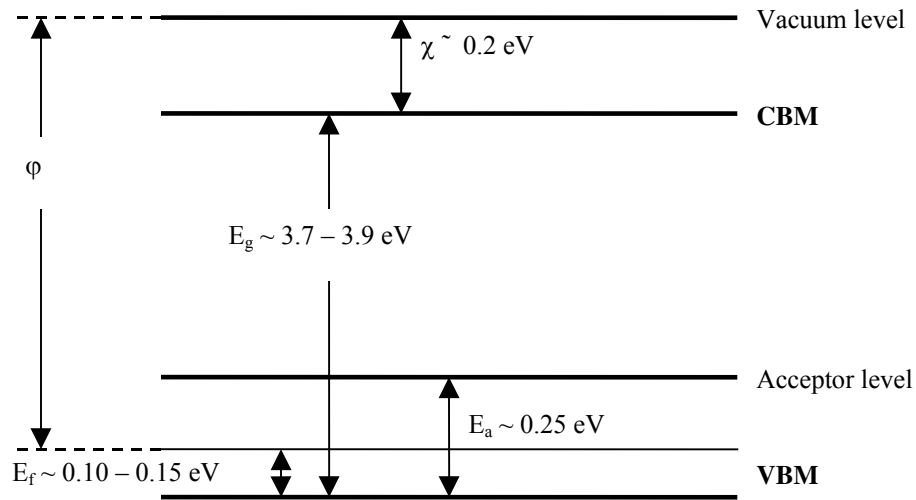


Figure 64(a). Schematic diagram of approximate energy level diagram of CuAlO_2 thin film. The energy levels are not exactly to the scale.

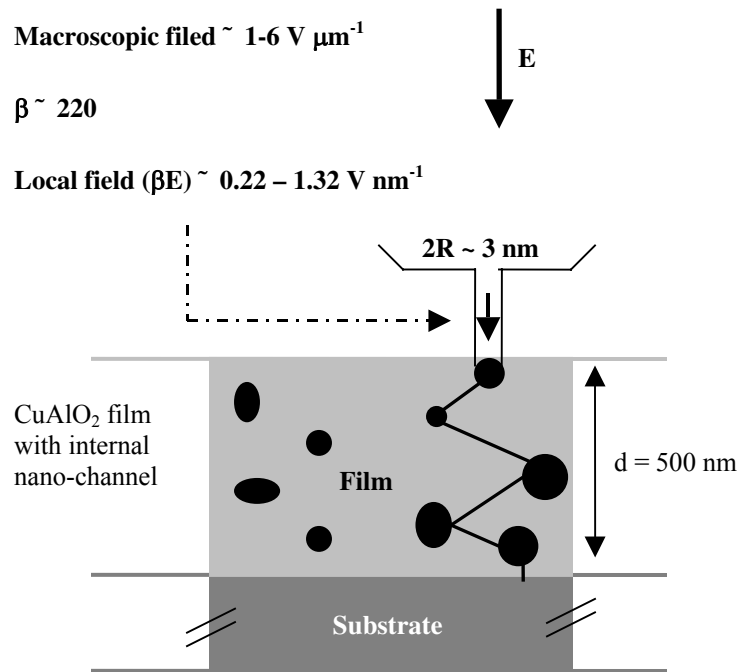


Figure 64 (b). Schematic diagram of ENH-model for CuAlO_2 film (After Ref.[213]).

our film also, as the particle size of our film was obtained around 30 to 40 nm with a film thickness of 500 nm (cf. **Fig. 63**). The mechanism is explained schematically in **Fig. 64(b)**, where the macroscopic field ($E \sim 1$ to $6 \text{ V}/\mu\text{m}$) is enhanced due to the field enhancement

factor ($\beta \sim 220$) by almost two to three orders of magnitude to produce large local field ($\beta E \sim 0.22$ to 1.32 V/nm) and thus provides necessary energy for electron tunneling. So, geometrical field enhancement inside as well as at the film / vacuum interface is assumed to be the primary cause of the low-threshold field emission of our films. It is also to be noted that, recently several transparent, wide bandgap oxide-based thin films have been reported to show good field emission properties such as ITO [198], SnO_2 [199, 272], ZnO [200-205, 273] etc. So these results are very important, interesting and encouraging in the sense that these wideband transparent semiconductors can become perfect alternative to the carbon-based films in the area of field-emission displays.

9. Conclusions

Polycrystalline, p-type semiconducting, transparent CuAlO_2 thin films were deposited by D. C. sputtering of sintered CuAlO_2 powder on Si and glass substrates successfully. The post-deposition oxygen annealing time (t_a) of the films was taken as a variable parameter (from 30 min to 150 min) to observe any change in the optical and electrical characteristics of the films. XRD spectrum confirms the polycrystalline *nature* of the films with small grain size (~ 26 nm). All the films were highly transparent in the visible region. Both allowed direct and indirect transitions were found to exist in the films. Corresponding direct band gap values were determined to be around 3.7 to 3.8 eV for all the films. P-type conductivity was confirmed from both thermoelectric power and Hall effect measurements. Sputtered-deposited transparent p-type semiconducting CuAlO_2 thin film showed fairly high conductivity with a maximum room temperature conductivity in the range of 0.39 S cm^{-1} and a carrier concentration $\sim 1.2 \times 10^{18} \text{ cm}^{-3}$, for the films with $t_a = 90$ min. It appears that, to some extent, post-deposition annealing of the film in oxygen atmosphere controls the p-type conductivity of the film. Compositional analyses reveal an increase in the excess oxygen content within the films with t_a upto 90 min. These values range from 0.5 at % (for $t_a = 30$ min) to 5.0 at % (for $t_a = 90$ min) over stoichiometric value, whereas room temperature conductivities (σ_{RT}) increase from 0.09 S cm^{-1} to 0.39 S cm^{-1} (for annealing times 30 to 90 min respectively). This suggests that excess oxygen, within the crystallite sites, may be inducing nonstoichiometry in the film, which, in turn, manifests the improved p-type conductivity of the CuAlO_2 thin film. Activation energies for these films range from 270 meV to 196 meV respectively. FT-IR spectra of the films indicated the existence of various bondings among Cu, Al and oxygen.

Thermo-power measurements indicate that CuAlO_2 may become a candidate material for thermoelectric conversion. CuAlO_2 has a natural superlattice structure, with an effective two-dimensional density of states (along ab-plane). This type of layered-structure material could become a good thermoelectric converter. Room temperature Seebeck coefficients (S_{RT}) are found to be +230, +141 and +120 $\mu\text{V K}^{-1}$ for $t_a = 90, 60$ and 30 min respectively, with $E_f = 130, 151$ and 200 meV respectively. An increase in S_{RT} with σ_{RT} is observed, which is expected for superlattice materials. Also, from band picture, it is observed that, higher the conductivity of the film, closer is its Fermi level to the upper edge of the valence band, which is obvious for a p-type material.

We have also successfully deposited polycrystalline p-type semiconducting CuAlO_2 thin films on glass and Si (400) substrates by reactive D. C. sputtering of a target, fabricated from

a stoichiometric mixture of Cu and Al metal powders. XRD spectrum confirmed the polycrystalline *nature* of the films with small grain size (~ 32 nm). The films were transparent in the visible region. Both allowed direct and indirect band gaps were found to exist and their corresponding values were 3.75 eV and 1.85 eV respectively. The p-type conductivity was confirmed by positive values of the Seebeck and Hall coefficients. The films showed fairly high room temperature conductivity of the order of 0.22 S cm^{-1} . The carrier concentration in the films was found to be $\sim 4.4 \times 10^{17} \text{ cm}^{-3}$. This is due to nonstoichiometric defect attributed to excess oxygen atmosphere introduced into the system during deposition. From EDX analyses, the composition of the film is found to be Cu: Al: O = 1: 1: 2.08, supporting the above argument. FT-IR spectra of the films indicated the existence of various bondings among Cu, Al and oxygen.

Wet-chemical synthesis of transparent copper aluminium oxide thin films has been performed successfully. XRD-pattern confirms the proper phase formation of the film with a strong (006) orientation. SEM micrograph shows existence of a smooth surface with some bigger clusters dispersed on the surface, which resulted due to the agglomeration of finer grains. Cross-sectional SEM reveals the thickness of the film around $\sim 1.5 \mu\text{m}$. Optical transmittance spectra depicts almost 90 % transparency of the film in the wavelength range of 500 nm to 800 nm, with a direct allowed bandgap of 3.98 eV. Hot-probe measurement confirms the p-type *nature* of the film.

The cost-effective fabrication of this technologically important material is extremely important for the large-scale production of device quality films. Low-cost physical routes like D.C. and reactive sputtering as well as chemical synthesis of p-CuAlO₂ thin films will enable fabrication of high quality films for diverse device applications.

All-TCO p-n hetero-junction diodes having the structure: n-ZnO: Al / p-CuAlO₂ have been successfully fabricated on glass substrates. The current-voltage characteristics of the all-transparent heterojunction diode shows the rectifying properties, indicating proper formation of the junction. Maximum current obtained at 5 V is around 1 μA and the turn-on voltage obtained as ~ 0.8 V. The forward bias current is greater than the reverse bias current by approximately a factor of ~ 30 at ± 4 V. The optical transmission spectra of the n-ZnO: Al / p-CuAlO₂ diode showed visible transparency around 60 %, indicating its potential applications in the field of 'Transparent Electronics'.

Nanostructured p-type conducting CuAlO₂ thin films have been synthesized by D. C. sputtering with deposition time as the variable parameter. It has been observed from TEM micrographs that for the films deposited with as low as 3 min, particle size is around 10 nm with a film thickness ~ 30 nm. With increase in the deposition time, an increase in the particle size is observed in the films, which is attributed to the agglomeration of smaller particles into bigger ones due to the greater time of exposure of these films into sputtering plasma. Optical transmission spectra of the films show an increase in the average visible transmittance with decrease in deposition time. For the film deposited for 3 min, the average visible transmittance is almost 99 %. This is mainly due to the smaller thickness of the film (~ 30 nm), which reduces the scattering and absorption of photons within the films. Also a blue-shift or widening of the bandgap of the material is observed with decrease in deposition time. As particle size decreases with decrease in the deposition time, this bandgap broadening is attributed to the quantum confinement effect, where the bandgap of a semiconductor nanoparticle becomes an inverse function of the particle size. Room temperature

photoluminescence measurements of this material showed UV bands around 3.56 eV to 3.66 eV for the films deposited for 45 min to 9 min respectively, which arises from the room temperature excitons. The existence of room-temperature excitons in CuAlO_2 is supposed to originate from low relative dielectric constant of the material and high reduced mass of the excitons, which produces large exciton binding energy. A blue-shift of the emission peaks is observed with decrease in the particle size, confirming the quantum confinement effect within the CuAlO_2 nanoparticles. The p-type conductivity of the films is confirmed by thermo-power as well as hot-probe measurements. This result of the synthesis of nano-crystalline p- CuAlO_2 (as well as other nanostructured p-TCO thin films, reported by various groups) will enable to fabricate nano-active devices which may give a new dimension in the field “Invisible Electronics”.

Transparent p- CuAlO_2 thin films prepared by D. C. and reactive sputtering have been investigated for its field emission properties. The anode-sample distance was varied from 100 to 200 μm . The film showed considerable low turn-on field between 0.5 – 1.2 $\text{V}/\mu\text{m}$. The F-N plots were found to be straight-line in *nature* which indicates that the electrons are emitted via cold-field emission mechanism. This low macroscopic field emission of the films may be attributed to the internal nanostructure of the films, which creates significant field enhancement inside as well as near the film-vacuum interface. Also secondary effect, such as, the presence of surface states creating field enhancement, may not be ruled out. This finding might open up a new direction in the field emission technology, and a new type of materials (such as, different TCOs) might become a promising candidate for low-threshold field emitter.

10. Future Directions

First and foremost future course of our research will be to increase the conductivity of these p-TCO materials. The maximum conductivity of our p- CuAlO_2 film is almost two orders of magnitude less than that of commercially available n-TCO films. So this may put hindrance in the formation of effective active devices for large-scale production. It is found that nonstoichiometric oxygen intercalation within the material has its limitation to increase the conductivity of the film. Excess oxygen intercalation, beyond an optimum value, is found to deteriorate the film quality. So intentional doping of the material is the obvious step to increase the conductivity of the film. Identification of proper dopant and doping procedure will be the focus of our future work. Several theoretical articles have been published so far [163, 164, 227, 228, 274], indicating various doping materials and procedures to enhance the electrical characteristics of this material but no experimental work has yet been reported, as far as literature survey goes. Therefore, doping of p- CuAlO_2 thin film for superior device quality films is an important area of research for the development of “Transparent Electronics”.

Another interesting area of research is the cost-effective fabrication of transparent junctions, without compromising its electro-optical properties. This is important for the large-scale production of various junctional devices with diverse applications. Here we have used a combination of cost-effective physical and chemical routes but future work will be aimed to improve the opto-electrical properties of these transparent junctions.

Another area of research, which is not yet explored completely, but has tremendous potential, is the thermoelectric properties of CuAlO_2 films. Being a layered-structured material, this material as well as other delafossite materials can become very good candidate for thermoelectric converters. Recently, Park et al [275] have reported a significant increase in the thermoelectric properties of this material for Ca substitution in Al sites at high temperature. They have observed the highest value of power factor around $7.82 \times 10^{-5} \text{ Wm}^{-1} \text{ K}^{-2}$ for $\text{CuAl}_{0.9}\text{Ca}_{0.1}\text{O}_2$ at 1140 K. If proper studies can be done on the thermoelectric properties of these types of superlattice materials, new horizon may open up in the field of thermoelectric converters.

Also keeping an eye in the tremendous progress in nanotechnology, fabrication and characterization of nano-structured p- CuAlO_2 as well as other p-TCO thin films may become an important field of work, because of new and interesting properties exhibited by these nano-materials. Proper fabrication procedure to get reproducible nano-materials is the most important future work. Also in-depth studies of the photoluminescence properties of p- CuAlO_2 nano-particles will be another area of research, which is needed to be explored properly. Fabrication of nano-structured p-TCOs, coupled with the already existing and well-known materials of nano-structured n-TCOs, will give an added impetus in the field of "Invisible Electronics" for the fabrication of nano-active devices, which can have high-efficient applications in the optoelectronics device technology.

Field-emission property of CuAlO_2 thin films is a completely new area of research, which has tremendous opportunities. This material showed very low turn-on field comparable to most of the carbonaceous low-threshold field-emitters like CNT, DLC, diamond, a:C, SiC-nanorods etc. So these types of TCO materials may become promising alternative to the existing materials in the field of FED technology. But, proper emission mechanism in these materials is not very clear till date and very good scopes are there to properly investigate the emission mechanism so that the material properties can be tuned accordingly to get better field-emission properties of these films.

Also recent study showed that p- CuAlO_2 can become a good candidate for ozone sensors. Zheng and co-authors [276] reported that CuAlO_2 has a selective and reversible response to ozone gas at room temperature. All existing commercial semiconductor ozone sensors are of n-type [277-280]. This study demonstrated the feasibility of developing an inexpensive p-type transparent ozone sensor. Hence, transparent p-n junction ozone sensors may be fabricated using the p- CuAlO_2 and existing n-TCO such as In_2O_3 .

Photocatalytic hydrogen evolution over delafossite CuAlO_2 is another interesting report published recently by Koriche et al [281]. This group proposed a new photochemical system for water reduction based on p- CuAlO_2 and S^{2-} as hole scavenger. They have used co-precipitation method, a new synthetic route, to synthesis CuAlO_2 , which increased the surface to volume ratio and delivered a highest H_2 production. This report is very interesting and shows newer applications of delafossite p- CuAlO_2 material.

Also, recently Kizaki and co-authors [282] proposed a materials designing procedure to get CuAlO_2 -based dilute magnetic semiconductors. Ab-initio calculations showed that Fe- and Mn-doped CuAlO_2 -based dilute magnetic semiconductors possess high-Curie-temperature ferromagnetic characteristics. Being a natural p-type transparent semiconductor without intentional doping, CuAlO_2 can easily be used for the host of dilute magnetic semiconductors. Also, most importantly, the delafossite structure of CuAlO_2 has the advantage of possessing two cation-sites, Cu^{+1} and Al^{+3} sites, for possible magnetic ion

substitution. O–Cu–O dumbbell-sites in delafossite CuAlO_2 can be partially replaced with magnetic ions. Due to this coordination one can realize new ferromagnetic dilute magnetic semiconductors from the standpoint of the hybridization of orbitals between 3d orbitals with the impurities and 2p orbitals with the oxygen in CuAlO_2 .

Therefore, it will not be an exaggeration to say that next decade will see the renaissance of delafossite materials and various new, interesting and novel technological applications with these materials are on the verge of exploration.

Acknowledgement

The authors wish to gratefully acknowledge the financial assistance of the Department of Science and Technology, Govt. of India, during the execution of the work.

References

- [1] Badekar, K. *Ann. Phys. (Leipzig)* 1907, 22, 749.
- [2] Lampert, C. M. *Sol. Energy Mater.* 1981, 6, 1-41.
- [3] Chopra, K. L.; Major, S.; Pandya, D. K. *Thin Solid Films* 1983, 102, 1-46.
- [4] Hamberg, I.; Granqvist, C. G. *J. Appl. Phys.* 1986, 60, R123-R160.
- [5] Holland, L. *Vacuum Deposition of Thin Films*; Wiley: New York, NY, 1958; pp. 492.
- [6] Cachet, H.; Gamard, A.; Campet, G.; Jousseau, B.; Toupance, T. *Thin Solid Films* 2001, 388, 41-49.
- [7] Wendt, R.; Ellmer, K. *Surf. Coat. Technol.* 1997, 93, 27-31.
- [8] Hartnagel, H. L.; Dawar, A. L.; Jain, A. K.; Jagadish, C. *Semiconducting Transparent Thin Films*; IOP Publishing Ltd.: Bristol and Philadelphia, PA, 1995.
- [9] Ginley, D. S.; Bright, C. *MRS Bull.* August 2000, pp.15.
- [10] Cava, R. J.; Philips, J. M.; Kwo, J.; Thomas, G. A.; van Dover, R. B.; Carter, S. A.; Krajewski, J. J.; Peck Jr., W. F.; Marshall, J. H.; Rapkin, D. H. *Appl. Phys. Lett.* 1994, 64, 2071-2073.
- [11] Philips, J. M.; Cava, R. J.; Thomas, G. A.; Carter, S. A.; Kwo, J.; Siegrist, T.; Krajewski, J. J.; Marshall, J. H.; Peck Jr., W. F.; Rapkin, D. H. *Appl. Phys. Lett.* 1995, 67, 2246-2248.
- [12] Freeman, A. J.; Poepelmeier, K. R.; Mason, T. O.; Chang, R. P. H.; Marks, T. J. *MRS Bull.* August 2000, pp.45.
- [13] Gordon, R. G. *MRS Bull.* August 2000, pp.52.
- [14] Mochel, J. M. *U.S. Patent No.* 2,564,706, 1947.
- [15] Sinclair, W. R.; Peters, F. G.; Stillinger, D.W.; Koonce, S. E. *J. Electrochem. Soc.* 1965, 112, 1096.
- [16] Lytle, W. O.; Junge, A. E. *U. S. Patent No.* 2,566,346 (1951).
- [17] Gordon, R. G. *U. S. Patent No.* 4,146,657, 1979.
- [18] Banerjee, A. N.; Kundoo, S.; Saha, P.; Chattopadhyay, K. K. *J. Sol-Gel Sci. Technol.* 2003, 28, 105-110.
- [19] Banerjee, A. N.; Maity, R.; Kundoo, S.; Chattopadhyay, K. K. *Phys. Stat. Solidi A* 2004, 201, 983-989.

- [20] Major, S.; Banerjee, A.; Chopra, K. L. *Thin Solid Films* 1984, 122, 31-43.
- [21] Minami, T.; Nanto, H.; Takata, S. *Jpn. J. Appl. Phys.*, Part 2: Lett. 1984, 23, L280-L282.
- [22] Hu, J.; Gordon, R. G.; *Sol. Cells* 1991, 30, 437-450.
- [23] Vijayakumar, P. S.; Blaker, K. A.; Welting, R. D.; Wong, B.; Halani, A. T.; Park, C. U. *U. S. Patent* No. 4,751,149, 1988.
- [24] Choi, B. H.; Im, H. B.; Song, J. S.; Yoon, K. H. *Thin Solid Films* 1990, 193, 712-720.
- [25] Hu, J.; Gordon, R. G. *J. Appl. Phys.* 1992, 72, 5381-5392.
- [26] Mochel, J. M.; *U. S. Patent* No. 2, 564,707, 1951.
- [27] Holland, L.; Siddall, G. *Vacuum III* 1955.
- [28] Avaritsiotis, J. N.; Howson, R. P. *Thin Solid Films* 1981, 77, 351-357.
- [29] Groth, R. *Phys. Stat. Solidi* 1966, 14, 69.
- [30] Nozik, A. J.; *U. S. Patent* No. 3,811,953, 1974.
- [31] Haacke, G.; Mealmaker, W. E.; Siegel, L. A. *Thin Solid Films* 1978, 55, 67-81.
- [32] Vossen, J. L. *RCA Rev.* 1971, 32, 269.
- [33] Enoki, H.; Nakayama, T.; Echigoya, J. *Phys. Stat. Solidi A* 1992, 129, 181.
- [34] Minami, T.; Sonohara, H.; Takata, S.; Sato, H. *Jpn. J. Appl. Phys.*, Part 2: Lett. 1994, 33, L1693-L1696.
- [35] Phillips, J. M.; Kwo, J.; Thomas, G. A.; Carter, S. A.; Cava, R. J.; Hou, S. Y.; Krajewski, J. J.; Marshall, J. H.; Pack, W. F.; Rapkin, D. H.; van Dover, R. B. *Appl. Phys. Lett.* 1994, 65, 115-117.
- [36] Otabe, T.; Ueda, K.; Kudoh, A.; Hosono, H.; Kawazoe, H. *Appl. Phys. Lett.* 1998, 72, 1036-1038.
- [37] Dali, S. E.; Jayachandran, M.; Chockalingam, M. J. *J. Mater. Sci. Lett.* 1999, 18, 915-917.
- [38] Edwards, D. D.; Mason, T. O.; Goutenoire, F.; Poeppelmeier, K. R.; *Appl. Phys. Lett.* 1997, 70, 1706-1708.
- [39] Minami, T.; Takata, S.; Kakumu, T.; Sonohara, H. *Thin Solid Films* 1995, 270, 22-26.
- [40] Minami, T.; Kakumu, T.; Shimokawa, K.; Takata, S. *Thin Solid Films* 1998, 317, 318-321.
- [41] Omata, T.; Ueda, N.; Ueda, K.; Kawazoe, H. *Appl. Phys. Lett.* 1994, 64, 1077-1078.
- [42] Kammler, D. R.; Mason, T. O.; Young, D. L.; Coutts, T. J. *J. Appl. Phys.* 2001, 90, 3263-3268.
- [43] Minami, T. *MRS Bull.* August 2000, pp. 38.
- [44] Lewis, B. G.; Paine, D. C. *MRS Bull.* August 2000, pp. 22.
- [45] Granqvist, C. G.; Azens, A.; Hjelm, A.; Kullman, L.; Niklasson, G. A.; Ronnow, D.; Mattson, M. S.; Veszelei, M.; Vaivars, G. *Sol. Energy* 1998, 63, 199-216.
- [46] Kammler, D. R.; Edwards, D. D.; Ingram, B. J.; Mason, T. O.; Palmer, G. B.; Ambrosini, A.; Poeppelmeier, K. R. In *Photovoltaics for the 21st Century*; Kapur, V. K.; McConnel, R. D.; Carlson, D.; Ceasan, G. P.; Rohatgi A.; Ed.; *The Electrochem. Soc. Proc.* **99-11**; Pennington, NJ, 1999; pp. 68.
- [47] Lee, S. H.; Hwang, K. H.; Joo, S. K. In *Electrochromic Materials*; Ho, K. C.; McArthur D. A.; Ed.; *The Electrochem. Soc. Proc.* **94-2**; Pennington, NJ, 1994; pp. 290.
- [48] Lugg, P. S.; Bommarito, S.; Bailey, J.; Budd, K.; Cullen, P.; Chen, K.; Hardy, L. C.; Nachbor, M. In *Solid State Ionic Devices*; Wachsman, E.D.; Akridge, J. R.; Liu, M.; Yamazoe, N.; Ed.; *The Electrochem. Soc. Proc.* **99-13**; Pennington, NJ, 1999; pp. 284.

- [49] Nakato, Y.; Kai, K. I.; Kawabe, K. *Sol. Energy Mater. Sol. Cells* 1995, 37, 323-335.
- [50] Emons, T. T.; Li, J.; Nazar, L. F. *J. Am. Chem. Soc.* 2002, 124, 8517.
- [51] Hutchins, M. G.; McMeeking, G. D. *Biosensor Patent No. 90,27,607.2*, 1990.
- [52] He, Y.; Kanicki, J. *Appl. Phys. Lett.* 2000, 76, 661.
- [53] Wager, J. F. *Science* 2003, 300, 1245.
- [54] Lampert, C. M. *Solar Energy Materials* 1990, 21, 191.
- [55] Grivas, C.; Mallis, S.; Boutsikaris, L.; Gill, D. S.; Vainos, N. A.; Chandler, P. J. *Laser Phys.* 1998, 8, 326.
- [56] Moschovis, K.; Gagaoudakis, E.; Chatzitheodoridis, E.; Kiriakidis, G.; Mailis, S.; Tzamali, E.; Vainos, N. A.; Fritzsche, H. *Appl. Phys. A* 1998, 66, 651.
- [57] Moller, S.; Perlov, C.; Jackson, W.; Taussig, C.; Forest, S. R. *Nature* 2003, 426, 166.
- [58] Hayes, R. A.; Feenstra, B. J. *Nature* 2003, 425, 1038.
- [59] Cornia, R. L.; Fenn, J. B.; Memarian, H.; Ringer, R. In *Proc. 41st Annual Technical Conference*; Soc. of Vacuum Coaters; Boston, MA, 1998; pp. 452.
- [60] Cairns, D. R.; Witte, R. P.; Sparacin, D. K.; Sachsman, S. M.; Paine, D. C.; Crawford, G. P.; Newton, R. *Appl. Phys. Lett.* 2000, 76, 1425.
- [61] Banerjee, A. N.; Ghosh, C. K.; Chattopadhyay, K. K.; Minoura, H.; Sarkar, A. K.; Akiba, A.; Kamiya, A.; Endo, T. *Thin Solid Films* 2006, 496, 112-116.
- [62] Seager, C. H.; McIntyre, D. C.; Warren, W. L.; Tuttle, B. A. *Appl. Phys. Lett.* 1996, 68, 2660.
- [63] Prince, M. W. J.; Gross-Holtz, K. O.; Muller, G.; Cillessen, J. B.; Giesbers, J. B.; Weening, R. P.; Wolf, R. M. *Appl. Phys. Lett.* 1996, 68, 3650.
- [64] Kawazoe, H.; Yasukawa, M.; Hyodo, H.; Kurita, M.; Yanagi, H.; Hosono, H. *Nature* 1997, 389, 939.
- [65] Thomas, G. *Nature* 1997, 389, 907.
- [66] Sato, H.; Minami, T.; Takata, S.; Yamada, T. *Thin Solid Films* 1993, 236, 27.
- [67] Yanagi, H.; Inoue, S.; Ueda, K.; Kawazoe, H.; Hosono, H.; Hamada, N. *J. Appl. Phys.* 2000, 88, 4159.
- [68] Efros, A. L.; Efros, A. L. *Sov. Phys. Semicond.* 1982, 16, 772.
- [69] Brus, L. E. *J. Chem. Phys.* 1984, 80, 4403.
- [70] Cox, A. J.; Louderback, J. G.; Bloomfield, L. A. *Phys Rev. Lett.* 1993, 71, 923.
- [71] Alivisatos, A. P. *Science* 1996, 271, 933.
- [72] Heath, J. R. *Science* 1995, 270, 1315.
- [73] Demel, T.; Heitmann, D.; Grambow, P.; Ploog, K. *Phys. Rev. Lett.* 1990, 64, 2559.
- [74] Li, Q.; Wang, C. *Appl. Phys. Lett.* 2003, 83, 359.
- [75] Demel, T.; Heitmann, D.; Grambow, P.; Ploog, K. *Phys. Rev. Lett.* 1991, 66, 2657.
- [76] Klein, D. L.; Roth, R.; Lim, A. K. L.; Alivisatos, A. P.; McEuen, P. L. *Nature* 1997, 389, 699.
- [77] Feldheim, D. L.; Keating, C. D. *Chem. Soc. Rev.* 1998, 28, 1.
- [78] Fink, R. L.; Li Tolt, Z.; Yaniv, Z. *Surf. Coat. Technol.* 1998, 108-109, 570.
- [79] May, P. W.; Hohn, S.; Wang, W. N.; Fox, N. A. *Appl. Phys. Lett.* 1998, 72, 2182.
- [80] Baek, Y. G.; Ikuno, T.; Ryu, J. T.; Honda, S. I.; Katayama, M.; Oura, K.; Hirao, T. *Appl. Surf. Sci.* 2002, 185, 243.
- [81] Robertson, J. *Diamond Relat. Mater.* 1996, 5, 797.
- [82] Hirakuri, K.; Yokoyama, T.; Enomoto, H.; Mutsukura, N.; Friedbacher, G. *J. Appl. Phys.* 2001, 89, 8253.

- [83] Yanagi, H.; Kawazoe, H.; Kudo, A.; Yasukawa, M.; Hosono, H. *J. Electroceram.* 2000, 4, 427.
- [84] May, P. W.; Hohn, S.; Wang, W. N.; Fox, N. A. *Appl. Phys. Lett.* 1998, 72, 2182.
- [85] Baek, Y. G.; Ikuno, T.; Ryu, J. T.; Honda, S. I.; Katayama, M.; Oura, K.; Hirao, T. *Appl. Surf. Sci.* 2002, 185, 243.
- [86] Chen, C. F.; Lin, C. L.; Wang, C. M. *Appl. Phys. Lett.* 2003, 82, 2515.
- [87] Zhou, X. T.; Lai, H. L.; Peng, H. Y.; Au, F. C. K.; Liao, L. S.; Wang, N.; Bello, I.; Lee, C. S.; Lee, S. T. *Chem. Phys. Lett.* 2000, 318, 58.
- [88] Tate, J.; Jayaraj, M. K.; Draeseke, A. D.; Ulbrich, T.; Sleight, A. W.; Vanaja, K. A.; Nagrajan, R.; Wager, J. F.; Hoffman, R. L. *Thin Solid Films* 2002, 411, 119.
- [89] Nagrajan, R.; Duan, N.; Jayaraj, M. K.; Li, J.; Vanaja, K. A.; Yokochi, A.; Draeseke, A.; Tate, J.; Sleight, A. W. *Int. J. Inorg. Mater.* 2001, 3, 265.
- [90] Nagrajan, R.; Uma, S.; Jayaraj, M. K.; Tate, J.; Sleight, A. W. *Solid State Science* 2002, 4, 787.
- [91] Norton, D. P. *Mat. Sci. Engg.* 2004, R 43, 139.
- [92] Banerjee, A. N.; Chattopadhyay, K. K. *Prog. Cryst. Growth and Charac. Mater.* 2005, 50, 52-105.
- [93] Shannon, R. D.; Rogers, D. B.; Prewitt, C. T. *Inorg. Chem.* 1971, 10, 713.
- [94] Prewitt, C. T.; Shannon, R. D.; Rogers, D. B. *Inorg. Chem.* 1971, 10, 719.
- [95] Rogers, D. B.; Shannon, R. D.; Prewitt, C. T.; Gilson, J. L. *Inorg. Chem.* 1971, 10, 723.
- [96] Hahn, H.; Lorent, C. Z. *Anorg. Allg. Chem.* 1955, 279, 281.
- [97] Benko, F. A.; Koffyberg, F. P. *J. Phys. Chem. Solids* 1984, 45, 57.
- [98] Ishiguro, T.; Kitazawa, A.; Mizutani, N.; Kato, M. *J. Solid State Chem.* 1981, 40, 170.
- [99] Ishiguro, T.; Ishizawa, N.; Mizutani, N.; Kato, M. *J. Solid State Chem.* 1982, 41, 132.
- [100] Ishiguro, T.; Ishizawa, N.; Mizutani, N.; Kato, M. *Acta. Cryst.* 1983, B39, 564.
- [101] Ueda, K.; Hase, T.; Yanagi, H.; Kawazoe, H.; Hosono, H.; Ohta, H.; Orita, M.; Hirano, M. *J. Appl. Phys.* 2001, 89, 1790.
- [102] Yanagi, H.; Hase, T.; Ibuki, S.; Ueda, K.; Hosono, H. *Appl. Phys. Lett.* 2001, 78, 1583.
- [103] Yanagi, H.; Ueda, K.; Ohta, H.; Orita, M.; Hirano, M.; Hosono, H. *Solid State Comm.* 2001, 121, 15.
- [104] Kohler, B. V.; Jansen, M. Z. *Anorg. Allg. Chem.* 1986, 543, 73.
- [105] Shimode, M.; Sasaki, M.; Mukaida, K. *J. Solid State Chem.* 2000, 151, 16.
- [106] Robertson, J.; Peacock, P. W.; Towler, M. D.; Needs, R. *Thin Solid Films* 2002, 411, 96.
- [107] Ingram, B. J.; Mason, T. O.; Asahi, R.; Park, K. T.; Freeman, A. J. *Phys. Rev. B* 2001, 64, 155114.
- [108] Duan, N.; Sleight, A. W.; Jayaraj, M. K. Tate, J. *Appl. Phys. Lett.* 2000, 77, 1325.
- [109] Nagrajan, R.; Draeseke, A. D.; Sleight, A. W.; Tate, J. *J. Appl. Phys.* 2001, 89, 8022.
- [110] Jayaraj, M. K.; Draeseke, A. D.; Tate, J.; Sleight, A. W. *Thin Solid Films* 2001, 397, 244.
- [111] Mattheiss, L. F.; *Phys. Rev. B* 1993, 48, 18300.
- [112] Crottaz, O.; Kubel, F.; Schmid, H. J. *Solid State Chem.* 1996, 122, 247.
- [113] Powder Diffraction File; Joint Committee on Powder Diffraction Standards, ASTM; Philadelphia, PA, 1967; Card # 35-1401.
- [114] Yanagi, H.; Park, S.; Draeseke, A. D.; Keszler, D. A.; Tate, J. *J. Solid State Chem.* 2003, 175, 34.

-
- [115] Ueda, K.; Inoue, S.; Hirose, S.; Kawazoe, H.; Hosono, H. *Appl. Phys. Lett.* 2000, 77, 2701.
- [116] Kudo, A.; Yanagi, H.; Hosono, H.; Kawazoe, H. *Appl. Phys. Lett.* 1998, 73, 220.
- [117] Teske, C. L.; Müller-Buschbaum, H. *Z. Anorg. Allg. Chem.* 1970, 379, 113.
- [118] Boudin, S.; Felser, C.; Studer, F. *Solid State Sciences* 2003, 5, 741.
- [119] Hiramatsu, H.; Ueda, K.; Ohta, H.; Orita, M.; Hirano, M.; Hosono, H. *Thin Solid Films* 2002, 411, 125.
- [120] Palazzi, M. *Acad. Sci., Paris, C. R.* 1981, 292, 789.
- [121] Ishikawa, K.; Kinoshita, S.; Suzuki, Y.; Matsuura, S.; Nakanishi, T.; Aizawa, M.; Suzuki, Y. *J. Electrochem. Soc.* 1991, 138, 1166.
- [122] Takano, Y.; Yahagi, K. -I.; Sekizawa, K. *Physica B* 1995, 206 & 207, 764.
- [123] Ueda, K.; Inoue, S.; Hosono, H.; Sarukura, N.; Hirano, M. *Appl. Phys. Lett.* 2001, 78, 2333.
- [124] Ueda, K.; Hosono, H. *J. Appl. Phys.* 2002, 91, 4768.
- [125] Takase, K.; Koyano, M.; Shimizu, T.; Makihara, K.; Takahashi, Y.; Takano, Y.; Sekizawa, K. *Solid State Comm.* 2002, 123, 531.
- [126] Hiramatsu, H.; Orita, M.; Hirano, M.; Ueda, K.; Hosono, H. *J. Appl. Phys.* 2002, 91, 9177.
- [127] Hiramatsu, H.; Ueda, K.; Takafuji, K.; Ohta, H.; Orita, M.; Hirano, M.; Kamiya, T.; Hosono, H. *J. Appl. Phys.* 2003, 94, 5805.
- [128] Hiramatsu, H.; Ueda, K.; Ohta, H.; Hirano, M.; Kamiya, T.; Hosono, H. *Appl. Phys. Lett.* 2003, 82, 1048.
- [129] Ueda, K.; Hiramatsu, H.; Ohta, H.; Hirano, M.; Kamiya, T.; Hosono, H. *Phys. Rev. B* 2004, 69, 155305.
- [130] Ueda, K.; Hosono, H. *Thin Solid Films* 2002, 411, 115.
- [131] Zhu, W. J.; Huang, Y. Z.; Dong, C.; Zhao, Z. X. *Mater. Res. Bull.* 1994, 29, 143.
- [132] Inoue, S. -I.; Ueda, K.; Hosono, H.; Hamada, N. *Phys. Rev. B* 2001, 64, 245211.
- [133] Furukawa, Y.; Ikeda, S.; Kumagai, K.; Mori, K.; Takano, Y.; Sekizawa, K. *Phys. Rev. B* 2000, 62, 15598.
- [134] Takano, Y.; Mori, K.; Koizumi, K.; Ozaki, H.; Sekizawa, K. *J. Alloys Compd.* 1998, 275-277, 447.
- [135] Sekizawa, K.; Takano, Y.; Mori, K.; Yahagi, T. *Czech. J. Phys.* 1996, 46, 1943.
- [136] Park, S.; Keszlor, D. A.; Valencia, M. M.; Hoffman, R. L.; Bender, J. P.; Wager, J. F. *Appl. Phys. Lett.* 2002, 80, 4393.
- [137] Wu, W. J.; Huang, Y. Z.; Wu, F.; Dong, C.; Chen, H.; Zhao, Z. X. *Mater. Res. Bull.* 1994, 29, 505.
- [138] Yanagi, H.; Park, S.; Draeseke, A. D.; Keszler, D. A. J. Tate, J. *Solid State Chem.* 2003, 175, 34.
- [139] Iglesias, J. E.; Pachali, K. E.; Stoinfink, H. J. *Solid State Chem.* 1974, 9, 6.
- [140] Maissel, L. I.; Glang, R. *Handbook of Thin Films Technology*; McGraw-Hill: New York, NY, 1970.
- [141] Chrisey, D. B.; Hübner, G. K. *Pulsed Laser Deposition of Thin Films*; Wiley-Interscience: New York, NY, 1994.
- [142] Chopra, K. L. *Thin Film Phenomena*; McGraw-Hill: New York, NY, 1969.
- [143] Anderson, J. C. *The Use of Thin Films in Physical Investigations*; Academic: New York, NY, 1966.

- [144] Kawazoe, H.; Yanagi, H.; Ueda, K.; Hosono, H. *MRS Bull.* August 2000, pp. 28.
- [145] Stauber, R. E.; Perkins, J. D.; Parilla, P. A.; Ginley, D. S. *Electrochem. Solid State Lett.* 1999, 2, 654.
- [146] Ong, C. H.; Gong, H. *Thin Solid Films* 2003, 445, 299.
- [147] Tsuboi, N.; Takahashi, Y.; Kobayashi, S.; Shimizu, H.; Kato, K.; Kaneko, F. *J. Phys. Chem. Solids* 2003, 64, 1671.
- [148] Alkoy, E.M.; Kelly, P. J. *Vacuum* 2005, 75, 221.
- [149] Wang, Y.; Gong, H. *Advanced Materials CVD* 2000, 6, 285.
- [150] Gong, H.; Wang, Y.; Luo, Y. *Appl. Phys. Lett.* 2000, 76, 3959.
- [151] Wang, Y.; Gong, H.; Zhu, F.; Liu, L.; Huang, L.; Huan, A. C. H. *Mater. Sci. Engg. B* 2001, 85, 131.
- [152] Kim, D. -S.; Choi, S. -Y. *Phys. Stat. Solidi (A)* 2005, 202, R167.
- [153] Tonooka, K.; Shimokawa, K.; Nishimura, O. *Thin Solid Films* 2002, 411, 129.
- [154] Gao, S.; Zhao, Y.; Gou, P.; Chen, N.; Xie, Y. *Nanotechnology* 2003, 14, 538.
- [155] Shy, J. H.; Tseng, B. H.; *J. Phys. Chem. Solids* 2005, 66, 2123.
- [156] Bouzidi, C.; Bouzouita, H.; Timoumi, A.; Rezig, B. *Mater. Sci. Engg. B* 2005, 118, 259.
- [157] Ohashi, M.; Iida, Y.; Morikawa, H. *J. Am. Ceram. Soc.* 2002, 85, 270.
- [158] Dloczik, L.; Tömm, Y.; Könenkamp, R. *Thin Solid Films* 2004, 451–452, 116–119.
- [159] Shahriari, D. Y.; Barnabè, A.; Mason, T. O.; Poeppelmeier, K. R. *Inorg. Chem.* 2001, 40, 5734.
- [160] Banerjee, A. N.; Kundoo, S.; Chattopadhyay, K.K. *Thin Solid Films* 2003, 440, 5 – 10.
- [161] Banerjee, A. N.; Maity, R.; Chattopadhyay, K. K. *Materials Letters* 2003, 58, 10 - 13.
- [162] Ghosh, P. K.; Banerjee, A. N.; Maity, R.; Chattopadhyay K. K. (unpublished data).
- [163] Yoshida, H. K.; Koyanagi, T.; Funashima, H.; Harima, H.; Yanase, A. *Solid State Comm.* 2003, 126, 135.
- [164] Koyanagi, T.; Harima, H.; Yanase, A.; Yoshida, H. K. *J. Phys. Chem. Solids* 2003, 64, 1443.
- [165] Kudo, A.; Yanagi, H.; Ueda, K.; Hosono, H.; Kawazoe, H.; Yano, Y. *Appl. Phys. Lett.* 1999, 75, 2851.
- [166] Ohta, H.; Kawamura, K.; Orita, M.; Sarukura, N.; Hirano, M.; Hosono, H. *Electron. Lett.* 2000, 36, 984.
- [167] Ohta, H.; Kawamura, K.; Orita, M.; Hirano, M.; Sarukura, N.; Hosono, H. *Appl. Phys. Lett.* 2000, 77, 475.
- [168] Ohta, H.; Orita, M.; Hirano, M. *J. Appl. Phys.* 2001, 89, 5720.
- [169] Hosono, H.; Ohta, H.; Hayashi, K.; Orita, M.; Hirano, M. *J. Cryst. Growth* 2002, 237–239, 496.
- [170] Hoffman, R. L.; Wager, J. F.; Jayaraj, M. K.; Tate, J. *J. Appl. Phys.* 2001, 90, 5763.
- [171] Jayaraj, M. K.; Draeseke, A. D.; Tate, J.; Hoffman, R. L.; Wager, J. F. *Mat. Res. Soc. Proc.* 2001, 666, F4.1.
- [172] Tonooka, K.; Bando, H.; Aiura, Y. *Thin Solid Films*, **445** (2003) 327.
- [173] Hwang, D. -K.; Bang, K. -H.; Jeong, M. -C.; Myoung, J. -M. *J. Cryst. Growth* 2003, 254, 449.
- [174] Tüzemen, S.; Xiong, G.; Wilkinson, J.; Mischuck, B.; Ucer, K. B.; Williams, R. T. *Physica B* 2001, 308-310, 1197.
- [175] Aoki, T.; Hatanaka, Y.; Look, D. C. *Appl. Phys. Lett.* 2000, 76, 3257.

- [176] Butkhuzi, T. V.; Bureyev, A. V.; Georgobiani, A. N.; Kekelidze, N. P.; Khulordava, T. G. *J. Cryst. Growth* 1992, 117, 366.
- [177] Wager, J. F. *Science* 2003, 300, 1245.
- [178] Prins, M. W. J.; Grosse-Holz, K.-O.; Müller, G.; Cillessen, J. F. M.; Giesbers, J. B.; Weening, R. P.; Wolf, R. M. *Appl. Phys. Lett.* 1996, 68, 3650.
- [179] Prins, M. W. J.; Zinnemers, S. E.; Cillessen, J. F. M.; Giesbers, J. B. *Appl. Phys. Lett.* 1997, 70, 458.
- [180] Hoffman, R. L.; Norris, B. J.; Wager, J. F. *Appl. Phys. Lett.* 2003, 82, 733.
- [181] Masuda, S.; Kitamura, K.; Okumura, Y.; Miyatake, S.; Tabata, H.; Kawai, T. *J. Appl. Phys.* 2003, 93, 1624.
- [182] Carcia, P. F.; McLean, R. S.; Reilly, M. H.; Nunes, Jr. G.; *Appl. Phys. Lett.* 2003, 82, 1117.
- [183] Nomura, K.; Ohta, H.; Ueda, K.; Kamiya, T.; Hirano, M.; Hosono, H. *Science* 2003, 300, 1269.
- [184] Ohta, H.; Nomura, K.; Hiramatsu, H.; Ueda, K.; Kamiya, T.; Hirano, M.; Hosono, H. *Solid-State Electronics* 2003, 47, 2261.
- [185] Banerjee, A. N.; Chattopadhyay, K. K. *J. Appl. Phys* 2005, 97, 084308.
- [186] Jacob, A.; Parent, C.; Boutinaud, P.; Le Flem, G.; Doumerc, J. P.; Ammar, A.; Elazhari M.; Elaati, M. *Solid State Comm.* 1997, 103, 529.
- [187] Hasegawa, S.; Nishida, S.; Yamashita, T.; Asahi, H. *Thin Solid Films* 2005, 487, 260.
- [188] Hasegawa, S.; Nishida, S.; Yamashita, T.; Asahi, H. *J. Ceram. Processing Res.* 2005, 6, 245.
- [189] Yu, K.; Zhang, Y.; Luo, L.; Zhu, Z. *Proc. SPIE-The Int. Soc. Optical Engg.* 2005, 5774, 353.
- [190] Liu, B.; Bando, Y.; Tang, C.; Xu, F.; Hu, J.; Golberg, D. *J. Phys. Chem. B* 2005, 109, 17082.
- [191] Liu, B. D.; Bando, Y.; Tang, C. C.; Xu, F. F.; Golberg, D. *J. Phys. Chem. B* 2005, 109, 21521.
- [192] Yue, S. L.; Gu, C. Z.; Shi, C. Y.; Zhi, C. Y. *Appl. Surf. Sci.* 2005, 251, 215.
- [193] Wang, Y. X.; Li, Y. A.; Feng, W.; Li, W. Q.; Zhao, C. H.; Liu, L. H.; Feng, K. C.; Zhao, Y. N. *Appl. Surf. Sci.* 2005, 243, 394.
- [194] Tong, Y.; Cong, H.; Chen, Z.; Cheng, H. *Appl. Phys. Lett.* 2005, 86, 233104.
- [195] Liu, C.; Hu, Z.; Wu, Q.; Wang, X.; Chen, Y.; Lin, W.; Sang, H.; Deng, S.; Xu, N. *Appl. Surf. Sci.* 2005, 251, 220.
- [196] Tang, Y. B.; Cong, H. T.; Zhao, Z. G.; Chen, H. M. *Appl. Phys. Lett.* 2005, 86, 153104.
- [197] Chen, S. -C.; Chen, C. -F.; Chattopadhyay, S.; Chen, K. -H.; Chen, L. -C. *Appl. Phys. Lett.* 2005, 87, 073109.
- [198] Olesik, J.; Malachowski, M. *Thin Solid Films* 2002, 422, 193.
- [199] Baranauskas, V.; Fontana, M.; Guo, Z. J.; Ceragioli, H. J.; Peterlevitz, A. C. *Sensors and Actuators B: Chemical* 2005, 107, 474.
- [200] Jo, S. H.; Lao, J. Y.; Ren, Z. F.; Farrer, R. A.; Baldacchini, T.; Fourkas, J. T. *Appl. Phys. Lett.* 2003, 83, 4821.
- [201] Dong, L.; Jiao, J.; Tuggle, D. W.; Petty, J. M.; Elliff, S. A.; Coulter, M. *Appl. Phys. Lett.* 2003, 82, 1096.
- [202] Xu, C.; Sun, X. *Int. J. Nanotechnology* 2004, 1, 452.

- [203] Yang, H. Y.; Lau, S. P.; Yu, S. F.; Huang, L.; Tanemura, M.; Tanaka, J.; Okita, T.; Hng, H. H. *Nanotechnology* 2005, 16, 1300.
- [204] Maity, R.; Banerjee, A. N.; Chattopadhyay, K. K. *Appl. Surf. Sci.* 2004, 236, 231.
- [205] Maity, R.; Das, S.; Mitra, M. K.; Chattopadhyay, K. K. *Physica E* 2005, 25, 605.
- [206] Yang, Y. H.; Wang, C. X.; Wang, B.; Xu, N. S.; Yang, G. W. *Chem. Phys. Lett.* 2005, 403, 248.
- [207] Banerjee, A. N.; Chattopadhyay, K. K. *Appl. Surf. Sci.* 2004, 225, 10.
- [208] Banerjee, A. N.; Ghosh, C. K.; Das, S.; Chattopadhyay, K. K. *Physica B* 2005, 370, 264.
- [209] Fowler, R. H.; Nordheim, L. *Proc. Roy. Soc. Lond.* 1928, A119, 173.
- [210] Murphy, E. L.; Good Jr., R. H. *Phys. Rev.* 1956, 102, 1464.
- [211] Schwettman, H. A.; Turneure, J. P.; Waites, R. F. *J. of Appl. Phys.* 1974, 45, 914.
- [212] Latham, R. V. *IEEE Trans. Elec. Insul.* 1983, EI-18, 194.
- [213] Forbes, R. G. *Solid-State Electronics* 2001, 45, 779.
- [214] Forbes, R. G. *J. Vac. Sci. Technol. B* 1999, 17, 526.
- [215] DeVault, D. *J. Chem. Educ.* 1944, 21, 526.
- [216] Bailar Jr., J. C.; Emeléus, H. J.; Sir Ronald, N.; Trotman-Dickenson, A. F. *Comprehensive Inorganic Chemistry*; Pergamon: New York, NY, 1973.
- [217] Leung, Y. K.; Khan, A. K.; Kos, J. F.; Koffyberg, F. P. *Proc. Nat. Conf. Solar Energy*; Solar Energy Society of Canada, Montreal, 1981; pp. 124.
- [218] Dahl, J. P.; Switendick, A. C. *J. Phys. Chem. Solids* 1966, 27, 931.
- [219] Hayashi, M.; Katsuki, K. *J. Phys. Soc. Jpn.* 1950, 5, 380.
- [220] Kleinman, L.; Mednick, K. *Phys. Rev. B* 1980, 21, 1549.
- [221] Otabe, T.; Ueda, K.; Kudoh, A.; Hosono, H.; Kawazoe, H. *Appl. Phys. Lett.* 1998, 72, 1036.
- [222] Kofstad, P. *Nonstoichiometry, Diffusion, and Electrical Conductivity in Binary Metal Oxides*; Wiley – Interscience, 1972, pp.19.
- [223] Koumoto, K.; Koduka, H.; Seo, W. S. *J. Mater. Chem.* 2001, 11, 251.
- [224] Cava, R. J.; Jr. Peck, W. F.; Krajewski, J. J.; Cheong, S. W.; Hwang, H. Y. *J. Mater. Res.* 1994, 9, 314.
- [225] Cava, R. J.; Zandbergen, H. W.; Ramirez, A. P.; Tagaki, H.; Chien, C. T.; Krajewski, J. J.; Jr. Peck, W. F.; Waszczak, J. V.; Meigs, G.; Roth, R. S.; Schneemeyer, L. F. *J. Solid State Chem.* 1993, 104, 437.
- [226] Jayaraj, M. K.; Draeseke, A.; Tate, J.; Duan, N.; Sleight, A. W. *Proceedings of the MRS Workshop on Transparent Conductive Oxide*, Denever, CO; 19 – 20 June, 2000.
- [227] Lalić, M. V.; Filho, J. M.; Carbonari, A. W.; Saxena, R. N.; Moralles, M. J. *Phys.: Condens. Matter* 2002, 14, 5517.
- [228] Lalić, M. V.; Filho, J. M.; Carbonari, A. W.; Saxena, R. N. *Solid State Communication* 2003, 125, 175.
- [229] Benko, F. A.; Koffyberg, F. P. *J. Phys. Chem. Solids* 1987, 48, 431.
- [230] Cullity, B. D. *Elements of X-ray Diffraction*, Addison-Wesley: CA, 1978.
- [231] Quadri, S. B.; Skelton, E. F.; Hsu, D.; Dinsmore, A. D.; Yang, J.; Gray, H. F.; Ratna, B. R. *Physical Review B* 1999, 60, 9191.
- [232] Nakamoto, *Infrared Spectra of Inorganic and Coordinated Compounds*, John Wiley & Sons, Inc.: New York, NY, 1963.
- [233] Tarte, P. *Spectrochimica Acta* 1967, 23A, 2127.

- [234] Tarte, P. *Mém. Acad. Roy. Belg.* 1965, 35.
- [235] Tarte, P.; Home, J. P. *Acta Cryst.* 1963, 16, 227.
- [236] Tarte, P. *Spectrochimica Acta* 1962, 18, 467.
- [237] Pankove, J. I. *Optical Processes in Semiconductors*, Prentice-Hall. Inc. 1971.
- [238] Moss, T. S. *Optical Properties of Semiconductors*, Butterworths: London, 1959.
- [239] Demichelis, F.; Kaniadakis, G.; Tagliaferro, A.; Tresso, E. *Applied Optics* 1987, 26, 1737.
- [240] Szczyrbowski, J.; Schmalzbauer, K.; Hoffmann, H. *Thin Solid Film* 1986, 137, 169.
- [241] Gurumurugan, K.; Mangalaraj, D.; Narayandass, Sa. K. *Thin Solid Films* 1994, 251, 7.
- [242] Bardeen, J.; Blatt, F. J.; Hall, L. H. *Proc. Atlantic City Photoconductivity Conference*, J. Wiely, Chapman and Hall, 1956.
- [243] Banerjee, A. N.; Ghosh, C. K.; Chattopadhyay, K. K. *Sol. Energy Mat. Solar Cells* 2005, 89, 75.
- [244] Banerjee, A. N.; Maity, R.; Ghosh, P. K.; Chattopadhyay, K. K. *Thin Solid Films* 2005, 474, 261.
- [245] Hicks, L. D.; Dresselhaus, M. S. *Phys. Rev. B* 1993, 47, 12727.
- [246] Hicks, L. D.; Herman, T. C.; Dresselhaus, M. S. *Appl. Phys. Lett.* 1993, 63, 3230.
- [247] Lin-Chung, P. J.; Reinecke, T. L. *Phys. Rev. B* 1995, 51, 13244.
- [248] Broido, D. A.; Reinecke, T. L. *Phys. Rev. B* 1995, 51, 13797.
- [249] Terasaki, I.; Sasago, Y.; Uchinokura, K. *Phys. Rev. B* 1997, 56, 12685.
- [250] Masuda, Y.; Ohta, M.; Seo, W. S.; Pitschke, W.; Koumoto, K. *J. Solid State Chem.* 2000, 150, 221.
- [251] Wang, Y.; Rogado, N. S.; Cava, R. J.; Ong, N. P. *Nature* 2003, 423, 425.
- [252] Willardson, R. K.; Beer, A. C. *Semiconductors and Semimetals*; Vol. 8, Academic Press: New York and London, 1971.
- [253] Park, K.; Ko, K. Y.; Seo, W. –S. *J. Euro. Ceram. Soc.* 2005, 25, 2219.
- [254] Manificier, J. C.; Gasiot, J.; Fillard, J. P. *J. Phys. E* 1976, 9, 1002.
- [255] Maity, R.; Kundoo, S.; Chattopadhyay, K. K. *Solar Energy Materials & Solar Cells* 2005, 86, 217.
- [256] Kröger, F. A. *The Chemistry of Imperfect Crystal*; North Holland, Amsterdam, 1974.
- [257] Hirsch, P.; Howie, A.; Nicholson, R. B.; Pashley, D. W.; Whelan, M. J. *Electron Microscopy in Thin Crystals*; Robert E. Krieger Publishing Co.: Huntington, NY, 1977.
- [258] Lu, Z. H.; Lockwood, D. J.; Baribeau, J. M. *Nature* 1995, 378, 258.
- [259] Reynolds, D. C.; Collins, T. C. *Excitons: Their Properties and Uses*; Academic: New York; 1981.
- [260] Yao, B. D.; Chan, Y. F.; Wang, N. *Appl. Phys. Lett.* 2002, 81, 757.
- [261] Forbes, R. G. *Ultramicroscopy* 1999, 79, 11.
- [262] Forbes, R. G. In *Proceedings of 4th Moscow International ITEP School of Physics*; Suvorov, A. L.; Abov, Y. G.; Firsov, V. G.; Ed.; Academprint: Moscow, 2001; pp 62.
- [263] Robertson, J. *Thin Solid Films* 1997, 296, 61.
- [264] Kotoh, S.; Kikuchi, T.; Muruyama, T.; Kobayashi, T.; Kanaya, M. *Jpn. J. Appl. Phys.* 2002, 41, 3924.
- [265] Satyanarayana, B. S.; Hart, A.; Milne, W. I.; Robertson, J. *Appl. Phys. Lett.* 1997, 71, 1.
- [266] Gupta, S.; Weiss, B. L.; Weiner, B. R.; Pilione, L.; Badzian, A.; Morell, G. *J. Appl. Phys.* 2002, 92, 3311.

-
- [267] Hirakuri, K. K.; Kurata, T.; Mustukura, N.; Friedbacher, G.; Ohuchi, M. *J. Appl. Phys.* 2000, 87, 1.
- [268] Oh, S. J.; Cheng, Y.; Zhang, J.; Shimoda, H.; Zhou, O. *Appl. Phys. Lett.* 2003, 82, 2521.
- [269] Okano, K.; Koizumi, S.; Silva, S. R. P.; Amartunga, G. A. J. *Nature* 1996, 381, 140.
- [270] Gröning, O.; Küttel, O. M.; Gröning, P.; Schlapbach, L. *Appl. Surf. Sci.* 1997, 111, 135.
- [271] Forbes, R. G.; Edgcombe, C. J.; Valdrè, U. *Ultramicroscopy* 2003, 95 57.
- [272] Luo, S.; Chu, P. K.; Zhang, Z. Di, M.; Liu, W.; Lin, C.; Fan, J.; Wu, X. *Appl. Phys. Lett.* 2006, 88, art.# 013109.
- [273] Marathe, S. K.; Koinkar, P. M.; Ashtaputre, S. S.; More, M. A.; Gosavi, S. W.; Joag, D. S.; Kulkarni, S. K. *Nanotechnology* 2006, 17, 1932.
- [274] Lalic, M. V.; Mestnik-Filho, J. *Hyperfine Interactions* 2004, 158, 89.
- [275] Park, K.; Ko, K. Y.; Seo, W. -S. *Mater. Sci. Engg. B* 2006, 129, 1.
- [276] Zheng, X. G.; Taniguchi, K.; Takahashi, A.; Liu, Y.; Xu, C. N. *Appl. Phys. Lett.* 2004, 85, 1728.
- [277] Sauter, D.; Weimar, U.; Noetzel, G.; Mitrovics, J.; Gopel, W. *Sens. Actuators B* 2000, 69, 1.
- [278] Kim, S.-R.; Hong, H.-K.; Kwon, C. H.; Yun, D. H.; Lee, K.; Sung, Y. K. *Sens. Actuators B* 2000, 66, 59.
- [279] Gagaoudakis, E.; Bender, M.; Douloufakis, E.; Katsuarakis, N.; Natsakou, E.; Cimalla, V.; Kiriakidis, G. *Sens. Actuators B* 2001, 80, 155.
- [280] Bender, M.; Gagaoudakis, E.; Douloufakis, E.; Katsuarakis, N.; Natsakou, E.; Cimalla, V.; Kiriakidis, G.; Fortunato, E.; Nunes, P.; Marques, A.; Martins, R. *Thin Solid Films* 2002, 418, 45.
- [281] Koriche, N.; Bouguelia, A.; Aider, A.; Trari, M. *International Journal of Hydrogen Energy* 2005, 30, 693.
- [282] Kizaki, H.; Sato, K.; Yanase, A.; Katayama-Yoshida, H. *Physica B* 2006, 376-377, 812.